The Pennsylvania State University
The Graduate School
College of Engineering

A GRAND POTENTIAL SINTERING MODEL: DERIVATION AND APPLICATION TO UO_2 THERMAL SINTERING, DOPED SINTERING, AND IRRADIATION-ENHANCED DENSIFICATION

A Dissertation in
Nuclear Engineering
by
Ian Greenquist

Submitted in Partial Fulfillment
of the Requirements
for the Degree of

Doctor of Philosophy

August 2019

The dissertation of Ian Greenquist was reviewed and approved* by the following:

Arthur T. Motta
Chair of the Nuclear Engineering Program
Professor of Nuclear Engineering
Dissertation Advisor, Chair of Committee

Michael Tonks
Associate Professor of Materials Science and Nuclear Engineering
University of Florida
Special Member

Nicholas Brown
Associate Professor of Nuclear Engineering
University of Tennessee Knoxville

Clive Randall
Director of Materials Research Institute
Professor of Materials Science and Engineering

Kenan Unlu
Director of Radiation Science and Engineering Center
Professor of Nuclear Engineering

*Signatures are on file in the Graduate School.

Abstract

UO_2 fuel properties such as the temperature profile, fracture, fission gas release, and volumetric changes are partially determined by the fuel microstructure. The initial fuel microstructure is created during the sintering process used to manufacture the UO_2 fuel pellets. A mechanistic microstructural model of sintering can help predict the initial fuel microstructure for various sintering conditions and predict additional densification that occurs during reactor operation.

This work describes the formulation of a grand potential sintering model, the model's verification, and comparisons to existing UO_2 experimental data. The model improves upon existing microstructural models by relying more on the thermodynamic and kinetic driving forces of sintering and less on fitting parameters.

Once the model is developed, it is used to gain additional insight into two additional forms of UO_2 microstructure evolution: doped sintering and irradiation-enhanced densification. Doped sintering is a manufacturing method where chemical dopants are used to increase the density and grain size of sintered UO_2. The grand potential model is used to verify a proposed mechanism for the impact of dopants in UO_2 and compare the density change and grain size to experimental data. Irraidation-enhanced densification is a form of sintering that occurs during the early stages of the fuel lifetime inside the reactor. The model is modified to include irradiation-enhanced densification mechanisms, making it the only microstructural densification model. It is then used in several small simulations to gain additional insight into the bulk behavior of densification.

The findings of this work are as follows: The grand potential sintering model is consistent with sintering theory, but high uncertainties in UO_2 material properties reduce the accuracy compared to experimental data. In addition, the relative sintering behavior of doped UO_2 compared to undoped UO_2 as predicted by the model is very similar to the relative behavior shown in experiments. This result helps validate the proposed dopant mechanism. The model behavior in irradiation-enhanced densification is also consistent with experimental observations. Simulations show that the evacuation of small pores is enhanced by fission events more than large pores or grain boundary pores. The model also predicts that grain size is not a direct controlling factor in the pore evacuation rate. It is more likely that grain size indirectly controls the densification effect by increasing the average pore size.

Table of Contents

List of Figures

List of Tables

List of Abbreviations

ATF	Accident Tolerant Fuel
CASL	Consortium for Advanced Simulation of Light water Reactors
FEM	Finite Element Method
GB	Grain boundary
IC	Initial Condition
IED	Irradiation-enhanced densification
LWR	Light water reactor
MC	Monte Carlo
MCP	Monte Carlo Potts
MOOSE	Multiphysics Object Oriented Simulation Environment
MSC	Master Sintering Curve
NEAMS	Nuclear Energy Advanced Modeling and Simulation
PDE	Partial differential equation
S	Surface

Acknowledgments

I would first like to thank my advisor, Dr. Michael Tonks, a great scientist and a great man. I also want to thank Yongfeng Zhang, Larry Aagesen, Michael Cooper, David Andersson, Daniel Schwen, and Cody Permann, without whom this work would not have been possible. I want to acknowledge my fellow researchers at Penn State and the University of Florida: Lauren Calogero, Amani Chaniour, Floyd Hilty, Jake Hirschorn, Dong-Uk Kim, Kasra Momeni, Ali Muntaha, Aashique Rezwan, Marina Sessim, Pierre-Clement Simon, Xueyang Wu, Shuaifang Zhang, and Yao Zhang.

I also want to thank the wonderful faculty and staff at Penn State, especially Dr. Arthur Motta, who taught me so much and helped me every step of the way.

This work was funded by the Nuclear Energy Advanced Modeling and Simulation (NEAMS) program as well as the Consortium for Advanced Simulation of Light Water Reactors (CASL).

Most importantly, I want to acknowledge my incredible wife, Emily, my wonderful daughters Rubye and Amelia, and the rest of my family and friends whose constant support carried me through this.

Dedication

To Emily. This is your achievement as much as mine.

Chapter 1
Introduction

1.1 Motivation

Current fuel performance codes for light water reactors (LWRs) use experimental data empirically coupled to the fuel burnup to predict fuel properties such as heat conductivity and fission gas release. This results in simple, computationally efficient codes that give high-accuracy results as long as the operating conditions match those used to inform the empirical equations. However, these empirical models cannot be extrapolated to operating conditions that do not match. This means that load following reactors, accident-tolerant fuels (ATFs), and next-generation reactor designs cannot be accurately modeled using empirical models developed using data from constant power operation of traditional LWRs.

To improve the fidelity of fuel performance models outside of experimental data ranges, the Nuclear Energy Advanced Modeling and Simulation (NEAMS) Program, has been working to develop a new set of mechanistic fuel performance codes that rely on the underlying physics to make predictions about fuel behavior. The NEAMS approach is to couple fuel performance properties to microstructural properties such as porosity and grain size distribution. Therefore, the fuel microstructure evolution and history must be well understood and quantified in order to inform fuel performance models.

The microstructure of fresh UO_2 fuel is determined by the sintering process used to manufacture it. Sintering is a process where a powder compact is placed under high temperatures (around 1900 K for UO_2) and the particles fuse together into a dense, porous solid. Within the reactor environment, the fuel pellets continue to densify, accelerated by irradiation. This is known as irradiation-enhanced densification (IED). In order to accurately capture the microstructure evolution of UO_2 fuel, a mechanistic microstructural model of sintering and IED must be developed.

1.2 Overview of Work

This work details the development of a mechanistic microstructural sintering model and its application to UO_2 sintering and IED. Each chapter in this work is a self-contained investigation which builds on the preceding chapters. As such, some information is repeated.

Chapter 2 is a comprehensive, introductory literature review of sintering and IED theory, experimental data, and existing computational models. The work in this chapter has been previously published by the Journal of Nuclear Materials [1].

Chapter 3 details the development and validation of a new, mechanistic microstructural model of sintering. This model is based on the grand potential formulation of the phase field method and improves upon previous microstructural sintering models through an increased reliance on the thermodynamic and kinetic driving forces of sintering and less reliance on fitting parameters. Once the model is developed, it is validated via comparisons to analytical models and it is also compared to experimental data.

Chapter 4 applies the model to doped-UO_2 in order to validate a newly-proposed charged-interstitial mechanism of dopant behavior. Based on this mechanism and these simulation results, a previously unstudied dopant is suggested as a viable near-term deployable ATF.

Chapter 5 modifies the model in order to account for the effects of IED and uses test simulations to gain additional insight into the roles that pore size and grain boundaries play in IED behavior.

Finally, in Chapter 6, conclusions are presented and future work is proposed in order to continue the development of mechanistic fuel performance models.

Chapter 2
Literature Review

2.1 Introduction

UO_2 is ubiquitous in light water nuclear power reactors due to its stability in water and its excellent radiation tolerance. In light water reactors, UO_2 is formed into pellets that are typically about one centimeter in diameter and have a height just above one centimeter. UO_2 is a ceramic, and therefore the pellets are manufactured via sintering. Starting from the initial powder compact and through its initial time in a reactor, UO_2 undergoes gradual densification until the fuel begins to swell. These density changes significantly impact the performance of the fuel rods [2–7]. In this work, this densification of UO_2 is discussed, including thermal densification during sintering and irradiation-enhanced densification during the early stages of fuel life in a reactor.

Sintering refers to the manufacturing process used to create a UO_2 fuel pellet. UO_2 powder is compacted into a highly porous pellet [8]). This powder compact is then heated to high temperatures until the original particles coalesce [6]. The overall volume of the pellet decreases and the density increases, creating a dense, porous pellet.

The term "densification" is often used synonymously with "sintering", but for the purposes of this work, the term "densification" will be used to describe irradiation-enhanced densification (also called irradiation-enhanced sintering). This is a separate phenomenon that occurs once the fuel pellet is placed in a reactor and begins to undergo fission. The volume decreases and density increases, similar to sintering. However, the fission process causes densification to occur faster than sintering under similar conditions outside of a nuclear reactor [9, 10].

For the purposes of reactor design and safety, densification must be modeled in fuel performance codes and this model should be accurate over a wide range of operating conditions including normal operation, startup, shutdown, and accident scenarios. How-

ever, there are several major challenges in the development of the model. Sintering and densification involve complex interactions between the atomistic, meso-, and engineering scales [11]. Densification also occurs simultaneously with swelling, which has the opposite effect to densification. Early in the fuel lifetime, densification is the dominant effect, while after moderate burnup swelling takes over. Even though only one can be observed at a time, both continue to occur throughout the fuel lifetime, partially negating one another. For this reason, and because both are caused by fission within the fuel, densification and swelling cannot be completely isolated experimentally.

This chapter has several purposes:

1. Introduce the physical mechanisms which control sintering and densification; these mechanisms are discussed in Sections 2.3.1 and 2.4.1, respectively.

2. Review experimental data on sintering and densification. Data were collected from multiple sources and compared to determine the mechanisms which play the largest roles. This is done for sintering in Section 2.3.2 and for densification in Section 2.4.2.

3. Examine the models used for predicting sintering and densification. In the case of sintering, three well-developed models are commonly used, which are summarized in Section 2.3.3. The models for densification are less developed and more have been presented in the literature. These are summarized in Section 2.4.3. Section 2.2 discusses how the models are categorized for the purposes of this chapter.

2.2 Types of Models

The models discussed in this chapter will be separated into three categories: empirical, semi-empirical, and mechanistic.

Empirical models are equations with parameters chosen to fit existing data. They are easy to develop, easy to use, and accurate as long as they are within the bounds of experimental conditions. However, empirical models are unreliable outside of these conditions [7, 12, 13]. This limits their usefulness in situations such as accident scenarios, where there may not be sufficient data to fit a model. Empirical models also give no insight into the underlying physics which cause the changes they describe. This further limits their usefulness when trying to improve or optimize fuel performance [14].

Semi-empirical models rely on equations that are based on the underlying physics, but still require some parameters to be fit to data. There are several reasons to use semi-empirical models. They may:

- Give more accurate forms for empirical models. This is done by basing the form of the equation on the underlying physics rather than just finding any equation that can be made to fit the data.
- Improve the computational efficiency of mechanistic models. Complex physics that would be computationally expensive to solve can be glossed over and replaced by terms which were fit to data.
- Act as intermediate steps in the development of mechanistic models
- Stand in for processes which are not fully understood. If there is a phenomenon which is not yet physically understood, this can be accounted for using a fitting parameter.

Mechanistic models are based primarily on a physical description of the phenomena taking place. They use material properties, such as lattice constants or defect formation energies, and some may also include model parameters that need to be determined by fitting to data. Their basis on a physical description makes mechanistic models the hardest to develop because the physics must be well understood and quantified.

This basis in physics makes mechanistic models the most computationally expensive [15]. However, because they rely on an understanding of the physics, validated mechanistic models are more likely to be valid in situations where little or no experimental data have been gathered [12, 16]. Ideally, a mechanistic model would account for all of the necessary physics to be valid in all situations. However, such accuracy would be impossible to guarantee in practice. These considerations mean that mechanistic models are highly valuable in preliminary development of new fuel or cladding concepts, as well as in accident scenario modeling, but they should be backed up with experimental data whenever possible.

Mechanistic models can be further subdivided into continuous models and microstructural models [15]. Continuous models describe changes on the engineering scale with a set of equations. They typically accomplish this by making simplifying assumptions about the microstructure. Some common assumptions are that the microstructure is continuous, or that microstructure features such as grains and voids are spherical [17, 18].

Microstructural models, on the other hand, spatially resolve the microstructure evolution. They do not directly calculate engineering-scale parameters, but these can be determined based on the microstructural results. For example, to calculate the effective thermal conductivity of a microstructure, the local thermal conductivities of the bulk, grain boundaries, and pores are averaged in a physically consistent manner. This makes microstructural models powerful, accurate, and flexible because they reduce the necessary

number of assumptions. However, the smaller scale of microstructural models also makes them the most computationally expensive type of model considered in this chapter. Typically they can only model a small section of a single fuel pellet rather than an entire reactor like an engineering-scale model.

No one model or type of model is appropriate for all scenarios. It is up to researchers to determine which type of model is best suited to the systems they are simulating. To facilitate this decision, this chapter compares models based on type, the physics they account for, the variable they solve for, and, in the case of widely used models, governing equations and major assumptions.

2.3 Sintering

Sintering has been widely studied for many years. As such, it is too wide of a subject for a single chapter to cover in-depth. Therefore, this section is meant to be an introduction to sintering rather than a comprehensive review. Additional review papers on sintering may be found in Refs. [6, 19–22].

2.3.1 Overview of Sintering

Sintering is a common ceramic and metallurgic manufacturing process. In standard thermal sintering, a powder is first pressed into a highly porous pellet; 50–60% of the maximum theoretical density. This powder compact, or "green pellet", is heated, causing the pellet to densify [6,23]. Sintering time varies based on material and desired properties, but typically lasts between several hours and several days [6]. There are many methods of sintering including two-phase sintering [25], microwave sintering [26], spark-plasma sintering [27, 28], and oxidative sintering [34]. Additionally, the sintering atmosphere can be controlled or changed during sintering to give further control [29, 30]. Sintering is used to manufacture UO_2 fuel pellets because the high melting temperature of UO_2 makes other techniques such as casting uneconomical. UO_2 is sintered at a temperature around 1700 °C for several hours [27] until it reaches a density greater than 95% of its theoretical maximum density [17, 27, 31].

The theoretical maximum density is what the density would be if there were no pores or other defects in the fuel. It is calculated based on the lattice arrangement of the atoms [32, 33], giving a value of $10.97 \frac{g}{cm^3}$.

There are many parameters that control the sintering behavior. Some of these parameters within the UO_2 powder that affect the sintered properties are:

- Variation of the oxygen to uranium (O/U) ratio: UO_2 is typically sintered with

an excess of oxygen. Changing the amount of excess oxygen can change the self-diffusion coefficients for vacancies and oxygen atoms. It does this by changing the ionic charge of some of the uranium atoms from U^{4+} to U^{5+} or U^{6+} in order to maintain neutral charge. Since the U^{5+} and U^{6+} atoms have fewer electrons, they are slightly smaller, and there is more room for atoms to diffuse through the lattice [33]. They can also introduce new phases such as U_3O_8 and U_4O_9, which have different properties [34]. For example, U_4O_9 sinters faster than UO_2 [30]. However, the optimum O/U ratio for the thermal conductivity of the fuel is exactly 2.

- The presence of impurities: impurities can enhance or impede grain growth based on their chemical interactions with the lattice [8, 35, 36].

- Variations in particle geometry: changing particle sizes and shapes affects the amount of contact area, the contact angle, and the initial porosity [6, 7]. This can also be impacted by the chemical history of the UO_2 powder. There are two primary chemical paths to get UO_2, which yield different particle size distributions [37].

Properties can also be affected by varying sintering parameters such as temperature [8], pressure [6], time, and the sintering atmosphere [34], which can affect the surface energy, the O/U ratio, and internal pressure in the UO_2.

Most sintering processes are designed to optimize mechanical properties such as yield strength and plastic deformation [6, 38]. However, in the case of UO_2, thermal properties such as heat conduction are more important [4, 31].

Sintering is caused and controlled by self-diffusion of atoms in the crystal lattice [6, 23]. In all crystalline solids, atoms diffuse randomly through the lattice by moving into adjacent vacant lattice sites, called vacancies. If an atom jumping to a vacant lattice site would increase the energy of the lattice, then it is less likely to occur. Conversely, if an atom migrating to a lattice site lowers the energy of the lattice, it is less likely to migrate away from that location and the site is preferred. Atoms on the surface of particles have higher energies than the atoms in the particle interiors. Generally, this energy is lower if the particle is in contact with another particle of the same material than if it is in contact with the atmosphere or a different material. Therefore, lattice sites that increase the contact area between particles are preferred. Such sites are found around the edges of the contact area.

However, when atoms move out of the bulk and to the contact area, they leave behind vacancies within the bulk. The overall energy change of an atom diffusing to the contact area is the difference of the energy reduced by increasing the surface area and

the energy increased by creating a vacancy. This net energy change is also referred to as the sintering stress [15]. The magnitude of the sintering stress depends on the contact angle between the particles, known as the dihedral angle. Sharper contact angles reduce the overall energy. However, as the contact area increases the dihedral angle naturally widens. Figure 2.1 demonstrates the progression of the dihedral angle, ψ, during sintering. Eventually it reaches a wide enough angle that the sintering stress is zero and sintering ceases. This angle is the equilibrium dihedral angle, ψ_e. Because of the limit on the dihedral angle, it is possible for sintering to reach equilibrium with pores still present in the material [19].

The rate at which sintering occurs is controlled by the diffusion rate and sintering stress. The diffusion rate, in turn, is affected by the defect concentration and temperature. More defects mean more atoms can diffuse simultaneously, while higher temperatures allow individual atoms to diffuse faster. This is why sintering is done at high temperature. Additionally, the strain from forming the powder compact can lead to the production of additional vacancies. The sintering stress depends on the contact angle as well as the relative energy differences between the grain interiors, grain boundaries, and free surfaces.

Sintering is often divided into three stages based on the microstructure [38]. Stage one consists of the powder particles increasing their contact areas through the formation of

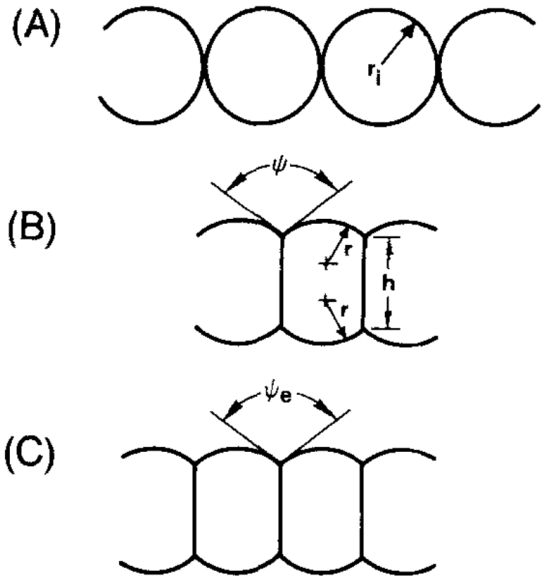

Figure 2.1. Demonstration of sintering theory. A) Powder particles in contact prior to sintering. B) As sintering occurs the particles begin to coalesce. The dihedral angle is the angle of contact between particles and controls the sintering rate. C) Eventually the dihedral angle is wide enough that there is no energy change from neck growth and the particles reach equilibrium [19].

necks [15, 19, 39]. It ends once neck growth ceases to be the major mechanism. Stage two is where the overall density increases as the pores decrease in size [19, 23, 40]. The contact areas grow into planes called grain boundaries [38]. The pores become more columnar in shape as they shrink into tunnel systems on grain boundaries and triple junctions. Stage three begins when pores become closed off to the surface [38]. Grain boundary motion begins as the lattice continues to decrease its overall energy by decreasing the surface area between grains [11, 40, 41]. Large grains grow at the expense of smaller grains [38]. As the grain boundaries move, they can pick up vacancies, impurity atoms, and even small pores. These small pores can come in contact with one another as grains are eliminated. This is called grain boundary sweeping and it is shown in Fig. 2.2 [41]. It reduces the number of pores as well as the defect concentration in regions near moving grain boundaries.

Early sintering models distinguished between the different stages and often only focused on a single stage [23, 24]. However, because the distinctions between stages are not always clear, and because of the development of models that include all three stages, single stage models have become less common. The stages are still commonly used when discussing sintering qualitatively.

During the final stage of sintering, atmospheric pressure becomes important. Since the pores are closed off from the surface, gas is trapped in the pores. As the pores decrease in volume the pressure inside the pore increases, pushing back against further pore shrinkage [38]. In fact, if the temperature is raised suddenly, reverse sintering, in which the pores increase in volume, has been observed for short periods of time [38]. The gas will diffuse into the solid lattice, relieving pressure and allowing sintering to continue. At this point the rate of sintering depends on the gas solubility in UO_2 [38].

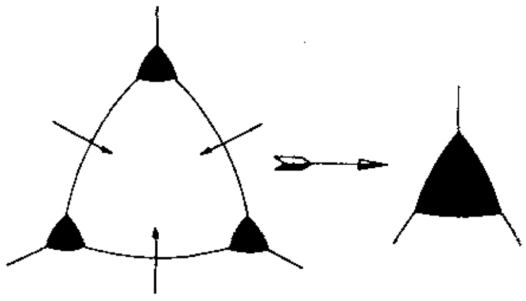

Figure 2.2. Grain boundary motion sweeps pores towards one another and causes them to coalesce [41].

2.3.2 Sintering Experiments and Data

Figure 2.3 shows experimental results from multiple published papers. These papers examined a wide range of parameters and their effects on sintering, including

- Temperature profile [28, 29, 36, 42]
- Sintering time [37]
- Sintering atmosphere and oxidation potential [29, 33, 42, 43]
- O/U ratio [29, 32, 33]
- UO_2 chemical history [37]
- Presence of dopants: Gd_2O_3 [32, 33, 43] can be added as a burnable poison while NbO_2 [42] and Cr_2O_3 [36] can be added to control the microstructure
- Green density [8, 29, 36, 37]
- Particle size distribution [8]
- Alternative sintering techniques including additional atmospheric stages [28, 30, 34].

While sintering time and temperature are clearly important factors, the results show that they are certainly not the only parameters that control sintering. Sintering atmosphere plays a very important role, while particle size distribution does not. The density change caused by additives appears to be rather small. The results of [32, 33, 36] show very little variation in final density. The results of [42] do show a large variation. However, this study looked at the effects of the atmosphere as well as a NbO_2 dopant.

In order to examine the effects of atmosphere more closely, we took the data from [29], which used several different atmospheres while sintering for two hours. This paper started with high O/U ratios ranging from 2.08 to 2.67. Those data are shown in Fig. 2.4 colored by the various atmospheres used. The more inert atmospheres of argon, CO_2, nitrogen, and a vacuum performed very well, despite the potential oxidation effects of CO_2. The oxidizing atmospheres of wet H_2 and partially dried H_2 performed a little better than the reducing atmosphere of dry H_2. At higher temperatures all of the various atmospheres would be expected to converge near maximum density. This demonstrates both that there is an optimum O/U ratio that yields the higher densities, and that the sintering atmosphere is an important factor in sintering behavior.

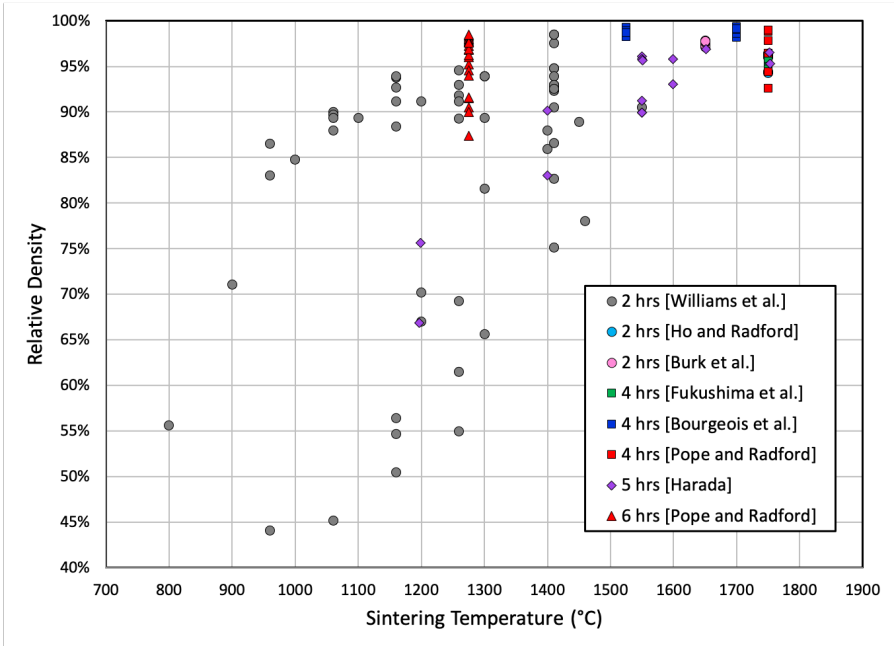

Figure 2.3. Sintering data from [8, 29, 32, 33, 36, 37, 42]. Sintering time and temperature play a large role in final density, but they are clearly not the only important parameters as the results are rather noisy. Sintering atmosphere plays a large effect (see Fig. 2.4). The dopants Gd_2O_3, NbO_2, and Cr_2O_3 do not have large effects on sintering rate. Neither do variations in the particle size distribution.

2.3.3 Sintering Models

The most common approach used to describe sintering is the Master Sintering Curve (MSC), which is a semi-empirical model. Other models exist (including a continuous mechanistic model [44]), but they are not widely used. In addition, two microstructural approaches are typically used to model sintering. The Monte Carlo Potts (MCP) model simulates the random diffusion within a material. The phase field sintering model is based on diffusion theory. It is the most recently developed of the models and has shown promising results.

Note that the final solution of a microstructural sintering model could act as the initial condition of similar microstructural densification models. Coupling of this kind can, in theory, improve the accuracy of microstructural models by using an initial condition based on sintering physics rather than a condition based on averaged values.

2.3.3.1 Master Sintering Curve

The MSC model began in 1992 when Hansen et al. developed a single model to describe all three stages of sintering [45]. It was refined by Su and Johnson in 1996 [46]. Later,

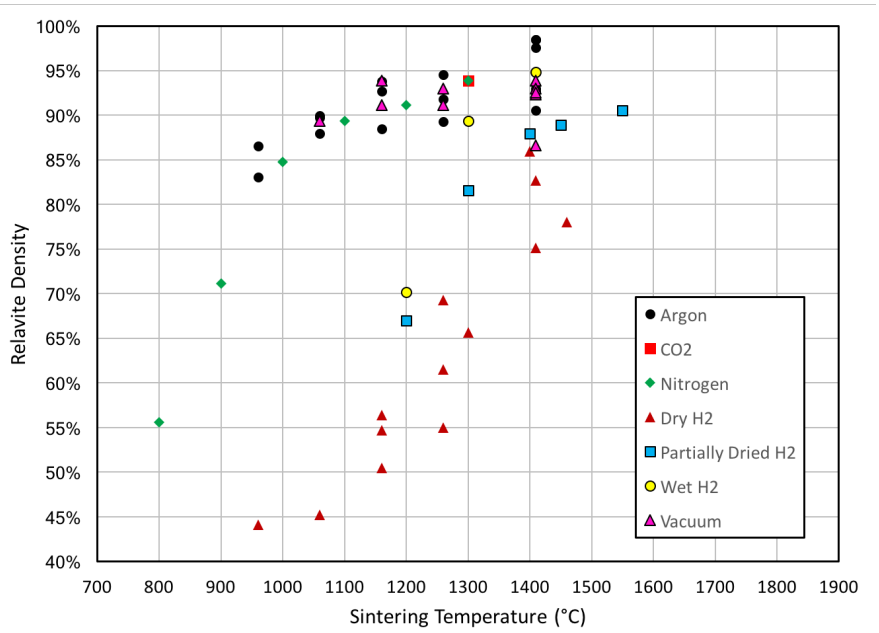

Figure 2.4. Sintering results from [29] colored by sintering atmosphere. Each sample was sintered for two hours. The trends become much more clear as inert and oxidizing atmospheres perform better than reducing atmospheres [29].

easier methods to fit empirical data were added in 2006 [47] and 2008 [48]. Now it is widely used for a large variety of sintering methods and materials [25, 28, 49–71]. Figure 2.5 shows one example of a MSC compared to experimental results for ThO_2 mixed with some UO_2 [65].

The MSC model is a semi-empirical model. It is based on sintering theory, but relies on several fitting parameters to simplify the equation and get the correct shape. These parameters allow it to reduce to a single equation rather than a system of coupled equations. The fitting parameters allow it to account for low-effect variables such as minor impurities and small variations in the atmosphere's oxygen potential. It also allows simplification by considering only bulk diffusion and ignoring diffusion along free surfaces and grain boundaries. However, it also means that new fitting parameters must be developed for each set of sintering conditions.

The dependent variable is the relative density of the material. In other words, the MSC equation solves for the density compared with what the density would be if there were no pores. The governing equation is derived from the PDE

$$\frac{1}{3\rho}\frac{d\rho}{dt} = \frac{\gamma\Omega}{kT}\left(\frac{\Gamma_v D_v}{G^3} + \frac{\Gamma_b \delta D_b}{G^4}\right), \tag{2.1}$$

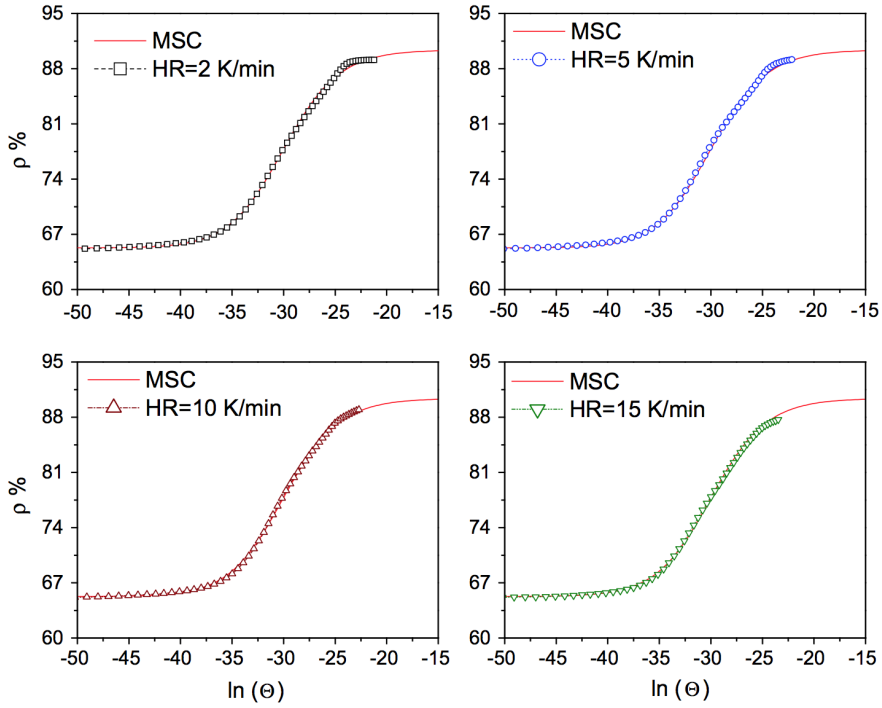

Figure 2.5. Master sintering curves for ThO_2 with 4% UO_2 compared to experimental results for four different heating rates [65].

where ρ is the relative density, γ is the surface energy, Ω is the atomic volume, k is the Boltzmann constant, G is the mean grain diameter, δ is the grain boundary width, and T is temperature. D_v and D_b are the diffusion coefficients for volume and grain boundaries, respectively, while Γ_v and Γ_b are associated fitting parameters.

The solution to Eq. (2.1) is

$$\frac{k}{\gamma\Omega D_0}\int_{\rho_0}^{\rho}\frac{[G(\rho)]^n}{3\rho\Gamma(\rho)}d\rho = \int_0^t \frac{1}{T}\exp(-\frac{Q}{RT})dt, \tag{2.2}$$

where D_0 is the initial grain boundary diffusion coefficient, ρ_0 is the initial relative density, $n = 3$, R is the universal gas constant, Q the activation energy of diffusion, and Γ is a fitting parameter.

In most conditions the MSC is a very useful and powerful model. It is able to take a given starting powder and predict how different densities, pore size distributions, and grain sizes can be achieved by modifying the sintering parameters. The major assumptions of the MSC are

1. The vacancy concentration is in equilibrium [45]

2. The microstructure is continuous and only depends on density [46]

3. Sintering is dominated by a single mechanism [46].

These assumptions are not always valid. Assumption 1 means that the MSC is not valid as a densification model since one of the characteristics of densification is a higher vacancy concentration. Assumption 3 means that the MSC may not be accurate if the sintering time is extremely long. Assumption 2 has the largest effect. In reality, the microstructure depends on other parameters besides density, such as the sintering atmosphere and the chemical history of the UO_2. Therefore, the model only predicts sintering behavior if the initial condition closely matches the initial condition of the experimental data it was fit to [46].

2.3.3.2 Monte Carlo Potts

The Monte Carlo Potts (MCP) method has been in use since it was first developed in 1990 [15, 21, 72–110]. It is a mesh-based microstructural model which relies on Monte Carlo simulations. These simulations are designed to approximate the random diffusion of atoms in the crystal lattice. Each point on the mesh has a value that represents either a void or a particular grain orientation. Typically voids are represented with 0 or -1 while positive integers represent the grain orientations. The grain boundaries and free surfaces are represented as sharp interfaces between two mesh points with different values. The energy associated with each mesh site is based on the number of neighbors to that site with the same value according to the equation [100]

$$E = \frac{1}{2}\sum_{j=1}^{n} J_{ij}(1 - \delta(q_i, q_j)), \tag{2.3}$$

where n is the number of neighbors for site i, J_{ij} is the neighbor interaction energy between sites i and j, q_i is the value of site i, and $\delta(q_i, q_j)$ is the Kronecker delta function

$$\delta(q_i, q_j) = \begin{cases} 1, & q_i = q_j \\ 0, & q_i \neq q_j \end{cases}. \tag{2.4}$$

At each time step, a random site is chosen to either switch values randomly or swap with a neighboring site, depending on how the simulation is set up [15, 86, 100]. The change in the free energy from this change, ΔE, is calculated. The probability of the change being

accepted is given by [100]

$$P = \begin{cases} \exp\left(-\frac{\Delta E}{kT}\right), & \Delta E > 0 \\ 1, & \Delta E \leq 0 \end{cases}, \tag{2.5}$$

where kT approximates the Boltzmann constant multiplied with the temperature, but is actually a chosen constant to get the desired behavior [74, 78, 100].

An example simulation covering 900 time steps is shown in Figs. 2.6 and 2.7 [110]. Fig. 2.6 shows the microstructure. It begins with obviously defined particles closely packed together and shows the contact area between them increasing until they have formed a single multi-grain solid with pores. Fig. 2.7 shows the relative density of the same simulation. The density increases rapidly at first, but as it approaches equilibrium, the sintering rate decreases.

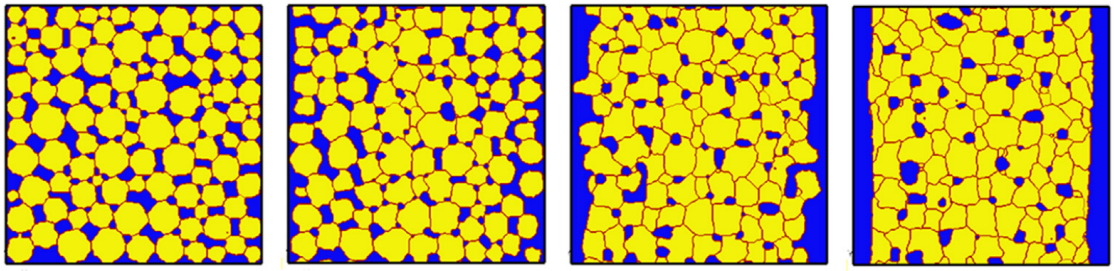

Figure 2.6. Example of a Monte Carlo Potts simulation progression. From left to right: Simulation at 1, 50, 300, and 900 Monte Carlo steps. The system evolves from multiple particles to a porous polycrystalline solid [110].

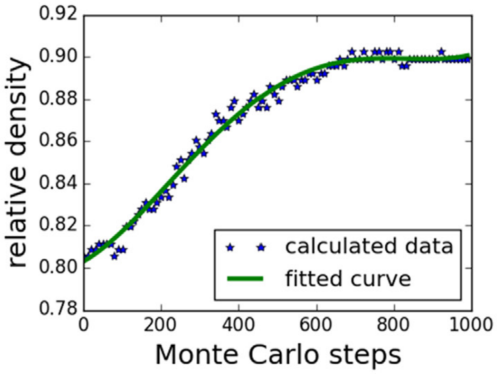

Figure 2.7. Density Measurement associated with Fig. 2.6. The density begins by increasing steadily, but as the driving force decreases the system approaches equilibrium [110].

The major assumption in MCP is that the mesh sites behave like atomic lattice sites. In truth the mesh sites are much larger than the lattice sites. So, like all microstructure

methods, a finer mesh will yield more accurate results.

Like all Monte Carlo methods, MCP has no built-in time scale. The times are given in Monte Carlo steps. However, several techniques exist to approximate the real time [111].

2.3.3.3 Phase Field Sintering

Phase field is a common method for simulating microstructure evolution. Like the MCP model, it is a mesh-based microstructural model that uses variable values to describe different microstructural regions. However, while the MCP model relies on sharp interfaces between grains, the phase field method uses diffuse interfaces, which allows the variables to be continuous. For a more complete discussion on the basics of the phase field method, see references [112, 113].

Generally, the phase field method relies on two governing equations. The Cahn-Hilliard equation is derived from the diffusion equation and describes variables subject to conservation laws such as mass or energy [115]:

$$\frac{\partial \rho}{\partial t} = \nabla \cdot M \nabla \frac{\delta F}{\delta \rho}, \tag{2.6}$$

where ρ is the conserved variable, F is a function giving the energy of the system, and M is the mobility parameter for ρ. The Allen-Cahn equation describes variables that are not subject to conservation laws [116]:

$$\frac{\partial \eta}{\partial t} = -L \frac{\delta F}{\delta \eta}, \tag{2.7}$$

where η represents an non-conserved variable such as grain orientation or phase, and L is the mobility of η.

The total energy F is defined as

$$F = \int \left[f(\rho, \eta) + \kappa_\rho (\nabla \rho)^2 + \kappa_\eta (\nabla \eta)^2 \right] dV, \tag{2.8}$$

where f is the free energy function of the material and the κ terms are gradient energy coefficients chosen to control the interface widths. It is possible to add any number of conserved and non-conserved variables by adding gradient energy terms and including them in the free energy function.

Researchers began attempting to apply phase field to sintering in 1999 [117, 118]. However, these initial simulations were not able to capture sintering without an additional driving force to account for rigid body motion of the particles due to the sintering stress [117]. It was only in 2006 that Wang fully incorporated rigid body motion into a

phase field model [119]. The model increased in popularity in 2014 and has been getting wide use since [39, 120–128, 176].

Wang's model works by modifying Eqs (2.6) and (2.7) to include rigid body velocity, $\vec{v}_{adv}$ [119]:

$$\frac{\partial \rho}{\partial t} = \nabla \cdot \left(D \nabla \frac{\delta F}{\delta \rho} - \rho \vec{v}_{adv} \right), \tag{2.9}$$

$$\frac{\partial \eta}{\partial t} = -L \frac{\delta F}{\delta \eta} - \nabla \cdot (\eta \vec{v}_{adv}). \tag{2.10}$$

It is generally accepted that inclusion of the rigid body velocity improves the accuracy of the simulation [39, 117]. However, some studies have produced similar behavior without including the rigid body velocities [129].

In this model, the conserved variable represents the relative density of the material being sintered with respect to a fully dense material at any point on the mesh. Non-conserved variables may be used to represent grain orientations and/or the individual powder particles. The free energy function is set up to make sure the non-conserved variables prefer to overlap with the conserved variables.

Figure 2.8 gives an example of a phase field sintering simulation with eight particles being sintered together for 156 seconds. The behavior is similar to Fig. 2.6 in that it begins with individual particles and ends with a single mass [39].

The major assumptions in the phase field method are that the processes are driven by diffusion and the boundaries are diffuse. Thinner boundaries tend to improve accuracy over wide boundaries, but require a finer mesh and can have convergence problems. The researcher must balance the computational time with the accuracy of the simulation. In

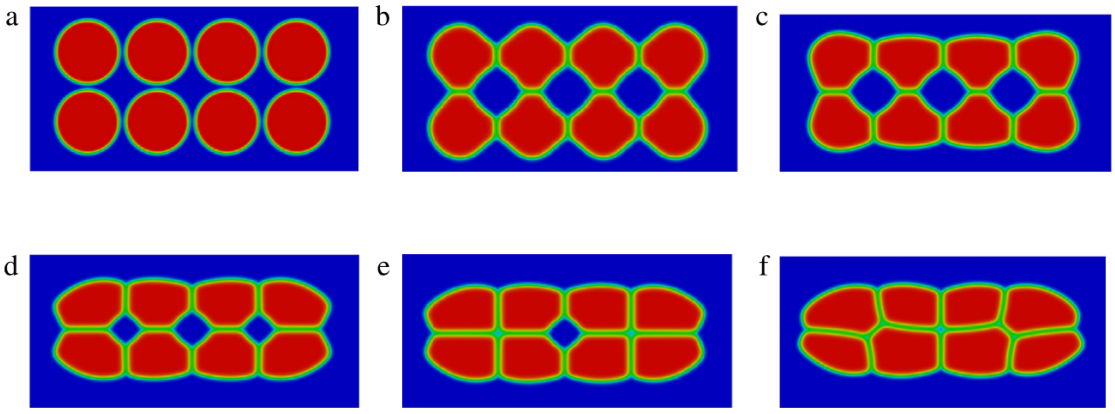

Figure 2.8. Example of phase field sintering simulation using eight particles. The times shown are a) 0 s, b) 2 s, c) 20 s, d) 100 s, e) 125 s, f) 156 s [39].

addition, the phase field method uses a continuum approximation of a material, where the individual atoms are described by the density and their configuration is described by order parameters. This approximation is accurate when the interface width is significantly larger than the lattice constant. Therefore, it is important to maintain an interface width that is much larger than the lattice constant.

2.4 Densification

2.4.1 Overview of Densification

Densification is an in-reactor phenomenon where fresh fuel increases in density as pores left over from sintering are evacuated. It impacts fuel performance in several ways. In the fuel, densification improves thermal conductivity and speeds up grain growth. In the gap, the decreasing volume increases the gap width and lowers the gap conductivity. The overall effect is generally to increase the centerline temperature of the fuel. Therefore, it is an important phenomenon to understand and model.

Densification has been studied since the early 1970's [10, 17]. It was initially believed to be a continuation of final-stage sintering [10, 130]. However, it occurs faster than sintering would under the same conditions without fission [9, 10].

This increase in sintering speed is caused by fission fragment collisions occurring within the fuel during reactor operation [17, 131, 132]. The fission chain reaction that powers nuclear power plants produces large amounts of energy. Most of the energy is carried as kinetic energy in the fission fragments. These fragments collide with atoms in the fuel lattice, which transfers energy to the lattice atoms and knocks them out of their lattice sites. The fission product continues to collide with more atoms even as those atoms knock other atoms out of lattice sites in a chain reaction. This is called a collision cascade and it results in a large section of lattice where atoms are displaced and diffusing at a highly accelerated rate [133].

Collision cascades speed up the sintering rate in three ways:

1. Accelerated localized diffusion: within the cascades the atoms diffuse incredibly quickly as the energy liquefies the region for a few picoseconds [134]. Since sintering is caused by diffusion, this fast diffusion speeds up sintering.

2. Increased defect production: as a collision cascade ends, the atoms that were displaced return to the lattice, but not all of them manage to reach an empty lattice site. These atoms are left as interstitials. They also leave a vacancy somewhere nearby in the lattice [135]. This pair of defects is called a Frenkel pair. Since point

defects are necessary for diffusion, Frenkel pairs speed up diffusion within the grain in general [11, 133]. The exact change in the diffusion rate has been a subject of study for many years [9, 136, 137].

3. Pore damage: if a collision cascade occurs close enough to a pore, it will scatter some of the pore volume into the lattice as vacancies [11]. Large pores will be damaged and decrease in volume, but most of the vacancies will find their way back to the pore, causing minimal densification. Small pores will be completely destroyed, forcing the vacancies to migrate farther. This directly decreases the volume of the pores in the UO_2 [17]. Therefore, small pores contribute more to densification than large pores.

2.4.2 Densification Experiments and Data

The most common research goal in densification experiments is to determine the thermal and irradiation stability of fuel pellets. Researchers have used different manufacturing methods and additives to try to minimize the amount of densification in the fuel to less than 1% [10].

Factors that control densification include:

- Temperature [130]
- Burnup [130, 138]
- Fission gas release and swelling [139]
- Pore size distribution [10, 130]
- Grain size distribution [140]

Pore and grain size distributions, as well as pellet density, are in turn dependent on the sintering conditions used to manufacture the pellet. Therefore, it is also important to understand the pellet's manufacturing history.

The most challenging part of densification experimentation is isolating the effect. Swelling is a process caused by fuel fissioning and radiation damage in which solid and gaseous fission products cause the fuel to swell and pores to expand. The gaseous fission products combine with vacancy clusters formed by collision cascades to form fission gas bubbles. Because both effects are caused by fission, swelling is impossible to isolate from densification. The best researchers are able to do is to run experiments at low temperatures and burnups where swelling is less prominent [10, 130]. However, even doing this it is not possible to fully remove the effects of swelling from the experimental

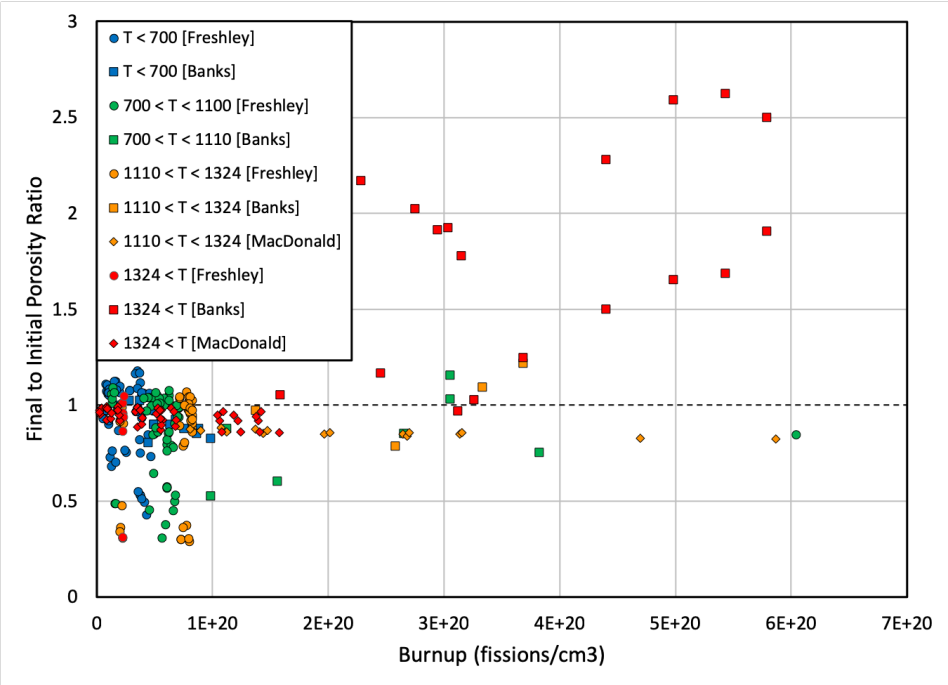

Figure 2.9. Experimental data collected from [10, 130, 138]. It compares the fuel burnup to the ratio of final to initial porosity. Ratios greater than 1 show swelling while ratios below 1 show densification. Data are colored based on the temperature range of the samples. While it is clear that high temperature and high burnup lead to swelling, swelling can still be observed even at very low temperatures and burnups. In order to compare results from the various papers, density data from all three were converted to the units shown while burnup data from [138] was converted from $\frac{MWd}{kg}$ to the units shown.

results [139]. This can be observed in Fig. 2.9. We collected densification measurements from several papers and again arranged them to determine the parameters that exhibit the most control over densification. The x-axis is fuel burnup and the y-axis is the ratio of the final porosity to the initial porosity, such that values below 1 show densification while values greater than 1 show swelling. The data were marked based on temperature. The average center temperatures of the different samples were divided into quartiles and distinguished by marker shape and color. The results show that high burnup and temperature do indeed lead to higher rates of swelling. However, even at low temperature and burnup it can be difficult to isolate the effects.

Though sintering and densification are related behaviors, differences in the objectives of research in the two areas is clearly evident by comparing Figs. 2.3 and 2.4 with Fig. 2.9. Researchers in sintering identify the conditions (temperature, sintering time, etc.) required to fabricate a sample with a specified geometry. Researchers in densification are concerned with the continuous reduction in volume of the fuel with time (typically

measured in terms of burnup), until swelling dominates and the volume begins to increase.

Several parameters are very important to consider in densification, especially

- Burnup [138]
- Fuel temperature [130]
- Fission rate
- Initial fuel density [130]
- Pore size distribution: fuels with small pores undergo densification significantly faster than fuels with large pores. This is both because collision cascades destroy small pores and because small pores sinter faster.
- Grain size distribution: large-grained fuels may exhibit more densification. This is believed to have less to do with densification and more to do with slowing down swelling by not allowing fission products to gather at grain boundaries [140].

2.4.3 Densification Models

Despite similarities to sintering, densification models are less developed than sintering models. This is likely because of densification is a smaller field of study, it has been studied for a shorter period of time, and it adds additional complex physics which must be considered. Though the models are less developed, more models are reviewed here than in Section 2.3.3 because none are used by the majority of researchers in the area. It is worth noting that all of the models summarized here are empirical or semi-empirical; our review found no mechanistic models for densification.

The most commonly employed models are empirical models. A typical empirical model, the ESCORE model, is summarized below. The first successful semi-empirical densification model was the Assmann and Stehle model. It was the first to identify collision cascades as the source for increased diffusion [17, 131, 132]. Although it is no longer used, all of later semi-empirical models are based on the Assmann and Stehle model [11, 141, 142], and for this reason it is summarized below.

2.4.3.1 ESCORE

A common empirical model in is the ESCORE model [12, 13]. It has a wide range of experimental data to back it up and is among the simplest models currently used. It uses only a single equation,

$$\epsilon_D = \Delta\rho_0 \left(\exp\left(\frac{Bu \ln(0.1)}{C_D Bu_D} \right) \right). \tag{2.11}$$

ϵ_D is the densification strain. $\Delta\rho_0$ is the total densification that can occur. Bu and Bu_D are the burnup and the burnup at which densification is complete, respectively. C_D is given by the equation

$$C_D = \begin{cases} 7.2 - 0.0086(T-25), & 25 \leq T \leq 750 \\ 1, & T > 750 \end{cases} \tag{2.12}$$

where T is temperature in units of $°C$.

2.4.3.2 Assmann and Stehle

The Assmann and Stehle model was developed between 1974 and 1978 [17, 131, 132]. It is a semi-empirical model which relies on experimental results to fill gaps in difficult-to-calculate parameters. It considers sintering, vacancy generation from cascades near pores, pore damage, and vacancy diffusion. However, it does not include Frenkel pair production.

Some of the major assumptions in the model are

- Pores are spherical
- Pores come in groups of discrete sizes
- Each group of pores can be clearly labeled as fine or coarse based on their volume
- Only one effect contributes to densification at a time
- The temperature determines which effect contributes.

The sizing of pores can present difficulties with this model. First of all, the shape of the size distribution may be unknown [143]. Also, there may not be a clear cutoff to separate fine and coarse pores.

The model breaks densification into four temperature regions shown in Table 2.1 [17]. Each region has its own governing equation for the behavior of coarse pores. Fine pores behave the same in each region, so have only one governing equation.

The governing equations are

$$\left(\frac{\Delta V}{V_0}\right)^c_{I,II} = -\sum_i P^c_{0,i}\left[1 - \left(1 - \frac{(D^{th}_v + D^{irr}_v)C_S t}{r^2_{0,i}}\right)^{3/2}\right] \tag{2.13}$$

$$\left(\frac{\Delta V}{V_0}\right)^c_{III} = -\sum_i P^c_{0,i}\left[1 - \left(1 - \frac{\lambda\omega G C_S t}{3r_{0,i}}\right)^{3}\right] \tag{2.14}$$

$$\left(\frac{\Delta V}{V_0}\right)_{IV}^{c} = -\sum_i P_{0,i}^{c}\left[\frac{6\Omega\gamma D(x)t}{kTr_{0,i}^3}\right]. \tag{2.15}$$

$$\left(\frac{\Delta V}{V_0}\right)^{f} = -f^* P_0^f (1-\exp(-\eta^*\Omega_S G t)) \tag{2.16}$$

where $\left(\frac{\Delta V}{V_0}\right)$ is the relative density change, c and f represent the effects from coarse and fine pores, respectively, and the roman numerals correspond to the regions in Table 2.1. The rest of the parameters are summarized in Table 2.2.

This model is based on a stage 3 sintering model, but specifically considers pores that are smaller than grains and according to their radii. The sintering MSC model, by contrast, looks at pores that are both larger and smaller than the grains and measures the overall density. These differences cause the governing equations to look different. However, in stage IV, the Assmann and Stehle model is controlled by sintering so Eq. (2.15) is the most similar to Eq. (2.2). In addition, sintering models are focused on predicting the final state of the sintered material as a function of the sintering conditions, while densification models predict the increase in density with time.

2.4.3.3 Other Densification Models

Table 2.3 summarizes five additional densification models that have been developed. The models are presented by model name, year, and type. Additionally, Table 2.3 compares the models based on the dependent variable and what physics are included in each model. None of the semi-empirical models are widely used. Most fuel performance codes use empirical models [143, 144]. The MFPR code does rely on semi-empirical models, but their corresponding densification model seems to have been developed for the individual code [11].

2.4.3.4 Guidance for Future Model Development

Development of a microstructural densification model would be easiest by making adjustments to the microstructural sintering models discussed in Section 2.3.3. However,

Region	Temperature Range	Vacancy Generation	Vacancy Migration
I	$\leq 450°C$	Athermal	Athermal
II	$450 \rightarrow 750°C$	Athermal	Thermal*
III	$750 \rightarrow 1300°C$	Athermal*	Thermal
IV	$\geq 1300°C$	Thermal	Thermal

Table 2.1. Temperature regions for Assmann and Stehle model. Thermal refers to sintering. Athermal refers to irradiation-enhanced densification. * = Rate controlling mechanism [17].

these models would have to be adjusted to consider the impact of radiation damage on the microstructure behavior, including accelerated localized diffusion, increased defect production, and pore damage. The MCP model could possibly be adjusted to include events that mimic collision cascades by alternating the values of a region of mesh points rather than just a single point. The phase field sintering model could be adjusted by adding stochastic terms to consider the collision cascade; e.g. that add the impact of defect generation, local temperature increases, and dispersement of defects around pores. The rigid body velocity would also be removed. These alterations would require time and space averaging to make the collision cascades fit on the mesh point and last for a time step during a simulation.

Once a microstructural model is developed and validated, it could be used in the development of an engineering-scale model by allowing researchers to separate densification from swelling within the model, or allow examination of the fuel microstructure while under irradiation. Such data, combined with experimental data, could give researchers valuable insights into which parameters are the most important for predicting densification.

Variable	**Physical Description**
C_S	Saturation concentration of vacancies in UO_2
$D(x)$	Self-Diffusion coefficient of uranium in UO_{2+x}
D_v^{irr}	Vacancy diffusion coefficient from irradiation
D_v^{th}	Vacancy diffusion coefficient from heat
G	Fission rate (fissions $cm^{-3}s^{-1}$)
f^*	Fraction of vacancies captured by coarse pores
i	Denotes a set of coarse pores with the same radius
k	Boltzmann constant
$P_{0,i}^c$	Initial pore volume fraction for a set of coarse pores
P_0^f	Initial fine pore volume fraction
$r_{0,i}$	Initial radius for a set of coarse pores
T	Temperature
t	Time
η^*	Vacancies per encounter that escape from fine pores
λ	Viable track length of fission fragments
ω	Atomic volume of UO_2
Ω	Vacancy volume
Ω_S	Collision cascade volume

Table 2.2. Descriptions of parameters used in the Assmann and Stehle model.

2.5 Conclusions

Reactor fuel pellets are fabricated using sintering, in which powder compacts densify to form fuel pellets. During reactor operation, fuel pellets continue to densify, but at a faster rate than would be expected in thermal sintering under the same conditions. This is caused by the effects of radiation. Eventually, enough fission products build up and cause the fuel to swell. This leads to a net increase in fuel volume. Sintering determines the porosity and microstructure at the beginning of fuel life, while densification must be accounted for in order to accurately model dimensional changes in UO_2.

Of the two effects, sintering is better understood. It is controlled primarily by the sintering temperature, the sintering time, the O/U ratio of the fuel, and the sintering atmosphere. Sintering modeling has converged to three models in wide use. The MSC is the most common model and is a semi-empirical equation that is simple to use. However, changes to the initial conditions such as the fuel's chemical history or its O/U ratio require the development of new curves. The MCP model and the phase field sintering models are both microstructurally resolved mechanistic models. These do not rely on fits to data, which makes them potentially more flexible and better equipped to handle different sintering conditions. However, the models are complex and computationally expensive, limiting the amount of material that can be modeled. Additionally, these models have not yet been fully validated against experimental data. Their accuracy is still in doubt.

Densification is a combination of sintering and irradiation damage from collision cascades. It is less understood both because the physics are more complex and experimental data are harder to obtain. However, it is known that the primary factors are the burnup, temperature, density, and pore size distribution. Densification primarily relies on empirical models. These models are very simple and accurate, but limited by the range of experimental data, which can be difficult to obtain. Several semi-empirical models exist.

Model Name	**Year**	**Type**	**Dependent Variable**	**Included Physics**					**Refs**
				TS	DG	DD	PD	EP	
Macewen & Hastings	1975	S	Pore Radius	X	X	X			[135]
Dollins & Nichols	1978	S	Pore Volume	X	X	X	X		[141]
Bouguerra & Si-Ahmed	1991	S	Pore Radius	X	X	X	X		[142]
MATPRO	1993	E	Strain						[144, 145]
MFPR	2014	S	Pore Volume	X	X	X		X	[11]

Table 2.3. Comparison of several densification models based on the type, dependent variables, and the physics included in each one. Key: TS = Thermal Sintering, DG = Defect Generation, DD = Defect Diffusion, PD = Pore Damage, EP = Equilibrium pores. E = Empirical, S = Semi-Empirical.

These models are more complex, but also give more insight into the underlying physics. However, there is not currently any mechanistic models of densification. We recommend that a mechanistic densification model should be developed in order to improve the physical understanding of the process as well as to add another tool to be used in fuel and cladding design. One straightforward way to accomplish this would be to find a way to include radiation damage to the already existing MCP or phase field sintering models.

Chapter 3
Grand Potential Sintering Model Development and Verification

3.1 Introduction

Bulk material properties, such as thermal conductivity, strength, and resistance to fracture are largely determined by the material microstructure. In sintered materials, the microstructure is determined by the sintering conditions [6]. Sintering is a common manufacturing process in metals and ceramics in which a highly-porous powder compact (the green body) is heated so that the particles coalesce into a dense, polycrystalline solid. Sintering occurs due to vacancy diffusion, which causes the total surface area to decrease by forming grain boundaries (GBs) [19]. The material densifies as vacancies diffuse along GBs from interior pores to to external surfaces [146, 177]. In addition, the GBs migrate to reduce the total GB area in a process known as coarsening; this GB migration is slowed by interactions with pores [1, 125](Chapter 2). The sintering process is shown schematically in Fig. 3.1.

Determining the proper sintering conditions to produce desired properties requires the ability to quantitatively predict microstructure evolution during the sintering process. There are four governing mechanisms which must be accounted for in any quantitative microstructural sintering model:

- Sintering stress—The driving force for densification during sintering is the energy difference between surfaces and GBs. As a GB is formed at the neck of two particles, it reduces the free surface area while increasing the GB area, thus reducing the overall surface energy and increasing the overall GB energy [1](Chapter 2). Only

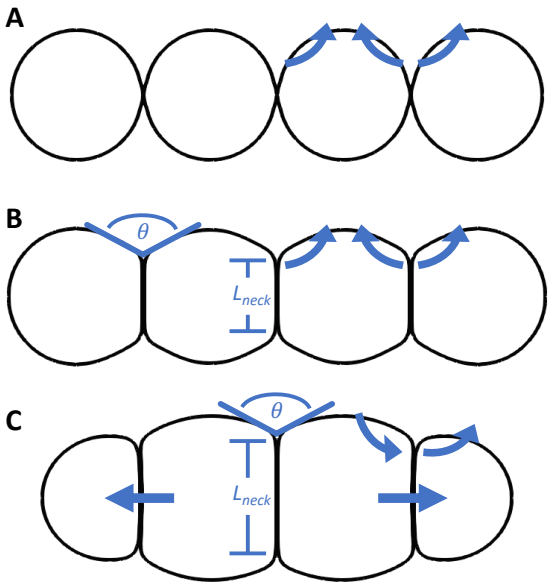

Figure 3.1. Simple demonstration of sintering theory. A: Four particles inside a powder compact. Vacancies diffuse from contact regions between particles to free surfaces, increasing the particle contact area and changing particle shape. Arrows show the direction of vacancy motion. B: Particle contact regions grow into necks of width L_{neck} to form GBs. There is a material-specific dihedral angle, θ, observed where GBs meet surfaces. C: Necks fully form into GBs. The neck width and dihedral angle are also shown. GB motion consumes small grains at the expense of large ones. Additional arrows show the direction of GB motion. The dihedral angle remains constant throughout grain growth.

when the surface energy is larger than the GB energy is there a thermodynamic driving force for sintering. The energy difference between surfaces and GBs is known as the sintering stress. The surface and GB energies interact when GBs intersect surfaces, resulting in a contact (or dihedral) angle θ, shown in Fig. 3.1, that is controlled by the ratio of the GB to surface energy.

- GB/vacancy interaction—GBs play a major role in the elimination of vacancies that results in densification. The effect of GBs can be considered in two ways, both of which result in densification. The first is that vacancies are annihilated by GBs and the second is that GBs serve as rapid diffusion paths for vacancies to reach free surfaces.

- Non-uniform diffusion—The kinetics of densification during sintering are governed by the rate at which vacancies diffuse through the material. However, diffusion does not occur at a uniform rate throughout the material. It is accelerated on GBs and surfaces because there is more empty space for atomic vibrations. Thus, GB and surface diffusion are rate-controlling factors for sintering kinetics [119].

- Grain coarsening—The driving force for coarsening is the reduction in the total grain boundary energy as large grains grow and small grains shrink. The kinetics are dictated by the GB mobility and by the interactions with pores.

There are several models available to describe sintering. Macroscale descriptions, such as the master sintering curve, predict the overall density and porosity change of the green body, but do not predict the evolution of the microstructure [1](Chapter 2). There are also analytical models based entirely on sintering theory [119] that exist for specific idealized cases involving only a few particles. They cannot predict the density change of the green body, but they are useful for describing sintering mechanics and verifying more advanced models. Microstructural sintering models resolve the individual particles of a green body and predict both the densification and microstructure evolution [1](Chapter 2). Due to the large computational cost of resolving individual particles, microstructural models are not typically used to model an entire green body.

Two microstructural sintering models are in common use [1](Chapter 2). The first is the Monte Carlo (MC) Potts method; originally developed in 1990 [72, 73, 87]. This is a stochastic MC method that represents three processes: GB migration, migration of pores by surface diffusion and vacancies by GB diffusion, and vacancy annihilation at GBs. The domain is represented by a computational grid, with the state at the grid points representing either voids or grains. Grid point states are randomly varied, and the probability that the new state is accepted depends on the resultant change in the free energy of the system. The MC Potts model provides a powerful means of modeling large numbers of particles in both 2D and 3D, and model predictions have been directly compared against experimental data [100]. However, while the MC Potts model quantitatively predicts the thermodynamics of a given material, it cannot quantitatively predict the kinetics because, like all MC models, it does not have a built-in timescale.

The other microstructural sintering model uses the phase field method [119]. The phase field method represents the microstructure using continuous variable fields [112, 113] that evolve according to partial differential equations to minimize the free energy. Interfaces between microstructural features are represented by regions where variables smoothly transition between equilibrium values. Early attempts to apply the phase field method to sintering found that it under-predicted sintering rates [117]. Wang corrected this in 2006 with the Rigid Body Motion model [119], which speeds up densification by introducing a rigid body force that represents vacancy annihilation by GBs. The model is qualitative and not material specific, and the rigid body force adds computational complexity. Others have applied this model to study densification kinetics [39], though no comparisons have been made to experimental data.

In this work, a new phase field model for sintering is presented that is fully quantitative and material specific. It provides complete control over the surface and grain boundary energies to properly describe the sintering stress. It separately describes diffusion through the bulk, along GBs, and along surfaces, and it accurately captures grain coarsening. It builds on many recent developments in phase field modeling [125, 147–149], including the grand potential model [150, 151], to accurately describe densification rates without rigid body motion physics. The new grand potential sintering model is derived is Sec. 3.2. Then the model is verified against analytical expressions and the thermodynamic and kinetic behavior is investigated in Sec. 3.3. In Sec. 3.4, initial comparisons against sintering data for UO_2 green bodies are carried out.

3.2 Model Description

The grand potential sintering model quantitatively describes microstructure evolution during sintering, including densification and coarsening. In the model, the surface and GB energies for a specific material are defined, which quantifies the sintering stress. The model assumes vacancies segregate to GBs and then rapidly diffuse along them to surfaces. The diffusion coefficients for bulk, GB and surface diffusion are defined, and GB and surface diffusion occur only within their planes. Finally, the GB mobility is defined, and its value, along with void interactions, control the coarsening kinetics.

This section provides the mathematical basis for the model. In Sec. 3.2.1, the governing equations for the phase field method are described. In Sec. 3.2.2, the phase field model is converted to a grand potential formulation. In Sec. 3.2.3, the assignment of parameter values to make a quantitative sintering model is described. Finally, in Sec. 3.2.4, values are assigned to properties in order to model the well-studied material UO_2.

3.2.1 Phase Field Method Formulation

There are two regions in the model. The solid region is represented by the subscript s and the void region is represented by the subscript v. There are n order parameter variables associated with the solid region, $\vec{\eta} = \{\eta_1, \eta_2, ..., \eta_n\}$. These distinguish the various grains. There is one order parameter variable associated with the void region, ϕ, which represents all pores and the external void region. The order parameters are not subject to any conservation law, and are therefore controlled by the Allen-Cahn equation [116]:

$$\frac{\partial \eta_i}{\partial t} = -L_s \frac{\delta F}{\delta \eta_i},$$

$$\frac{\partial \phi}{\partial t} = -L_v \frac{\delta F}{\delta \phi}, \tag{3.1}$$

where L is the order parameter mobility and F is the total free energy of the system. As is commonly done to simplify polycrystal simulations, it is assumed that all GB properties are isotropic [113], such that L is constant. The order parameter values are constant within a region, but smoothly transition between values across interfaces. The various regions of the domain are defined by these variables as follows:

- A grain is a region where $\eta_i = 1$, $\eta_j = 0$ for all $j \neq i$, and $\phi = 0$.
- A void is a region where $\phi = 1$ and $\vec{\eta} = 0$.
- A GB is a region where $0 < \eta_i < 1$, $0 < \eta_j < 1$ for some $j \neq i$, and $\phi = 0$.
- A surface is a region where $0 < \eta_i < 1$, $\eta_j = 0$ for all $j \neq i$, and $0 < \phi < 1$.

To represent the fraction of lattice sites occupied by vacancies, which are subject to conservation of mass, the conservation variable field c is used. This is governed by the Cahn-Hilliard equation [114]:

$$\frac{\partial c}{\partial t} = \nabla \cdot \mathbf{M} \nabla \frac{\delta F}{\delta c}, \tag{3.2}$$

where $\mathbf{M}$ is the phase field mobility tensor for c. The total free energy, F is defined according to:

$$F = \int_V \left[f_b(\vec{\eta}, \phi) + f_{gr}(\nabla \vec{\eta}, \nabla \phi) + h_s f_s(c) + h_v f_v(c) \right] dV, \tag{3.3}$$

where f_b is the bulk energy, f_{gr} is the gradient energy, f_s and f_v are the energies of the solid and void regions, respectively, and h_s and h_v are switching functions that interpolate smoothly between values corresponding to the two regions. The switching functions have the constraint $h_s + h_v = 1$.

The bulk energy ensures that the order parameters have the correct values in the different regions and is calculated according to the equation [147]

$$f_b(\vec{\eta}, \phi) = \epsilon \left[\left(\frac{\phi^4}{4} - \frac{\phi^2}{2} \right) + \sum_{i=1}^{n} \left(\frac{\eta_i^4}{4} - \frac{\eta_i^2}{2} \right) + \gamma \left(\phi^2 \sum_{i=1}^{n} \eta_i^2 + \sum_{i=1}^{n} \sum_{j>i}^{n} \eta_i^2 \eta_j^2 \right) + \frac{1}{4} \right], \tag{3.4}$$

where ϵ is the free energy barrier coefficient and γ is the interface profile coefficient. The gradient energy is calculated as [112, 113]

$$f_{gr}(\nabla \vec{\eta}, \nabla \phi) = \frac{1}{2} \kappa \left[(\nabla \phi)^2 + \sum_{i=1}^{n} (\nabla \eta_i)^2 \right], \tag{3.5}$$

where κ is the gradient energy coefficient. The region energies are assumed to be parabolic [151]:

$$f_s(c) = \frac{1}{2}k_s \left(c - c_s^{eq}\right)^2,$$
$$f_v(c) = \frac{1}{2}k_v \left(c - c_v^{eq}\right)^2, \tag{3.6}$$

where c_s^{eq} and c_v^{eq} are the equilibrium vacancy concentrations in the two regions and k_s and k_v are parabolic energy coefficients. ϵ and κ define additional energy added to the system within the region interfaces.

One issue with this formulation occurs within interfaces transitioning from solid regions to void regions. In such regions, c is transitioning between c_s^{eq} and c_v^{eq}, and is out of equilibrium with both phases, resulting in large values for f_s and f_v that make it difficult to quantitatively assign a value for the surface energy. Here, this issue is remedied by converting to the grand potential formulation. However, other models, like the Kim-Kim-Suzuki model [152], could also be used to remedy the issue.

3.2.2 Conversion to Grand Potential Model

Grand potential conversions were developed by Plapp for parabolic energy functions as well as the dilute species and ideal solution cases [150]. The grand potential formulation used in this work is based on the model developed by Aagesen et al. [151], which in turn relies on the thermodynamic analysis of Moelans [147]. A different grand potential formulation was also proposed by Choundhury et al. [153], but is not used in this work.

In the grand potential model, the evolution equations are derived from a functional of the grand potential density:

$$\Omega = \int_V \left[f_b(\vec{\eta}, \phi) + f_{gr}(\nabla\vec{\eta}, \nabla\phi) + h_s\omega_s(\mu) + h_v\omega_v(\mu)\right] dV, \tag{3.7}$$

where Ω is the total grand potential and ω_s and ω_v are the grand potential densities for the solid and void phases, respectively. Eq. (3.7) is used in Eq. (3.1) in place of Eq. (3.3):

$$\frac{\partial\eta_i}{\partial t} = -L_s\frac{\delta\Omega}{\delta\eta_i},$$
$$\frac{\partial\phi}{\partial t} = -L_v\frac{\delta\Omega}{\delta\phi}. \tag{3.8}$$

To convert from the phase field model to a grand potential model, the variable c is removed as an independent variable and replaced with the chemical potential μ. The first step of this process is to define vacancy concentration variables for each phase: c_s

and c_v. The chemical potential is derived from the Hemholtz free energies (Eq. (3.6)) as:

$$\begin{aligned}\mu &= V_a \frac{\partial f_s(c_s)}{\partial c_s} = V_a \frac{\partial f_v(c_v)}{\partial c_v}, \\ &= V_a k_s \left(c_s - c_s^{eq}\right) = V_a k_v \left(c_v - c_v^{eq}\right), \end{aligned} \tag{3.9}$$

where V_a is the atomic volume of the species. Eq. (3.9) is then inverted to give:

$$c_s = \frac{\mu}{V_a k_s} + c_s^{eq},$$

$$c_v = \frac{\mu}{V_a k_v} + c_v^{eq}, \tag{3.10}$$

$$c = h_s \left(\frac{\mu}{V_a k_s} + c_s^{eq}\right) + h_v \left(\frac{\mu}{V_a k_v} + c_v^{eq}\right). \tag{3.11}$$

Eq. (3.6) is replaced with the potential density equations according to:

$$\begin{aligned}\omega_s(\mu) &= f_s(c_s(\mu)) - c_s(\mu)\frac{\mu}{V_a} = -\frac{1}{2}\frac{\mu^2}{V_a^2 k_s} - c_s^{eq}\frac{\mu}{V_a}, \\ \omega_v(\mu) &= f_v(c_v(\mu)) - c_v(\mu)\frac{\mu}{V_a} = -\frac{1}{2}\frac{\mu^2}{V_a^2 k_v} - c_v^{eq}\frac{\mu}{V_a}. \end{aligned} \tag{3.12}$$

Since c is no longer an independent variable, Eq. (3.2) is replaced by an evolution equation for the chemical potential:

$$\frac{\partial \mu}{\partial t} = \frac{1}{\chi}\left[\nabla \cdot (\chi \mathbf{D} \nabla \mu) - \frac{1}{V_a}\left(\frac{\partial c}{\partial \phi}\frac{\partial \phi}{\partial t} + \sum_{i=1}^{n} \frac{\partial c}{\partial \eta_i}\frac{\partial \eta_i}{\partial t}\right)\right], \tag{3.13}$$

where $\mathbf{D}$ is the diffusivity tensor, χ is the susceptibility

$$\chi = \frac{1}{V_a}\frac{\partial c}{\partial \mu} = \frac{1}{V_a^2}\left(\frac{h_s}{k_s} + \frac{h_v}{k_v}\right), \tag{3.14}$$

and $\mathbf{M} = \chi \mathbf{D}$.

It is worth noting that Eq. (3.13) can be derived by applying Eq. (3.11) to the continuity equation

$$\frac{\partial c}{\partial t} = -\nabla \cdot \mathbf{j}, \tag{3.15}$$

where $\mathbf{j}$ is the vacancy flux. This ensures that vacancies will still be conserved.

3.2.3 Quantitative Parameter Assignment

To make the grand potential model quantitative and material specific, it is necessary to go into more detail about the assignment of individual parameter values. These

values and their partial derivatives were implemented in the implicit finite element code MARMOT [154]. Not only do partial derivatives show up in the governing equations such as Eqs. (3.8) and (3.13), but additional derivatives are required to derive the Jacobian matrix. However, for the sake of brevity, calculations of derivatives are left to the reader.

First, the energy coefficients from Eqs. (3.4) and (3.5) can be defined as

$$\begin{aligned} \epsilon &= h_S \epsilon_S + h_{GB} \epsilon_{GB}, \\ \kappa &= h_S \kappa_S + h_{GB} \kappa_{GB}, \\ \gamma &= 1.5, \end{aligned} \tag{3.16}$$

where h_S and h_{GB} are functions that switch between surface and grain-boundary interfaces, and ϵ_S, ϵ_{GB}, κ_S, and κ_{GB} are corresponding constant values on those interfaces. The value for γ is 1.5 to yield symmetric interfaces [147]. The values for ϵ_S, ϵ_{GB}, κ_S, and κ_{GB} can be defined in terms of the width of the diffuse interface l, the isotropic GB energy σ_{GB} and the isotropic surface energy σ_S following the approach from Moelans [147]:

$$\begin{aligned} \epsilon_S &= 6\frac{\sigma_S}{\ell}, & \kappa_S &= \frac{3}{4}\sigma_S \ell, \\ \epsilon_{GB} &= 6\frac{\sigma_{GB}}{\ell}, & \kappa_{GB} &= \frac{3}{4}\sigma_{GB} \ell. \end{aligned} \tag{3.17}$$

There are now four switching functions (h_s, h_v, h_S, h_{GB}), all of which need to be included along with their partial derivatives in order to solve Eqs. (3.8) and (3.13). For simplicity, all are based on the same second-order continuous piecewise polynomial:

$$H(\phi, \phi_0) = \begin{cases} 0, & \phi \leq 0 \\ 6\left(\frac{\phi}{\phi_0}\right)^5 - 15\left(\frac{\phi}{\phi_0}\right)^4 + 10\left(\frac{\phi}{\phi_o}\right)^3, & 0 < \phi < \phi_0 \\ 1, & \phi \geq \phi_0 \end{cases}, \tag{3.18}$$

where $0 < \phi_0 \leq 1$. The piecewise components of Eq. (3.18) ensure that the switching functions are limited to the domain $[0, 1]$ even in the case of numerical noise causing ϕ to leave these limits. The individual switching functions are then defined as

$$\begin{aligned} h_v &= H(\phi, 1), & h_s &= 1 - h_v, \\ h_S &= H(\phi, \phi_0 < 1), & h_{GB} &= 1 - h_S. \end{aligned} \tag{3.19}$$

These definitions give several advantages. First, since they rely on only a single variable, fewer partial derivatives are needed. Second, the functions and their derivatives are

continuous and defined throughout the entire domain. This is very important for implicit solvers because it helps keep the Jacobian matrix stable; any undefined values or sudden jumps can cause convergence problems. However, there is also a drawback in that h_S goes to zero before the end of the interface, depending on the value of ϕ_0. Thus, some error will be introduced to the surface energy. This error is quantified in Sec. 3.2.4. An alternate form for the switching function was proposed by Moelans [155] that is constant across surface interfaces but has undefined regions that may caused convergence problems in implicit codes.

The diffusivity tensor is defined as [148]:

$$\mathbf{D} = \mathbf{D}_B + \mathbf{D}_{GB} + \mathbf{D}_S, \tag{3.20}$$

$$\mathbf{D}_B = D_B \mathbf{I}, \tag{3.21}$$

$$\mathbf{D}_{GB} = D_{GB} \sum_{i=1}^{n} \sum_{j \neq i} \eta_i \eta_j \mathbf{T}_{GB}^{ij}, \tag{3.22}$$

$$\mathbf{D}_S = D_S \phi^2 (1-\phi)^2 \mathbf{T}_S, \tag{3.23}$$

$$\mathbf{T}_{GB}^{ij} = \mathbf{I} - \frac{\nabla\eta_i - \nabla\eta_j}{|\nabla\eta_i - \nabla\eta_j|} \otimes \frac{\nabla\eta_i - \nabla\eta_j}{|\nabla\eta_i - \nabla\eta_j|}, \tag{3.24}$$

$$\mathbf{T}_S = \mathbf{I} - \frac{\nabla\phi}{|\nabla\phi|} \otimes \frac{\nabla\phi}{|\nabla\phi|}. \tag{3.25}$$

$\mathbf{D}_B$, $\mathbf{D}_{GB}$, and $\mathbf{D}_S$ are the diffusivity tensors for the bulk, GB, and surface regions, respectively. D_B, D_{GB}, and D_S are the diffusivity magnitudes. $\mathbf{I}$ is the identity tensor, and $\mathbf{T}_{GB}^{ij}$ and $\mathbf{T}_S$ are the GB and surface directional tensors. The form of $\mathbf{D}_B$ assumes isotropic bulk diffusion, and the forms of $\mathbf{D}_{GB}$ and $\mathbf{D}_S$ only allow diffusion along GBs and surfaces, respectively. If known, D_B, D_{GB}, and D_S can be used directly. If not, then D_{GB} and D_S can be approximated by adding weights to the bulk diffusivity according to:

$$\begin{aligned} D_{GB} &= w_{GB} D_B, \\ D_S &= w_S D_B, \end{aligned} \tag{3.26}$$

where D_B is calculated using the standard Arrhenius equation:

$$D_B = D_0 \exp\left(-\frac{E_m^B}{k_B T}\right). \tag{3.27}$$

D_0 is the diffusivity prefactor, E_m^B is the migration energy of vacancies in the bulk, k_B is Boltzmann's constant, and T is the absolute temperature.

The order parameter mobilities depend on the phase mobilities and interface width

according to:

$$L_s = \frac{4}{3}\frac{M_s}{\ell},$$
$$L_v = \frac{4}{3}\frac{M_v}{\ell}. \tag{3.28}$$

The solid phase, or GB, mobility is defined as:

$$M_s = M_0 \exp\left(-\frac{Q}{k_B T}\right), \tag{3.29}$$

where M_0 is the mobility prefactor and Q is the mobility activation energy. The void phase mobility is required for the model, but does not represent a physical quantity. Voids are as mobile as the solids around them. Therefore, the requirement for the void mobility is that it is large enough not to impede diffusion in the solid. It can be estimated by multiplying the solid mobility by an additional factor:

$$M_v = mM_s. \tag{3.30}$$

The equilibrium concentrations from Eq. (3.12) also need to be determined. Vacancies are missing atoms in the crystal lattice; therefore, having vacancies in unstructured regions such as voids or GBs does not make sense physically. However, for the sake of conserving mass, these regions must have vacancy concentrations within the model. In this model, vacancies may be thought of as a specific volume of empty space. By this logic, the equilibrium vacancy concentration within void regions is $c_v^{eq} = 1$. For the solid phase, more behavior must be accounted for. Vacancies segregate to GBs and move to the external surfaces via GB diffusion. In order to account for this, the solid phase vacancy concentration is defined as

$$c_s^{eq} = c_B^{eq} + 4c_{GB}^{eq}\left(1-\lambda\right)^2, \text{ where}$$
$$\lambda = \sum_{i=1}^{n} \eta_i^2$$
$$c_B^{eq} = \exp\left(-\frac{E_f}{k_B T}\right). \tag{3.31}$$

Here, $\lambda < 1$ identifies GBs, c_B^{eq} is the bulk vacancy concentration, c_{GB}^{eq} represents additional vacancy concentration on GBs, and E_f is the vacancy formation energy in the bulk.

This grand potential sintering model includes all of the governing mechanisms listed in Sec. 3.1. It includes the sintering stress by separately defining the surface and GB energies. Vacancy segregation to GBs is included using the solid phase vacancy concentration

c_s^{eq}. Non-uniform diffusion is accounted for through the diffusivity tensor $\mathbf{D}$, which distinguishes between bulk, surface, and GB diffusion both in terms of direction and magnitude. Thus, the vacancies can diffuse along GBs and surfaces faster than through the bulk. Grain coarsening is a well-established feature of the phase field method [112,113] and has also been observed in the grand potential formulation this work is based on [151].

3.2.4 Material Properties

In order to compare this model to experimental data, the material properties must be chosen to match a real material. For this work, the material uranium dioxide (UO_2) is used. The vacancy concentration describes U vacancies, since U-lattice vacancies are much less mobile than the O-lattice vacancies and limit the overall diffusion rate [156]. Many of the UO_2 vacancy property values can be taken directly from the literature. These values are listed in Table 3.1. Some discussion, however, is necessary on the values for σ_{GB} and σ_S.

According to Hall et al. [157], the GB and surface energies are difficult to measure experimentally and depend heavily on the experimental setup. Therefore, the experimental values from the literature have significant scatter. However, the ratio of surface to GB energy remains relatively constant at $\sigma_S/\sigma_{GB} = 2$ no matter the experimental setup. For this reason, it was decided to use a GB energy σ_{GB} value obtained via atomistic simulation [158] for a $\Sigma 5$ tilt boundary and define the surface energy $\sigma_S = 2\sigma_{GB}$. Since the GB energy value was only calculated at a single temperature, any temperature dependence in the GB energy is neglected.

The diffusivities are calculated according to Eqs. (3.26) and (3.27). However, the bulk, GB, and surface diffusivities are also subject to an extremely large experimental error. Various values from experiments and atomistic simulations from the literature are shown in Fig. 3.2. At the lowest temperature shown, the bulk diffusivities vary by a factor of 10^{15}. Matzke et al. [156] found in 1987 that experiments prior to 1975 had a systemic error causing their results to be several orders of magnitude too large.

Parameter	**Value**	**Units**	**Ref.**
V_a	0.04092	nm^3	[159]
σ_{GB}	9.86	eV/nm^2	[158]
σ_S	$2\sigma_{GB}$	eV/nm^2	[157]
M_0	1.476×10^9	$nm^4/eV\ s$	[160]
Q	2.77	eV	[160]
E_f	2.69	eV	[161]

Table 3.1. UO_2 constant material parameters taken from the literature.

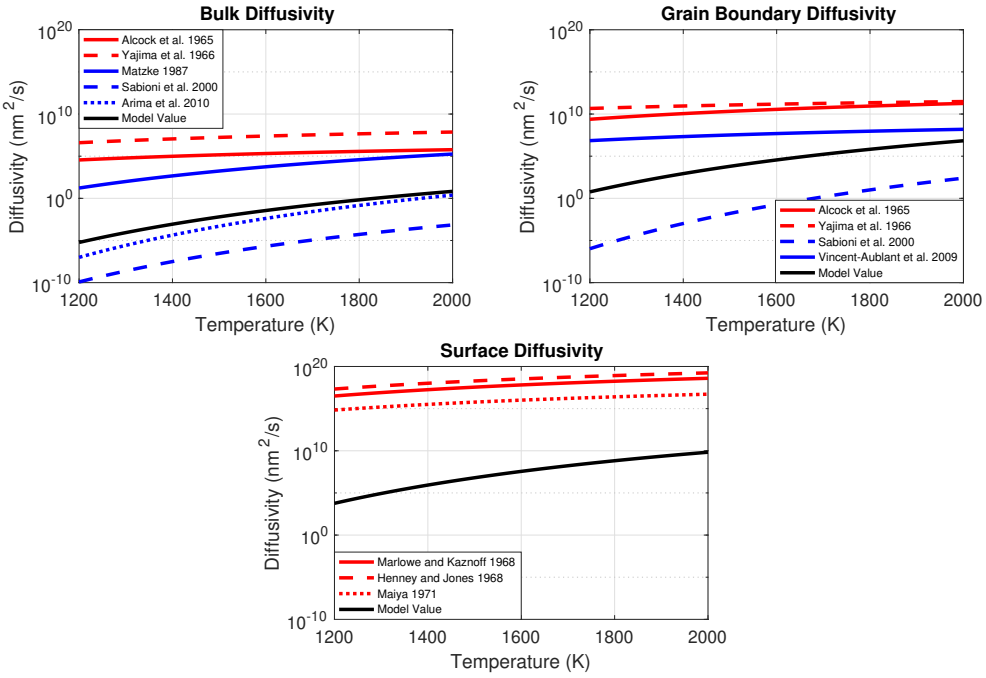

Figure 3.2. Various experimental values for bulk [156, 162, 163, 165, 166], GB [162, 164–166], and surface [167–169] diffusivities. Before 1975 there was a systemic error in the methods used to measure diffusivities, causing results to be several orders of magnitude too high [156]. Measurements from before 1975 are shown in red and more recent measurements are shown in blue. The values used in the simulation are shown in black. They fall somewhere near the center of the blue measurements and about 10 orders of magnitude below the red measurements.

But even discounting those values, the bulk diffusivities still vary by up to a factor of 10^{10}. Therefore, the value used in the sintering model was calculated based on the three diffusivities taken since 1987 [156, 162, 163] by using the average bulk migration energy (E_m^B) and the log-average diffusivity prefactor (D_0). The values used are $E_m^B = 3.608$ eV and $D_0 = 8.33 \times 10^9$ nm^2/s. The GB weight was chosen to be $w_{GB} = 10^6$ in order to keep it approximately average between two GB diffusivities calculated since 1975 [162, 164]. A literature review did not find post-1975 values for the surface diffusion. Additionally, convergence problems began to manifest in the model when the surface diffusion weight was too large. Therefore, the surface diffusion weight was chosen to be a large enough value to be approximately consistent with the other weights and not too large to cause convergence problems: $w_S = 10^9$.

The phase mobility multiplication factor was chosen to be $m = 40$ because it was the lowest value at which the void phase mobility did not significantly affect the simulation results.

To determine a value for the additional vacancy equilibrium concentration on GBs

c_{GB}^{eq}, the free volume at GBs was assumed to be caused by U-vacancies. Brutzel and Vincent-Aublant found that GBs take up 15% more volume than the same number of atoms in the bulk [170] and Freyss et al. found that vacancies are 31% smaller than U atoms [171]. From these findings, the GB equilibrium concentration is determined to be

$$c_{GB}^{eq} = x(1 - c_U^{GB}) = \frac{V_U}{V_v}\left(1 - \frac{V_B}{V_{GB}}\right) = 0.189, \tag{3.32}$$

where x is the number density ratio of U vacancies to U atoms and c_U^{GB} is the concentration of U atoms on GBs.

The value for parabolic free energy coefficient k_s was determined by fitting a parabolic curve to the ideal solution model [150] from $c = 0$ to $c = 1$ at various sintering temperatures. The parabolas were then fit to a linear temperature equation:

$$k_s \left\langle \frac{eV}{nm^3} \right\rangle = 157.16 - 0.0025T \left\langle K \right\rangle . \tag{3.33}$$

Since voids do not have a measurable energy, k_v is not an easily obtained value. So it is assumed that $k_v = 10k_s$ in order to ensure that the void phase equilibrium concentration is always near its equilibrium value, which is set to $c_v^{eq} = 1$.

The value of the interface width ℓ and the temperature T vary between simulations. ℓ is a modeling parameter that is set depending on the size of the domain being modeled. It is selected to be as small as possible but still allow simulations to complete in a reasonable time (three to five elements should cover the distance ℓ). The value of T depends on the conditions being modeled.

To determine the switching value for the S/GB interface ϕ_0, an investigation was carried out to determine the relationship between the error and the value of ϕ_0. To do this, a set of 1D simulations was used with a single surface interface using $\ell = 50$ nm, $T = 1700$ K, a domain size of 200 nm, and 400 elements across the domain. The initial condition put the interface in the center of the domain with a cosine-profile interface. The simulations ran until MARMOT detected steady-state conditions. The surface energy was determined by numerically integrating Eq. (3.3). The phase energies were converted from functions of c to functions of μ using Eq. (3.11). First, a simulation using constant values was used to verify that the integrated surface energy matched σ_S for the condition $\epsilon = \epsilon_S$ and $\kappa = \kappa_S$. Then simulations were performed using Eq. (3.16) and values of ϕ_0 ranging from 0.1 to 0.6. The relative errors were calculated based on the difference between the value of σ_S used in Eq. (3.17) and the value calculated by the integral. The relative memory was calculated based on the increased memory used by MARMOT compared to the case which used the least memory. The relative error and the memory

used in the simulations were then plotted for these values in Fig. 3.3. The results show that, as expected, smaller values of ϕ_0 produce less error at the expense of increasing the memory usage. The value of $\phi_0 = 0.3$ keeps the error below 5% and the memory increase below 10%. Considering the high uncertainty already in the surface energy value [172], this level of error was deemed acceptable.

All of the material properties for UO_2 have now been defined. These values will be used in the rest of the work, except where otherwise specified.

3.3 Model Verification

Now that the model is established, it must be verified that it behaves as expected and is implemented correctly. This is done in two ways. First, in Sec. 3.3.1 the model is compared with two analytical models to verify that it behaves consistently with the established sintering theory. Then in Sec. 3.3.2, the model behavior is tested against the

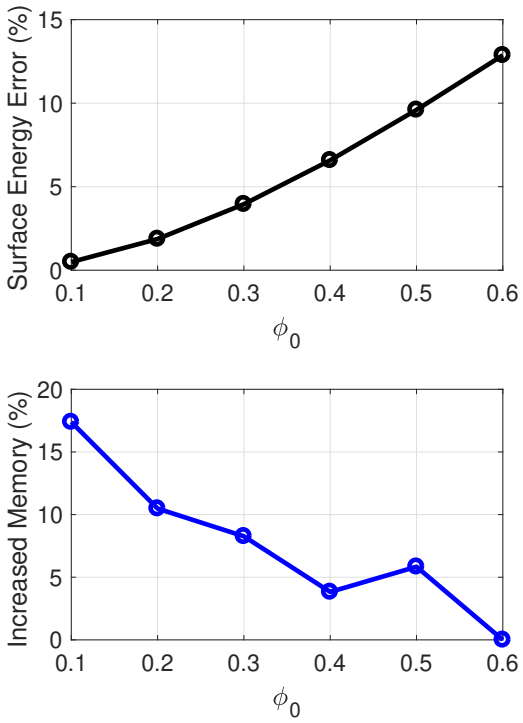

Figure 3.3. Selection of the value for ϕ_0 using a 1D surface interface calculation. TOP: Quantification of surface energy error introduced by Eqs. (3.16), (3.18) and (3.19). Small values of ϕ_0 reduce the error. BOTTOM: Quantification of memory usage compared to the simulation which used the least amount of total memory. Small values of ϕ_0 increase memory usage. $\phi_0 = 0.3$ was chosen to keep the error below 5% and the memory increase below 10%.

governing mechanisms listed in Sec. 3.1. The results of these comparisons are discussed in Sec. 3.3.3.

3.3.1 Comparison to Analytical Description

In certain idealized test cases, sintering theory allows for problems to be solved analytically and without the use of numerical methods. Two of these problems involve the behavior of two spherical or circular particles as they sinter together. The first of these is the time-evolution of the neck region. The neck width can be expressed in both 2D and 3D cases as [119]:

$$\left(\frac{L_{neck}}{D}\right)^n = Kt, \tag{3.34}$$

where L_{neck} is the neck width (first used in Fig. 3.1), D is the original particle diameter, t is the sintering time, K is a fitting parameter depending on the material and problem scale, and n is a parameter which depends on the rate-controlling diffusion process. For GB-controlled diffusion, $n = 6$. For surface-controlled diffusion, several values have been proposed for n including 3, 6, and 7 [119].

The second model describes the equilibrium contact angle (dihedral angle) of the sintered material. This is a vital expression both in experiments and simulations [172]. The relationship between dihedral angle and the ratio of GB to surface energy is [119,173]:

$$\frac{\sigma_{GB}}{\sigma_S} = 2\cos\left(\frac{\theta}{2}\right), \tag{3.35}$$

where θ is the dihedral angle. When Hall et al. reviewed surface energy data [157], they found that not only did the dihedral angle measurements vary significantly, but that the effect of temperature changed depending on the experimental setup. However, two of the major trendlines crossed at 1816 K where the dihedral angle was measured as $\theta = 163°$. This temperature and angle represent the most reliable experimental data on dihedral angles for UO_2.

3.3.1.1 Simulation Descriptions

For both analytical model comparisons, the same basic simulation setup was used. Two 2D particles with a diameter of 300 nm were placed side by side in a 680 nm×580 nm mesh. Mesh adaptivity was used, with the coarsest mesh having an element size of (20 nm)^2 and the finest with an element size of (5 nm)^2. The interface width was set to $\ell = 20$ nm and the temperature was set to $T = 1816$ K. The initial condition interface used a hyperbolic tangent profile of thickness ℓ, which is a reasonable approximation to

the actual interface profile [155].

Three simulations were performed to test the neck-growth behavior. The first was a GB-controlled diffusion case with the surface diffusion weight from Eq. (3.26) set to $w_S = 1$ and the second was a surface-controlled case with the GB diffusion weight set to $w_{GB} = 1$. The third case included both effects. The neck width was measured by looking at ϕ along the line $x = 340$ nm and measuring the distance between the two locations where $\phi = 0.5$. If the points fell between two mesh elements, then the exact position was estimated using linear interpolation. The neck width evolution was fit to a power law $L_{neck} = at^b$ and solved for K and n according to $n = \frac{1}{b}$ and $K = (\frac{a}{D})^n$.

Three cases were likewise compared to test the effects of interface energies on the dihedral angle. The value of σ_S was changed according to $\sigma_S = \sigma_{GB}$, $\sigma_S = 2\sigma_{GB}$, and $\sigma_S = 3\sigma_{GB}$. For each case, the simulation ran until $t = 50$ s and the angle was measured by hand along the line $\phi = 0.5$.

3.3.1.2 Simulation Results

An example of the simulation evolution is given in Fig. 3.4. Also shown are a white line along the contour of $\phi = 0.5$ and the measured dihedral angle.

Fig. 3.5 shows how the neck width evolved in the three cases discussed in Sec. 3.3.1.1. For the GB-controlled case, Eq. (3.34) was fit to parameters $K = 2.99 \times 10^{-6}$ and $n = 7.42$. For the surface-controlled case, Eq. (3.34) was fit to parameters $K = 0.037$ and $n = 6.35$. The case with both GB and surface diffusion active behaved identically to the surface-controlled case. The GB-controlled case saw neck growth proceed at a significantly lower rate than the other cases. Considering the large difference between w_S and w_{GB} for UO_2 this is not surprising.

The first two seconds of the GB-controlled case requires further discussion. While the hyperbolic tangent profile used in the initial condition is a reasonable approximation, there is always an adjustment period at the beginning of a simulation. In many cases this has a negligible effect on the simulation results. But in the case of the GB-controlled simulation it caused some perturbation in the neck-width measurements.

Fig. 3.6 shows the results of the dihedral angle measurements from the simulation compared to the analytical expression in Eq. (3.35) and the experimental value for the given temperature. The maximum difference in the measured angle and the analytical expression is 15° at $\sigma_S/\sigma_{GB} = 1$. As the ratio increases, the agreement improves. Two factors play into this trend in the error. First, in Sec. 3.2.4 it was established that there is an inherit error in the surface energy caused by the surface–GB switching function used for implicit solvers. Theoretically this error should increase as σ_S/σ_{GB} increases.

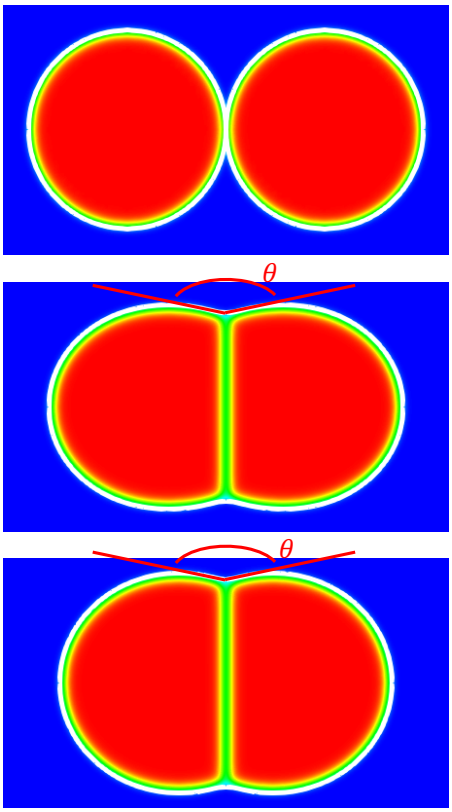

Figure 3.4. Demonstration of the two-particle symmetric simulation results. Coloring is according to the variable $\lambda = \sum \eta_i^2$, with a white line showing the position of $\phi = 0.5$. Based on the ϕ contour, the dihedral angle and neck width were measured. The dihedral angle stayed consistent once it reached equilibrium, even as the neck continued to grow. All images are taken from the case using the material parameters for UO_2, with similar microstructure evolution shown in the other cases. TOP: 0 s, MIDDLE: 1.8 s, BOTTOM: 3.5 s.

This would cause the trend to be less accurate angle measurements as σ_S/σ_{GB} increases. Another source of error in the angle measurement comes from the fact that the angle is measured by hand on a diffuse interface. As the angle sharpens the measurements become more difficult, causing the error to increase. This matches the trend seen in the results. It is also worth noting that the model predicted an angle of 156° for $\sigma_S/\sigma_{GB} = 2$, the energy ratio for UO_2, which is in good agreement with the measured angle for UO_2 of 163° [157].

3.3.2 Verification of Thermodynamics and Kinetics

In Sec. 3.1, it was established that two mechanisms which must be captured in sintering are the sintering stress and accelerated diffusion on GBs and surfaces. In this section, these behaviors are verified. The ability of the phase field model to accurately represent

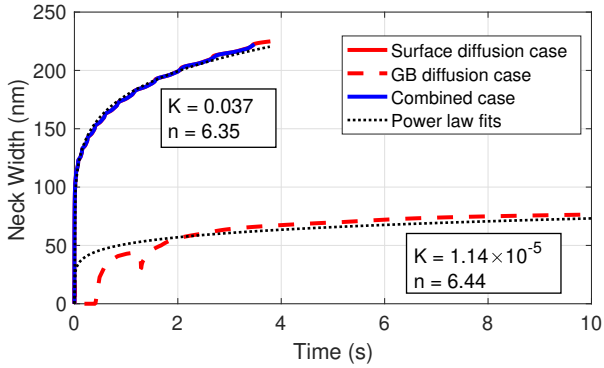

Figure 3.5. Evolution of the neck width with time for the surface diffusion case ($\sigma_{GB} = 1$), the GB diffusion case ($\sigma_S = 1$), and the combined case. Power law fits are also included. In the combined case, surface diffusion dominates, causing the behavior to almost perfectly match the surface-diffusion case. The GB diffusion case progressed much slower. In the GB diffusion case, adjustment of the interface from the initial condition near the beginning of the simulation had some impact on the measured neck width, causing a dip early in the plot.

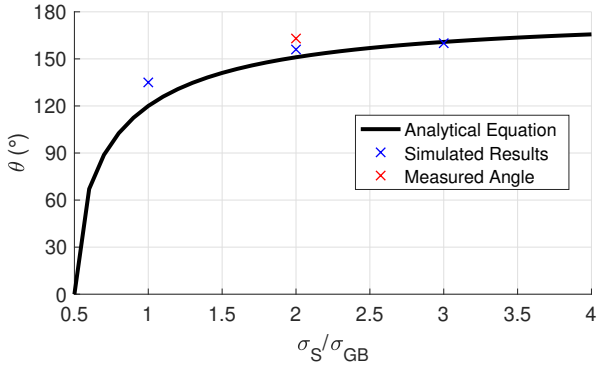

Figure 3.6. Dihedral angle measurements compared to the analytical expression which is a function of the surface to GB energy ratio (σ_S/σ_{GB}) and experimental measurement of dihedral angle. The simulated angle shows reasonable agreement with both the analytical expression and the experimental measurement for this temperature.

grain coarsening is well established and will not be investigated here [147, 151]. The sintering stress is primarily controlled by the surface and GB energies and non-uniform diffusion is controlled through the surface and GB diffusion weights. The effects of changing both of these factors will be quantified to determine if they change the sintering rate as expected.

This section also quantifies the difference these effects have in 2D and 3D simulations. 3D simulations are more accurate to real-world geometry, but 2D simulations have been commonly used in sintering models because they are computationally cheaper [39, 107, 108, 117, 119, 174]. The effects of dimensionality are quantified by replicating each

simulation in both 2D and 3D and comparing the results.

3.3.2.1 Simulation Descriptions

The first set of simulations tested the effects of changing the surface to GB energy ratio, σ_S/σ_{GB}. The difference between these two energies is the driving force for sintering, and therefore should affect the densification rate. The 2D simulations were set up with four circular particles with a uniform diameter of 300 nm arranged in a square formation. This created a closed pore in the center of the domain. The mesh was $(680\text{ nm})^2$ with $\ell = 40$ nm and $T = 1600$ K. Mesh adaptivity was used with elements ranging from $(10\text{ nm})^2$ to $(40\text{ nm})^2$. The simulation time was 400 seconds.

The 3D simulations used the same conditions described for the 2D simulations with some additions. Eight spherical particles were arranged in a cube formation. This creates an open pore, unlike the closed pore in the 2D simulations. The height of the mesh was 300 nm such that only half of each particle was inside the mesh. Zero-flux boundary conditions ensured that the top and bottom planes remained symmetry planes. This arrangement was chosen for three reasons:

- A smaller mesh reduces the computational cost
- The 2D simulation setup is equivalent to four 3D cylinders of infinite length. This 3D symmetric setup is also infinite in length.
- A direct comparison of the area of the closed pore in 2D and the volume of the open pore in 3D is not possible. Therefore, rather than measure the total pore volume, the 3D simulation measures the pore cross-sectional area along the top plane of symmetry. This area is equal to the 2D pore area at the initial condition, which allows for the areas to be determined in the same manner for direct comparison. The cross-sectional area will be referred to as the pore area to simplify discussion of the results.

Several different values of σ_S were used while σ_{GB} was held constant. A total of six simulations were performed. A pair (2D and 3D) of simulations with $\sigma_S/\sigma_{GB} = 1$, a pair with $\sigma_S/\sigma GB = 2$ (correct value for UO_2), and a pair with $\sigma_S/\sigma_{GB} = 3$ were carried out.

The second set of simulations used the same setup as the first set. However, rather than test the thermodynamic driving force, they tested the kinetic effects of the surface and GB diffusivities. Four additional simulation pairs were performed. In one 2D / 3D pair the surface diffusivity weight was set to $w_S = 1$ in order to isolate the effects of GB diffusivity. In the other pair the GB diffusivity was similarly set to $w_{GB} = 1$

to isolate surface diffusivity. These were then compared to the pair with both surface and GB effects, which is the second pair from the previous set of simulations. The GB diffusion-only case is not expected to sinter in either 2D or 3D. The shape evolution of particles relies on surface diffusion, and since this is retarded, the particles should not be able to pack together any tighter than their initial packing. The surface diffusion-only case is expected to sinter in 3D, but not in 2D. Vacancies from closed pores migrate primarily via GB diffusion. Without accelerated GB diffusion, the closed 2D pore would not be able to evacuate its vacancies. But the 3D open pore vacancies will still have a surface path that allows the pore to close.

The third set of simulations primarily examined the effect of geometry on grain coarsening during sintering. The 2D simulation had two non-uniform circular particles with diameters of 300 nm and 200 nm placed horizontally in a $(580\text{ nm})^2$ mesh. The interface width was $\ell = 40$ nm and the temperature was $T = 1816$ K. The 3D simulation was based on the 2D setup with the additions that the particles were hemispheres which used the plane of symmetry to reduce computational cost and the mesh height was 300 nm. The simulation terminated once the order parameter for the smaller particle had a maximum value below 0.5. The GB position was determined from the x-coordinate where $\eta_1 = \eta_2 \approx 0.5$ along the line $y = 290$, $z = 0$.

3.3.2.2 Simulation Results

Fig. 3.7 shows an example of microstructure evolution of the four-particle 2D simulations and the eight-particle 3D simulations used to quantify the effects of thermodynamics and kinetics. White circles in the center images show the pore areas that were measured in each simulation.

Fig. 3.8 shows plots of the pore area with time for the different energy ratios. The linear region of each curve was fit to a linear function of the form $A = p_1 t + p_2$ where A is the pore area and t is the simulation time. The fits are also shown in Fig. 3.8. The slopes are plotted vs energy ratio in Fig. 3.9. The slope magnitude increased as the energy ratio increased. This is the expected result and shows that the sintering stress is acting as a thermodynamic driving force for sintering.

The results for the set of simulations that tested the effects of diffusivity are given in Fig. 3.10. The red lines correspond to the black lines in Fig. 3.8. The 3D surface-controlled case exactly matches the 3D combined case, which suggests that the overall pore closure rate is surface-controlled. This behavior matches Fig. 3.5 which shows neck growth to be surface controlled. As expected, both the 3D GB-controlled diffusion case and the 2D surface-controlled diffusion case showed no pore closure. The most surprising result is

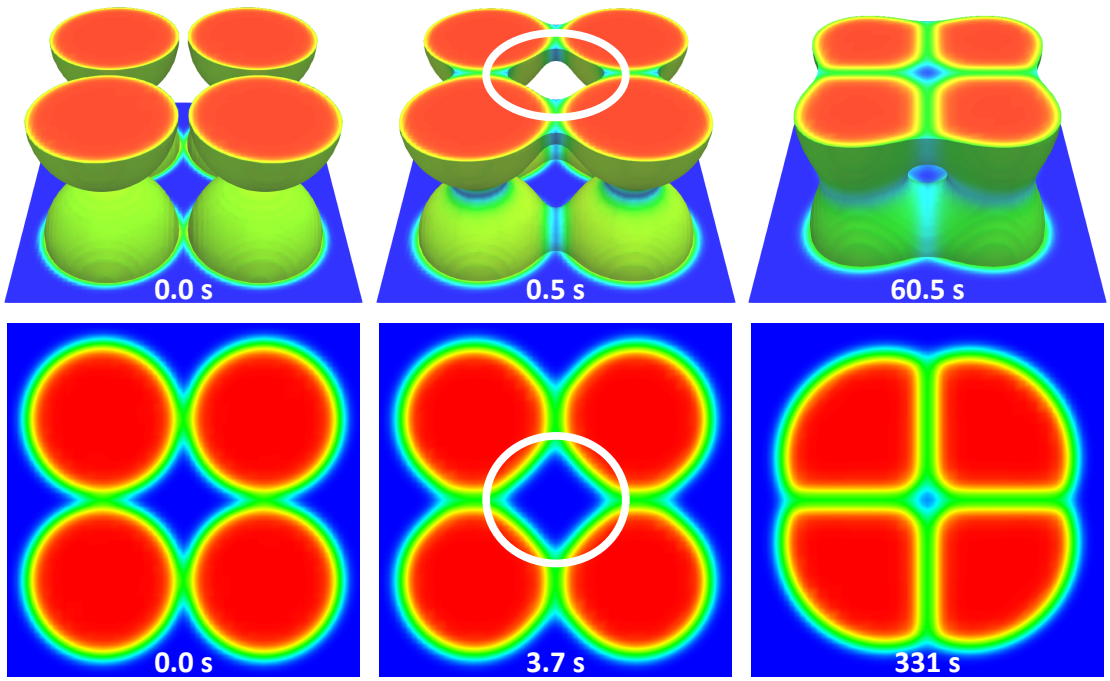

Figure 3.7. Demonstration of 2D and 3D pore closure simulations using $\sigma_S/\sigma_{GB} = 2$. TOP: 3D 8-particle simulation of pore closure. The bottom domain's surface is shown along with the region $\phi \leq 0.2$. BOTTOM: 2D 4-particle simulation of pore closure. In both cases the coloration represents the variable λ from Eq. (3.31). From left to right both rows show an initial condition, an intermediate stage, and the point of pore closure. The 2D pore area was compared against the 3D pore cross-section on the top surface of the domain. Both areas are circled in white in the two center images. The time of each image is given. Similar microstructures were produced for the other cases.

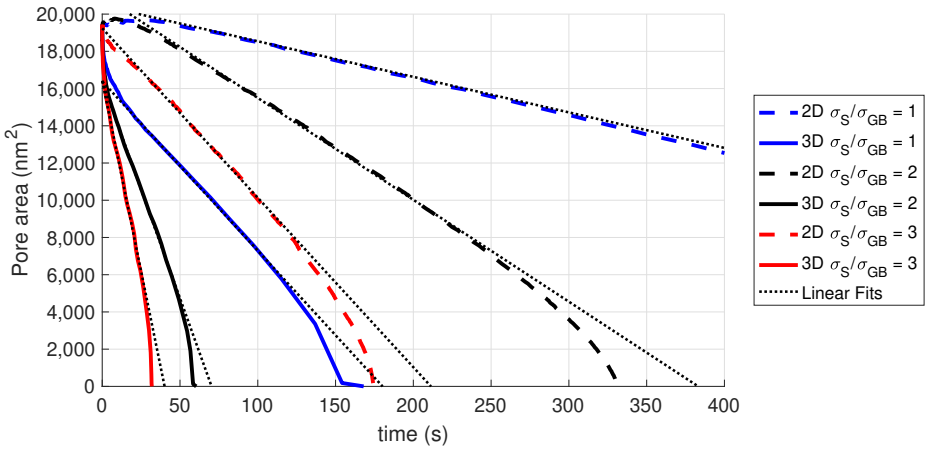

Figure 3.8. Pore area measurements for the 2D 4-particle and 3D 8-particle sintering stress simulations. In these simulations the surface to GB energy ratio, σ_S/σ_{GB} was varied to verify that the energy difference is acting as the driving force. The rate of pore closure increases as σ_S/σ_{GB} increases. Also shown are fits to the linear regions of each curve.

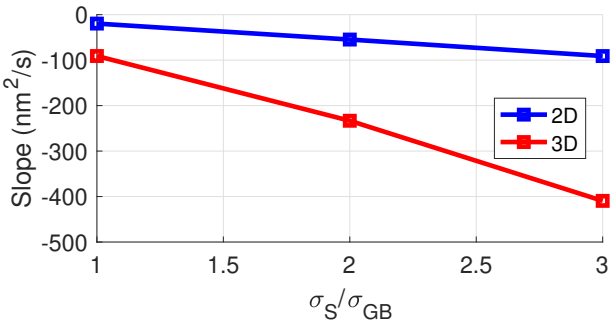

Figure 3.9. Slopes of the linear fits in Fig. 3.8 as a function of the surface to GB energy ratio. The change appears to be linear in 2D and nearly linear in 3D, but more data are needed to verify the trend.

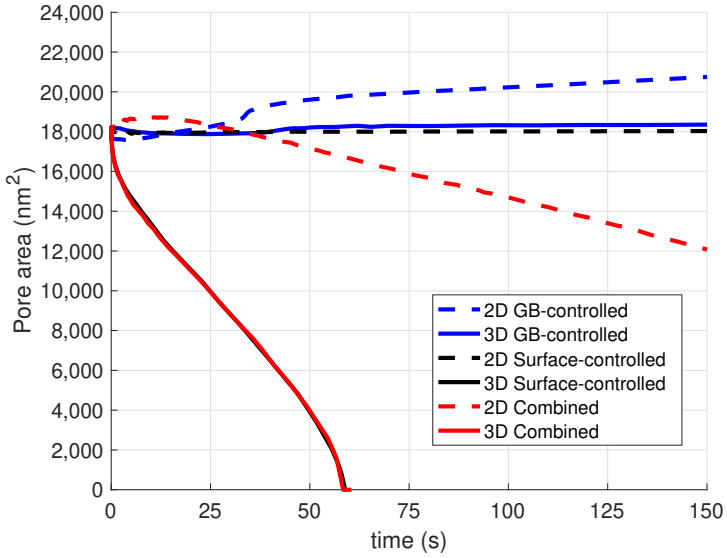

Figure 3.10. Results of 3D 8-particle and 2D 4-particle diffusivity simulations. In this set of simulations the surface and GB diffusivities were modified. In one pair of simulations the surface diffusion weight was changed to $w_S = 1$ in order to make it GB-controlled. In another pair the GB diffusion weight was changed to $w_{GB} = 1$ in order to make the process surface-controlled. The third pair used the weights described in Sec. 3.2.4 in order to include both effects. The third pair corresponds to the black lines in Fig. 3.8.

that the 2D GB-controlled case actually increased the pore area. The volume change was too large and long-lived to be explained by interface adjustments. Rather, it appears that the model decreased the overall energy of the system by diffusing vacancies from the exterior void to the interior pore along GBs. The causes of this result will be discussed more in depth in Sec. 3.3.3.

The linear fits for these simulations were not calculated because the red line fits are already included in Fig. 3.8, the black line fits have a slope of 0 in 2D and match the red

line in 3D, and the blue line fit for 3D also has a slope of 0. The only line where a slope fit would be yield new information is the one line with the positive slope.

Results for the simulations using asymmetric particles to measure grain coarsening are shown in Fig. 3.11. The microstructure evolution of the 2D and 3D cases are both shown at several intermediate times and the GB location as a function of time is also included. These results show that grain coarsening occurs much faster in 3D than in 2D. In 3D, the smaller grain has been completely consumed within 9.2 seconds; while in 2D, it takes 24.3 seconds. The larger surface area for vacancies to diffuse through in 3D appears to more than compensate for the increased volume that must be transported. However, the GB itself does not move as far in 3D. This appears to be related to the geometry. The radius for a circle with the area of two smaller circles is

$$r = \sqrt{r_1^2 + r_2^2}, \tag{3.36}$$

and the radius of a sphere with the volume of two smaller spheres is likewise

$$r = \sqrt[3]{r_1^3 + r_2^3}. \tag{3.37}$$

Based on these equations and the values used in the simulation, one would expect the GB to end near $x = 370$ nm in 2D and $x = 354$ nm in 3D. Each of these is slightly lower than the measured GB position, which is reasonable since the center of the particle is not fixed nor is the resulting particle perfectly spherical.

3.3.3 Discussion

A total of five sets of simulations have been used to verify that the grand potential model is accurately capturing sintering effects. The model makes reasonable predictions of the neck growth rate and the dihedral angle, compared to analytical models. In addition, the behavior of the sintering stress was consistent with expectations. Interestingly, the rate of the decrease in the pore area varied close to linearly with the GB to surface energy ratio. However, additional data would be needed to draw firm conclusions. The impact of the GB and surface diffusion also behaved as expected for most of the simulations. Also note that the behavior of surface and GB diffusion would be different in larger systems. Both open and closed pores exist in real compacts, such that both GB and surface diffusion are controlling the densification.

The only unexpected result was that a closed-pore 2D simulation of GB-only diffusion showed the void increase in size. Reverse sintering like this is a documented phenomenon [38]. However, the physics necessary for reverse sintering to be observed in experiments,

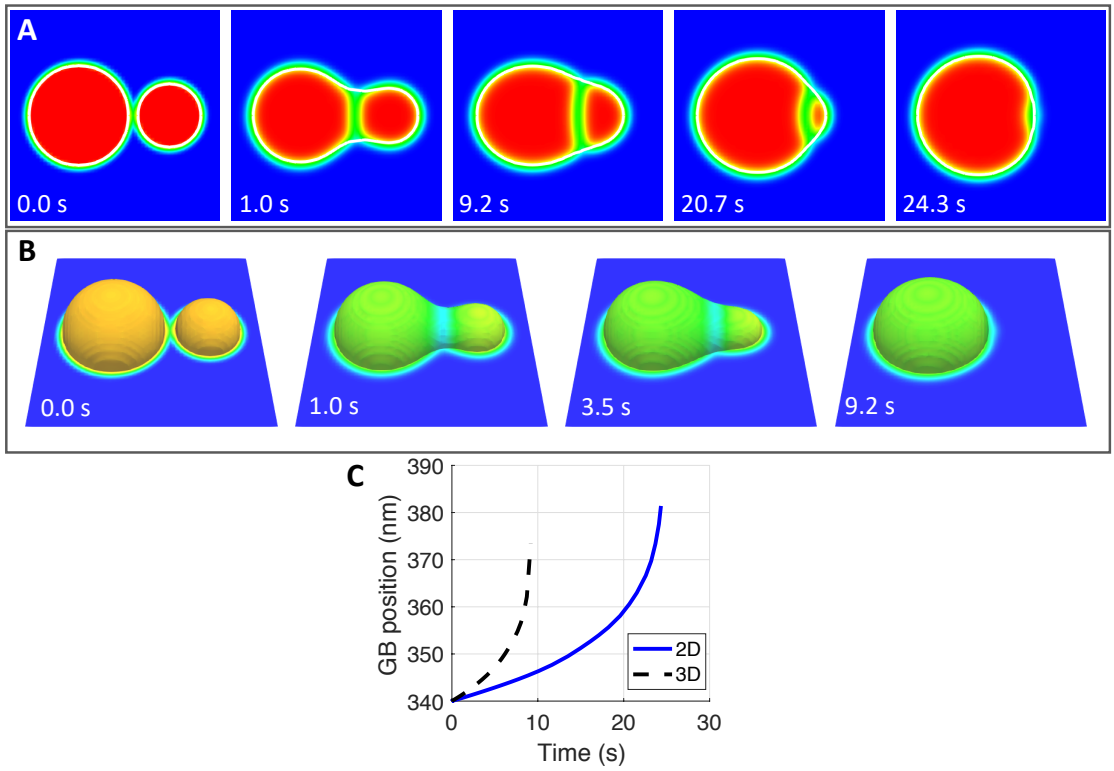

Figure 3.11. Results from 2-particle simulations using asymmetric particles. The particle radii are 150 nm and 100 nm with their initial contact point at x = 340 nm. A: 2D simulation with the line $\phi = 0.1$ shown in white. B: 3D simulations with the bottom surface of the domain and the surface $\phi = 0.1$ shown at several timesteps. C: Position of the GB as a function of time. The 3D case exhibits faster overall grain growth even though the GB does not move as far. In A and B the coloring is according to $\lambda = \sum \eta_i^2$.

such as high gas pressure and sudden temperature changes, were not present in the simulation. To study this further, the 2D GB-controlled case was simulated again, but allowed to continue until the pore closed. During the simulation, the total free energy of the system was calculated, as were the total bulk, surface, and GB energies, as shown in Fig. 3.12. Pore growth ceased after about 1,000 seconds and the pore closed after 10,800 seconds.

Interestingly, Fig. 3.12 shows that the surface energy decreased even as the pore area was increasing. This indicates that the pore shape change increased the pore area but decreased the amount of surface, thus being energetically favorable to the system. Fig. 3.12 also shows the microstructure at several times during the simulation. Unlike Fig. 3.7, the primary shape change occurs at the GBs, creating an X-shape at the end of the simulation rather than a circular shape. This is reasonable because the GBs are the major source of diffusion for the system. The GB motion may have helped the initially

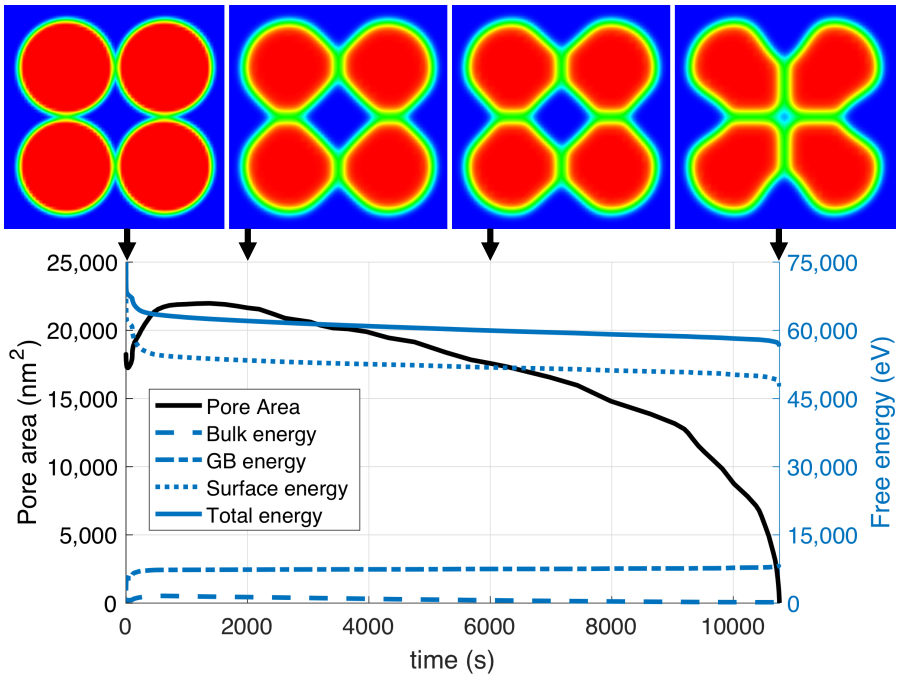

Figure 3.12. 2D GB-controlled case from Fig. 3.10 performed a second time for a longer time period. The black line shows the pore area over time. Pore growth occurs for the first 1,000 seconds before the pore begins to close. The blue lines show the bulk, GB, surface, and total energy of the simulation. The microstructure of the simulation is shown at four times with arrows pointing to their corresponding times on the graph. The pore changes from a concave shape at the initial condition to a convex shape. This causes the pore perimeter to decrease, which reduces the surface energy, while increasing the pore area. The microstructure evolution is much different than Fig. 3.7 where the final shape is a circle.

concave pore to form a convex shape with a larger area but smaller perimeter.

Based on the results of all of the simulations in this section, several conclusions can be drawn. First, the UO_2 parameters clearly exhibit surface diffusion-controlled kinetics. Not only is the surface diffusivity 1,000 times larger than the GB diffusivity, but both sets of simulations that compared surface-only diffusion to surface and GB diffusion showed identical results. Second, 3D effects are vitally important to get realistic results. All of the simulations that compared 2D and 3D behaviors showed 3D progressed significantly faster in terms of pore closure and GB motion. One cause for this is that pores that are closed off from the external surface in a 2D domain may be open to the external surface in a 3D domain. Since surface diffusion is the rate-controlling effect, this means that 2D domains will underestimate the closure rates of these pores Because of these geometric effects, any attempt at validating the model against experimental results will require 3D simulations.

3.4 Comparison Against Experiments

All computational models should be validated against experimental data to ensure their accuracy. While macroscale models like the master sintering curve have been well-validated [28], validation of microstructural models is more difficult. The MC Potts model has only been compared to data once [100] and no comparison to data has been carried out for phase field sintering models [1](Chapter 2).

There are three challenges when validating microstructural sintering models. First, a method is needed to create the structure of the initial powder compact. In a green body there are millions of individual particles of various sizes arranged in an unorganized lattice, and a method is needed to create a simulated compact with similar characteristics. Second, a method is needed for determining the compact volume that is similar to the approaches used in experiments. Third, the computational cost of representing the large number of particles found in actual green bodies is too high, and therefore the microstructural model represents the behavior in a much smaller body. Methods for handling the first two challenges are presented here, and the consequences of the third challenge are discussed.

In this section, an attempt is made to begin validating the grand potential sintering model using experimental data available in the literature. First, the approach taken to create the initial condition is described in Sec. 3.4.1 and the approach for measuring the volume in Sec. 3.4.2. The simulation is then described in Sec. 3.4.3 and the results are presented in Sec. 3.4.4. The results are discussed in Sec. 3.4.5.

3.4.1 Initial Condition Generation

A sintering simulation will not yield realistic results unless the initial condition (IC) meets the following criteria:

- The IC contains a reasonably large number of particles,
- The particles follow a realistic size distribution,
- The particles contact one another to form a single body without any particle overlap,
- The bulk density is approximately the same as real powder compacts,
- The particles do not form an organized lattice.

A particle packing algorithm was developed to generate ICs based on these criteria. It is demonstrated in Fig. 3.13. First, spherical particles are randomly sized according to a

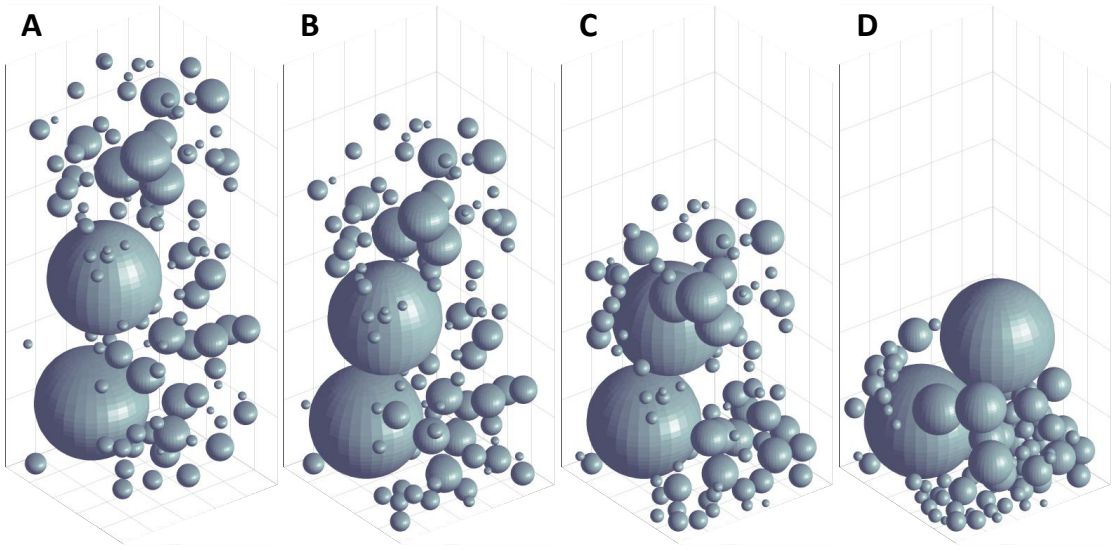

Figure 3.13. Demonstration of the algorithm used to generate ICs for sintering simulations. A: The particles are randomly placed such that no two overlap and all are completely inside the domain. B: A potential field pulls all of the particles down, and penalties are applied to prevent overlap and exits from the domain. C: Particles begin to gather at the bottom of the domain. D: The script finishes when no particle is able to move and minimize its potential. Any particles that are not in contact with the larger body (such as the one seen on the bottom right edge of D) are removed.

predetermined size distribution. Then, particles are placed, largest to smallest, in the domain at random positions one at a time. If a particle overlaps with a pre-existing particle, then the new particle is moved to a new location until one is found in which it does not overlap any other particles.

Once all of the particles are placed, a potential field is applied to the domain. The potential is lowest at the bottom and highest at the top. One at a time, the particles attempt to move a set distance down the potential gradient to lower their potential. If this movement causes the particle to leave the domain or overlap another particle, then a penalty is applied which increases the potential. The particle may then attempt to push other particles out of the way, calculate a new gradient which accounts for the field and the penalty and move again, or return to its original position. Particles continue cycling through this process until none of the particles can move.

Once the cycle is finished, particles that are not in contact with the main body of particles can be manually removed. Finally, the particle positions and radii are output to a text file that can be read by MARMOT and used to generate the simulation's IC.

3.4.2 Density Approximation

In experiments, there are typically two methods used to measure pellet volumes for density calculations [8]. First there is liquid immersion. A pellet is submerged in a liquid such as water and the volume change of the liquid is measured. The other method is to measure the pellet dimensions with a caliper or similar tool and calculate the volume. Both of these methods are difficult to replicate in a microstructural simulation. In the case of liquid immersion, the simplest computational method to replicate this would be a flood algorithm, which colors regions according to the dominant continuous variable [149]. Internal pores could then be separated from external pores based on continuousness. However, the initial condition method described above generates a completely open microstructure. A flood algorithm would classify the interconnected porosity as a single pore. In actual experiments, forces such as surface tension and gas bubbles would prevent complete wetting of the material, but a flood algorithm does not consider these effects.

Replicating a caliper measurement is complicated by the small number of particles, and thus the small length-scale, used in the phase field simulations. These very small green bodies will have a large amount of surface variation, as shown in Fig. 3.13. Caliper volume measurements will have a certain level of error based on the surface roughness of the pellet. For a typical green body, this error is negligible. However, for the small green bodies used in phase field simulations, this error becomes large. Any method to approximate the density based on the simulated microstructure must mitigate some of the effects of surface roughness.

A method was developed to approximate the density during simulated sintering. In the method, the volumes and centroids of each particle/grain are used to generate a sphere that has an equivalent centroid and volume. A convex hull is drawn around the centroids, eliminating surface roughness from the system. Finally, a MC integration technique is used to estimate the density [175] inside the convex hull. Points inside the hull are randomly sampled and the number of points that fall within the spheres are counted. Points that that fall within multiple spheres (since they only approximate the actual structure, and could thus overlap) are counted once for each of the overlapping spheres. This method is demonstrated in Fig. 3.14 by overlaying an image of the MC integration over an image of the microstructure.

3.4.3 Simulation Description

The simulation was designed to replicate the 1983 experiment described by Burk et al. [8]. This paper was chosen because it included particle size distribution measurements for

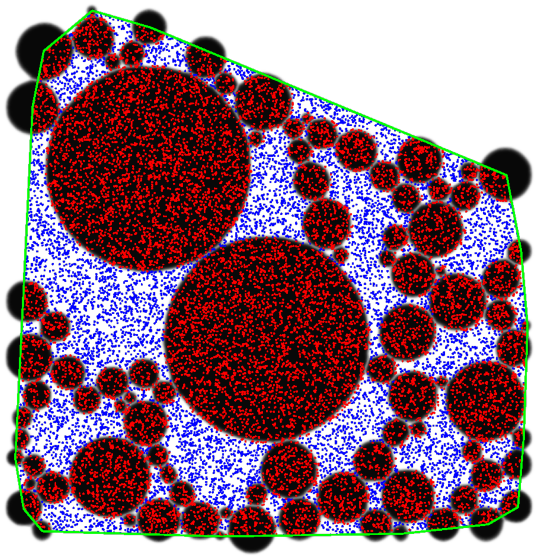

Figure 3.14. Demonstration of the MC density estimation technique created by overlaying an image of a convex hull and MC points over an image of the microstructure. A convex hull is wrapped around the grain centroids. Black regions are grains and white regions are voids. The hull is shown in green. Points inside the hull are randomly sampled. Points that fall within grains are marked in red and points in voids are marked as blue. The relative density is calculated by dividing the number of red points by the total number of points.

green pellets. Green pellets of stoichiometric UO_2 were heated at a rate of 4 K/min to 1973 K, held at this temperature for two hours, then cooled at a rate of 5 K/min back to room temperature. The particle size distribution was estimated based on the bimodal log-normal distribution from the paper [8]. The initial density was approximately 5.5 g/cm^3 (50.1%) and the final density was approximately 10.7 g/cm^3 (97.5%).

An IC was generated as described above using 120 particles randomly sampled from the distribution. Seven particles had to be removed because they were not in contact with the larger body of particles, resulting in a group of 113 particles inside a 5.52 µm by 5.52 µm by 6.48 µm domain. The interface width was set to $\ell = 120$ nm and a minimum diameter for the initial particles was set to 200 nm. Only 24 solid order parameters were used to represent the 113 particles to reduce computational cost, and the Grain Tracker algorithm in MARMOT [149] was used to avoid coalescence of particles.

3.4.4 Simulation Results

The evolution of the 113 particles was simulated using the same temperature conditions as the experiment, and all particles were maintained at the same temperature. The microstructure evolution of the simulation is shown in Fig. 3.15. The initial density was an exact match with the data. The particles coalesced and sintered as expected. However,

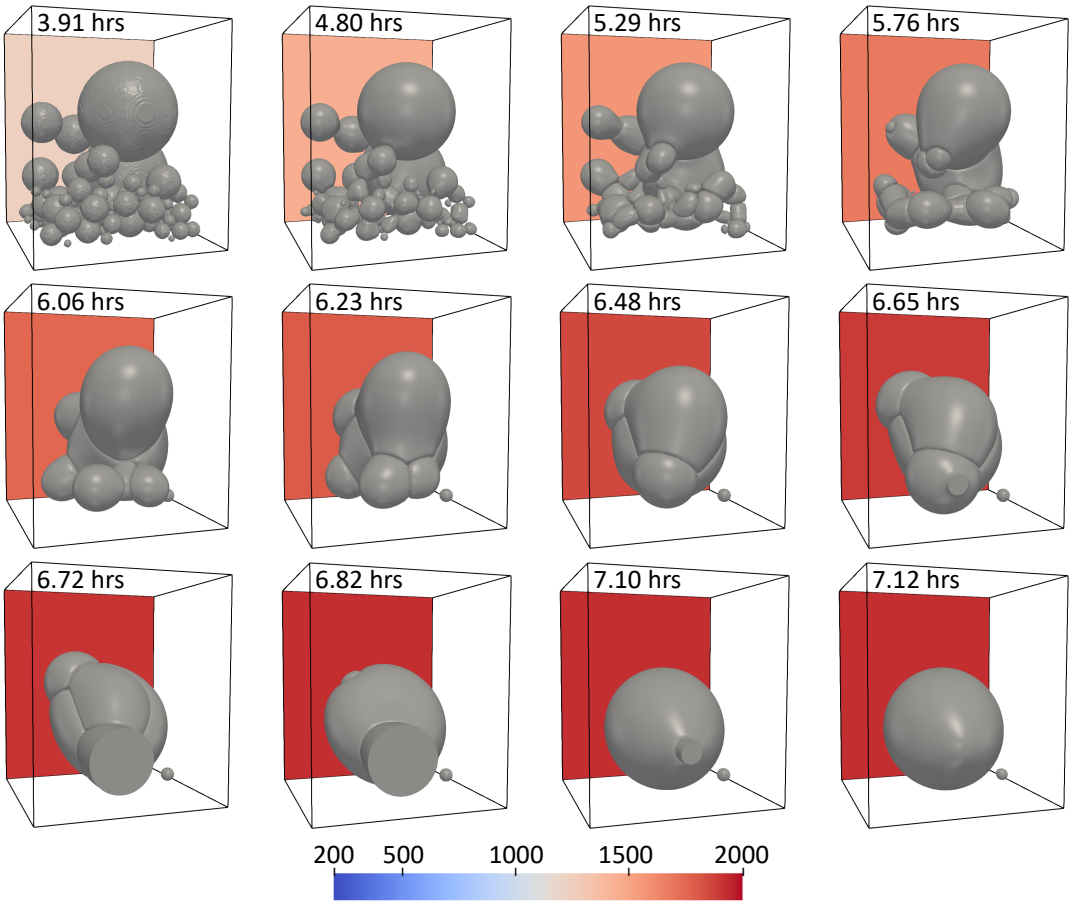

Figure 3.15. Evolution of the 113 particle sintering simulation. The microstructure is shown in gray. The back edge of the simulation domain is shaded by temperature. Some particles broke off from the main body, signifying the initial condition may have been a poor compact.

there are several particles that break from the main body. The smallest ones then shrink via mass diffusion through the void space, which is unphysical. This breakage suggests that the intial condition was a poor quality powder compact. In the initial compact, the small particles tended to be at the bottom of the simulation domain while larger particles tended to be near the top. This unequal distribution may help account for the poor compact quality.

The estimated density along with experimental data and the temperature profile are given in Fig. 3.16. All pores were eliminated before reaching the sintering temperature and the system spent the second half of the simulation at 100% theoretical density. The final relative density from the experiment was 97.5%.

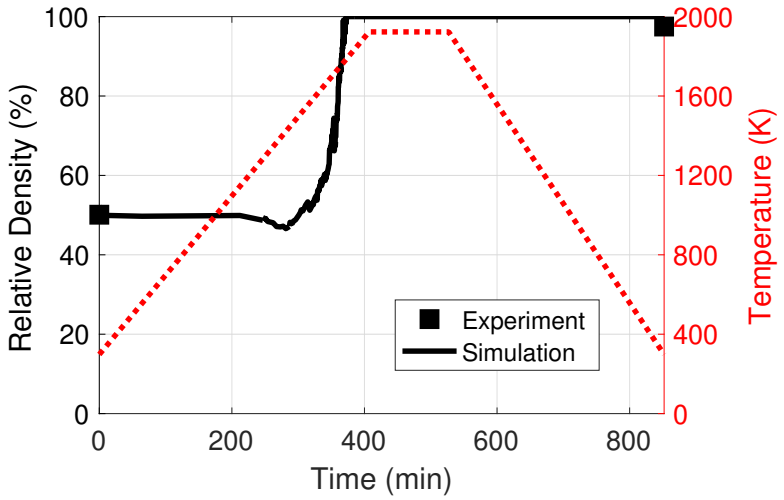

Figure 3.16. Relative density during the 113 particle sintering simulation, where the density was approximated using the method discussed in Sec. 3.4.2. The measured initial and final relative densities and the temperature profile from Ref. [8] are included for reference. The simulation had the correct initial density but the simulated body reached 100% density, while the experimental body only reached 97.5% density.

3.4.5 Discussion

The MC density approximation worked as intended, but it appears that the IC needs additional development. Some particles separated from the main body, and although the initial density was reasonable, the particles self-sorted by size. The mechanism of self-sorting is readily apparent. Small particles can travel through the spaces between the large particles, which allows them to reach the bottom of the domain where the potential field is lowest. However, self-sorting by size is not observed in experimental powder compact. It is possible that more mixing is necessary in the initial condition to more accurately capture the sintered microstructure.

The sintering rate of the simulation was physically reasonable, though the simulated body reached 100% relative density while the experiments did not. In addition, Fig. 3.16 shows that the body reached 100% density quickly, even before the end of the temperature ramp. One likely reason for this rapid densification is the small number of particles used in the simulation. Fewer particles means a higher fraction of open pores, which densify faster than closed pores, as well as shorter distances for vacancies to diffuse before reaching external surfaces, which also speeds up the kinetics. Using more particles for future simulations would result in a larger simulation domain and slower densification, but also higher computational cost. However, in our simulation, the small particles that resulted from the smaller side of the bimodal distribution combined with larger grains

quickly. By the time that significant densification started, at around 300 minutes, all grains with initial sizes less than 400 nm (about half of all the initial particles) had already been consumed. Thus, future simulations could sample particle sizes only from the larger half of the distribution, resulting in a larger domain with the same number of particles. An alternative approach to validating the model is to compare against data collected using small particle compacts, as done by Tikare et al. [100]. They compared against data from copper sintering of cylindrical green bodies with diameters of 40 to 60 µm that were characterized using X-ray synchrotron irradiation.

Another likely reason for the rapid densification is the large uncertainty in the measured property values that inform the diffusivity (see Fig. 3.2). The values used in this work may not have accurately described the diffusion behavior occurring in the experiments. If the diffusivity were lower, then the sintering rate would decrease. Uncertainty quantification needs to be carried out to quantify the impact of this property uncertainty on the density change predicted by the model.

The results from the new grand potential sintering model are promising. They show that the model does not experience the under-prediction of the densification rate found in previous phase field models without the Rigid Body Motion model. The results also indicate where modifications can be made to improve future predictions, mainly in increasing the size of the domain modeled and understanding the impact of the large parameter uncertainty. Once this improvements are made, future comparisons to data are needed to fully validate the model.

3.5 Conclusions and Future Work

A quantitative grand potential sintering model has been presented that captures the four driving mechanisms of sintering: sintering stress, vacancy/GB interaction, rapid diffusion on GBs and surfaces, and grain coarsening. Small test simulations were used to verify that these mechanisms are accurately captured in the model. Additional test simulations compared the model's behavior with analytical relations derived from sintering theory. In these tests, the model performed reasonably well.

Comparisons were also made to experimental data. First, the approaches taken for generating the IC and for quantifying the density were presented. However, the IC appears to have resulted in a poor initial compact, as some particles detached from the densifying body. The sintering rate was reasonable, clearly demonstrating that the grand potential model can accurately capture the sintering rate without requiring the Rigid Body Motion model. However, while the simulated final body reached 100% relative

density, the experiment only reached 98% density. In addition, the densification occurred too quickly. The cause of this is unclear, though it is likely related to the small size of the green body used in the simulation and the large uncertainty in the measured diffusion properties. The size of the green body could be increased without increasing the computational cost by neglecting small particles, which disappear quickly. Comparisons could also be made to data collected on green bodies that are the same size represented in the simulations. To reduce the property uncertainty, future experimental work and atomistic simulations should seek to determine these values with greater accuracy.

Chapter 4
Grand Potential Simulations of Doped-UO_2

4.1 Introduction

Multiple experimental studies have found that sintered UO_2 fuel pellets doped with chromium (Cr) are more dense and have larger grains than undoped fuels [36, 178–184]. Furthermore, it is known that both high density and large grains improve the behavior of in-pile UO_2 by reducing fission gas release and mechanical interactions with the cladding [185]. A fuel that reduces the plenum gap pressure and mechanical interactions with the cladding qualifies as a type of accident-tolerant fuel (ATF) [186]. Cr-doped UO_2 is an ATF concept that has been studied for near-term deployment in commercial nuclear reactors [180]. It is believed that reduced swelling will reduce interactions with the cladding [186] and the reduced fission gas release will lower the plenum gap pressure and reduce the likelyhood of cladding failure [187]. While Cr is the most widely studied dopant for UO_2, others have been identified and studied in experiments such as titanium (Ti) [178, 188, 189], magnesium (Mg) [178, 190], aluminum (Al) [178], iron (Fe) [178], and vanadium (V) [178]. Despite these studies, thermodynamic and kinetic mechanisms that cause the effects of the dopants have not been widely discussed or agreed upon [36, 191].

Recently, an explanation involving charged-interstitial defects was proposed for these dopant effects and was simulated using atomistic methods [191]. It was shown that at high temperatures the positively charged dopant ions can occupy interstitial lattice sites. In response to the extrinsic positive charge introduced by the interstitials and to maintain charge neutrality the Fermi level of the system is increased, enhancing the electron population. This change in the Fermi level enhances the concentrations of all negatively charged defects in the system, including U vacancies. The increased concentration of

U vacancies increases atomic self-diffusion; the principle driver of densification during sintering [1](Chapter 2). Multiple potential dopants were identified and simulated on the atomistic scale, including all of those listed above and manganese (Mn). These simulations found that V was the most efficient at increasing the U vacancy concentrations, followed by Mn and then Cr.

Unlike Cr and V, Mn has only previously been examined as a dopant in the oxide mixture MnO-Al_2O_3 for its low melting temperature in two-phase sintering [192, 193]. Solid-solution Mn-doped sintering experiments have not been reported in the literature.

In this chapter, we use the results of these atomistic studies to predict the microstructural sintering behavior of undoped, Cr-, and Mn-doped UO_2 fuels. To do this, we use the recently-developed grand potential sintering model (Chapter 3). The undoped and Cr-doped cases are used to qualitatively compare against existing experimental results. The Mn-doped case is included to determine the relative behavior of this potential dopant. V is not included in this study despite being the strongest dopant from Ref. [191] because it (a) has been studied in the past, and (b) is chemically dissimilar from Cr and Mn. This chemical difference would make accurate comparisons much more difficult to simulate. In Sec. 4.2, the atomistic results are used to extract the necessary vacancy concentrations for the undoped and doped comparisons. In Sec. 4.3, the grand potential sintering model is summarized and applied to this study. Secs. 4.4, 4.5, and 4.6 discuss the simulations used to compare the charged-defect predictions against experimental results.

4.2 Equilibrium Vacancy Concentrations

Fig. 6 of Ref. [191] shows the doped vacancy concentration to undoped vacancy concentration ratio as a function of temperature. These ratios were determined using the Busker potentials for vibrational entropy, which includes a description of Cr-O interactions. Fitting Arrhenius functions to these ratios for Cr and Mn yields the functions

$$\frac{c_{cr}^B}{c_{un}^B} = \begin{cases} 1.0, & 300K < T < 1803K \\ 8.78 \times 10^{19} \exp\left(\frac{-7.134eV}{k_B T}\right), & 1803K < T < 2000K \end{cases} \tag{4.1}$$

$$\frac{c_{mn}^B}{c_{un}^B} = \begin{cases} 1.0, & 300K < T < 1776K \\ 4.65 \times 10^{21} \exp\left(\frac{-7.617eV}{k_B T}\right), & 1776K < T < 2000K \end{cases} \tag{4.2}$$

where c_X^B is the equilibrium bulk U-vacancy concentration of species X (where X can be un for undoped, cr for Cr-doped, or mn for Mn-doped), T is the temperature, and k_B is

Boltzmann's constant.

The undoped U-vacancy equilibrium concentration was calculated using density functional theory (DFT) and the Cooper-Rushton-Grimes (CRG) potential for vibrational entropy, which provides a better description of the host UO_2 lattice and predicts higher uranium vacancy concentrations than the Busker potential [194–196]. That was then combined with Eqs. (4.1) and (4.2) to give

$$c_{un}^{B} = \begin{cases} 1.1185 \times 10^{-4} \exp\left(\frac{0.2134eV}{k_B T}\right), & 1000K < T < 1263K \\ 1.1772 \times 10^{-15} \exp\left(\frac{2.971eV}{k_B T}\right), & 1263K < T < 2000K \end{cases}, \tag{4.3}$$

$$c_{cr}^{B} = \begin{cases} c_{un}^{B}, & 1000K < T < 1803K, \\ 1.0335 \times 10^{5} \exp\left(\frac{-4.163eV}{k_B T}\right), & 1803K < T < 2000K \end{cases}, \tag{4.4}$$

$$c_{mn}^{B} = \begin{cases} c_{un}^{B}, & 1000K < T < 1776K, \\ 5.4800 \times 10^{6} \exp\left(\frac{-4.646eV}{k_B T}\right), & 1776K < T < 2000K \end{cases}. \tag{4.5}$$

Note that the defect concentration analysis results in positive exponents in the undoped case. This is because the oxidation energy is exothermic (negative) for UO_2 with an oxygen molecule as reference and because the model assumes a fixed partial pressure of oxygen, which results in more reducing conditions for increasing temperature. This has a large effect on the sintering rate in UO_2 [1](Chapter 2).

In addition to the bulk equilibrium concentrations, a grain boundary (GB) equilibrium concentration is also needed for the grand potential model (Chapter 3). We have previously assumed a constant, temperature independent value (Chapter 3). However, for the purposes of comparing the effects of various vacancy concentrations, assigning a uniform value to the rate-controlling equilibrium vacancy concentration would not be appropriate. Instead we assume a form of the GB equilibrium concentration that is a function of the bulk equilibrium concentration. A simple equation to accomplish this utilizes a constant positive GB segregation energy, E_{GB}, to attract additional vacancies:

$$c_X^{GB} = c_X^B \exp\left(\frac{E_{GB}}{k_B T}\right). \tag{4.6}$$

Since no value for E_{GB} has been determined through experiments or atomistic simulations, it is necessary to assume a value. We assumed a value of $E_{GB} = 1.5$ eV because this value gives physically reasonable results in the sintering temperature region. However, it gives unrealistically high concentrations at low temperatures. Therefore, an additional

constraint is placed on the GB equilibrium concentrations to mitigate these unrealistic values:

$$c_X^{GB} = \begin{cases} c_X^B \exp\left(\frac{1.5eV}{k_B T}\right), & c_X^B \exp\left(\frac{1.5eV}{k_B T}\right) < 0.1, \\ 0.1, & \text{otherwise} \end{cases}. \tag{4.7}$$

Fig. 4.1 shows the equilibrium bulk and GB concentrations using these equations for the undoped, Cr-doped, and Mn-doped cases.

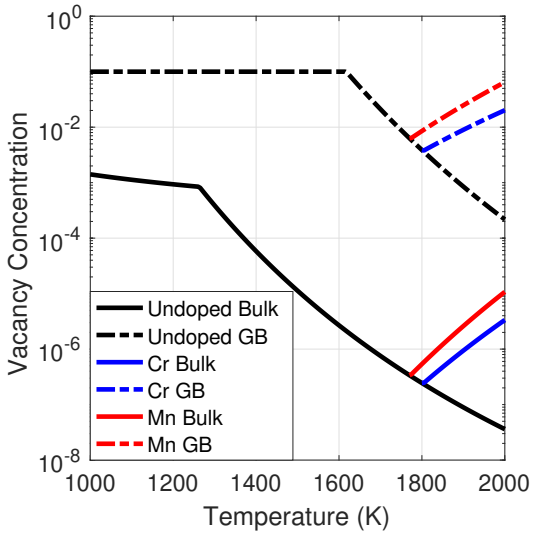

Figure 4.1. Equilibrium bulk and GB vacancy concentrations for undoped, Cr-doped, and Mn-doped cases. Dopants do not affect the vacancy concentration until high temperatures. The GB concentrations are capped at a value of 0.1 to prevent unrealistic concentrations at low temperatures.

One barrier to a direct comparison against experimental results is that Ref. [191] does not provide any set dopant concentrations. Rather, it assumes an ideal concentration in which all of the dopant dissolves into the lattice. This concentration was calculated from the point defect framework and varies with both dopant and temperature. Therefore, a relative comparison will be used to compare test simulations with experiments rather than a direct replication of experiments.

4.3 Grand Potential Model Description

The grand potential sintering model was defined in Chapter 3. It is based primarily on the grand potential model of Aagesen et al. [151], but also relies heavily on the works of Moelans [147] and Plapp [150]. This section gives an overview of the model without

including derivations or detailed descriptions. For more complete descriptions of the derivation of the grand potential model, see the cited works.

4.3.1 Governing Equations

The grand potential model is based on the phase field method. It utilizes continuous variable fields bounded by the values 0 and 1 with diffuse interfaces. There are two phases in the model. The solid phase, representing the UO_2 matrix, is described by n order parameters $\vec{\eta} = \{\eta_1, \eta_2, ..., \eta_n\}$. Each η order parameter represents a unique crystal grain. The void phase, representing pores and voids, is described by a single order parameter ϕ. Order parameters are non-conserved variables governed by the Allen-Cahn Equation [116],

$$\begin{aligned} \frac{\partial \eta_i}{\partial t} &= -L_s \frac{\delta \Omega}{\delta \eta_i}, \\ \frac{\partial \phi}{\partial t} &= -L_v \frac{\delta \Omega}{\delta \phi}, \end{aligned} \tag{4.8}$$

where L_s and L_v are the phase field mobilities of the solid and void phases and Ω is the grand potential function. Surfaces are the interfaces between ϕ and one or more η's while GBs are the interfaces between two or more η's.

The vacancies are defined in terms of their chemical potential μ, which is governed by the equation

$$\chi(\phi)\frac{\partial \mu}{\partial t} = \nabla \cdot \chi(\phi)\mathbf{D}(\phi, \vec{\eta}, \nabla\phi, \nabla\vec{\eta})\nabla\mu - \left(\frac{\partial \rho(\mu, \phi, \vec{\eta})}{\partial \phi}\frac{\partial \phi}{\partial t} + \sum_{i=1}^{n} \frac{\partial \rho(\mu, \phi, \vec{\eta})}{\partial \eta_i}\frac{\partial \eta_i}{\partial t} \right), \tag{4.9}$$

where χ is the susceptibility, $\mathbf{D}$ is the diffusivity tensor, and ρ is the atomic number density of vacancies. The grand potential function takes the form:

$$\Omega = \int_V \left[\epsilon(\phi) f_B(\phi, \vec{\eta}) + \kappa(\phi) f_{grad}(\nabla\phi, \nabla\vec{\eta}) + h_v(\phi)\omega_v(\mu) + (1 - h_v(\phi))\omega_s(\mu) \right] dV, \tag{4.10}$$

where f_B is the bulk free energy function, f_{grad} is the gradient energy function, and ϵ and κ are the bulk and gradient energy coefficient terms, respectively. h_v is a switching function that determines the current phase. ω_v and ω_s are the local potential densities for the void and solid phases, respectively. The bulk free energy function is defined as

$$f_B(\phi,\vec{\eta}) = \left(\frac{\phi^4}{4} - \frac{\phi^2}{2}\right) + \sum_{i=1}^{n}\left(\frac{\eta_i^4}{4} - \frac{\eta_i^2}{2}\right) + \frac{3}{2}\sum_{i=1}^{n}\eta_i^2\left(\phi^2 + \sum_{j>i}^{n}\eta_j^2\right) + \frac{1}{4}, \tag{4.11}$$

the gradient energy function is

$$f_{grad}(\nabla\phi,\nabla\vec{\eta}) = \frac{1}{2}\left[(\nabla\phi)^2 + \sum_{i=1}^{n}(\nabla\eta_i)^2\right], \tag{4.12}$$

and the local potential densities are

$$\begin{aligned}\omega_v(\mu) &= -\frac{1}{2}\frac{\mu^2}{V_a^2 k_{v,X}} - c_v^{eq}\frac{\mu}{V_a}\\ \omega_s(\mu,\vec{\eta}) &= -\frac{1}{2}\frac{\mu^2}{V_a^2 k_{s,X}} - c_{s,X}^{eq}(\vec{\eta})\frac{\mu}{V_a}\end{aligned} \tag{4.13}$$

where V_a is the atomic volume of U, $k_{s,X}$ and $k_{v,X}$ are parabolic constants, and $c_{s,X}^{eq}$ and c_v^{eq} are the equilibrium atomic vacancy concentrations for both phases. Note that atomic densities and atomic concentrations are interchangeable according to $c = V_a\rho$.

4.3.2 Quantitative Parameters

There are two vacancy number densities, one for each phase, which are calculated according to

$$\begin{aligned}\rho_s(\mu,\vec{\eta}) &= \frac{\mu}{V_a^2 k_{s,X}} + \frac{c_s^{eq}(\vec{\eta})}{V_a}\\ \rho_v(\mu) &= \frac{\mu}{V_a^2 k_{v,X}} + \frac{c_v^{eq}}{V_a}\\ \rho(\mu,\phi,\vec{\eta}) &= h_v(\phi)\rho_v(\mu) + (1-h_v(\phi))\rho_s(\mu,\vec{\eta})\end{aligned} \tag{4.14}$$

The susceptibility from Eq. (4.9) is defined as

$$\chi(\phi) = \frac{1}{V_a^2}\left(\frac{h_v(\phi)}{k_{v,X}} + \frac{1-h_v(\phi)}{k_{s,X}}\right). \tag{4.15}$$

The bulk and gradient energy coefficients are

$$\epsilon(\phi) = h_S(\phi)\epsilon_S + (1-h_S(\phi))\epsilon_{GB}$$

$$\kappa(\phi) = h_S(\phi)\kappa_S + (1 - h_S(\phi))\kappa_{GB} \tag{4.16}$$

where h_S is a switching function that distinguishes between solid/void surfaces and solid/solid grain boundaries. ϵ_S and κ_S are coefficients that depend on the surface energy and ϵ_{GB} and κ_{GB} depend on the GB energy. These can be calculated according to

$$\begin{aligned} \epsilon_S &= 6\frac{\sigma_S}{\ell} & \epsilon_{GB} &= 6\frac{\sigma_{GB}}{\ell} \\ \kappa_S &= \frac{3}{4}\sigma_S\ell & \kappa_{GB} &= \frac{3}{4}\sigma_{GB}\ell \end{aligned} \tag{4.17}$$

where σ_S and σ_{GB} are the surface and GB energies, respectively, and ℓ is the phase field interface width. In reality, σ_{GB} depends on the degree of misorientation between the two grains, but it is assumed constant for the sake of simplifying the model [113].

The switching functions h_v and h_S are both based on the same function:

$$H(\phi, \phi_0) = \begin{cases} 0, & \phi \leq 0 \\ 1, & \phi \geq \phi_0 \\ 6\left(\frac{\phi}{\phi_0}\right)^5 - 15\left(\frac{\phi}{\phi_0}\right)^4 + 10\left(\frac{\phi}{\phi_0}\right)^3, & 0 < \phi < \phi_0 \end{cases} \tag{4.18}$$

where ϕ_0 is a constant between 0 and 1. The two switching functions are then $h_v(\phi) = H(\phi, 1)$ and $h_S(\phi) = H(\phi, 0.3)$.

The equilibrium vacancy concentration for the solid phase has two values. Eqs. (4.3), (4.4), and (4.5) give values for the bulk concentrations with the various dopants, while Eq. (4.7) modifies them for GBs. Therefore, $c_{s,X}^{eq}$ must distinguish between grain interiors and GBs. We do this with the function:

$$c_{s,X}^{eq}(\vec{\eta}) = c_X^B + 4\left(c_X^{GB} - c_X^B\right)\left(1 - \lambda(\vec{\eta})\right)^2, \tag{4.19}$$

$$\lambda(\vec{\eta}) = \sum_{i=1}^{n} \eta_i^2. \tag{4.20}$$

The void vacancy equilibrium concentration, on the other hand, is simply set to $c_v^{eq} = 1$. This formulation will also increase the equilibrium vacancy concentration on surfaces. This should have a small effect on the profile, however, due to the high equilibrium vacancy concentration in the void phase. However, it may also increase the surface diffusion rate. The effects of dopants on surface diffusion have not been studied experimentally, so this behavior may or may not be physically accurate.

The phase field mobilities are defined as

$$L_s = \frac{4}{3}\frac{c_{s,X}^{eq}}{c_{s,un}^{eq}}\frac{M_{GB}}{\ell},$$
$$L_v = 40L_s, \tag{4.21}$$

where M_{GB} is the solid-phase GB mobility in the undoped solid. It is known that higher vacancy concentrations increase the GB mobility [197]. The GB mobility is a linear function of the self-diffusion coefficient, which for UO_2 is a linear function of the fraction of lattice sites occupied by vacancies [198]. Therefore, in Eq. (4.21), we assume there is a linear relationship between L_s and $c_{s,X}^{eq}$. We also assume that the presence of dopants does not affect the GB mobility through any other mechanism. Also, the void phase mobility, L_v, is not a physical parameter. It is needed for the phase field method to describe the evolution of the void phase, but the only constraint is that it is large enough not to artificially slow the evolution of the solid phase. Therefore, it is set to be larger than L_s by a factor of 40. M_{GB} is calculated according to the Arrhenius function:

$$M_{GB} = M_0 \exp\left(\frac{-Q}{k_B T}\right), \tag{4.22}$$

where M_0 is the mobility prefactor and Q is GB mobility activation energy.

The diffusivity tensor from Eq. (4.9) enables the model to represent accelerated diffusion along GBs and surfaces. It is taken from Ahmed et al. [148]:

$$\begin{aligned}
\mathbf{D}(\phi, \vec{\eta}, \nabla\phi, \nabla\vec{\eta}) &= \mathbf{D}_B + \mathbf{D}_{GB}(\vec{\eta}, \nabla\vec{\eta}) + \mathbf{D}_S(\phi, \nabla\phi) \\
\mathbf{D}_B &= D_B\mathbf{I} \\
\mathbf{D}_{GB}(\vec{\eta}, \nabla\vec{\eta}) &= w_{GB}D_B\sum_{i=1}^{n}\sum_{j\neq i}^{n}\eta_i\eta_j\mathbf{T}_{GB}^{ij}(\nabla\eta_i, \nabla\eta_j) \\
\mathbf{D}_S(\phi, \nabla\phi) &= w_S D_B\phi^2(1-\phi)^2\mathbf{T}_S(\nabla\phi),
\end{aligned} \tag{4.23}$$

where $\mathbf{D}_B$, $\mathbf{D}_{GB}$, and $\mathbf{D}_S$ are the bulk, GB, and surface diffusion tensors, respectively. w_{GB} and w_S are weights used to estimate the GB and surface diffusion magnitudes based on the bulk diffusion magnitude, D_B. We assume that the dopants do not affect the self-diffusion coefficient directly, and we can thus use the same diffusion values for each case. $\mathbf{I}$ is the identity tensor, $\mathbf{T}_{GB}^{ij}$ is the normalized GB directional tensor for the η_i/η_j GB, and $\mathbf{T}_S$ is the normalized surface directional tensor. These two directional tensors

are defined as

$$\mathbf{T}_{GB}^{ij}(\nabla\eta_i, \nabla\eta_j) = \mathbf{I} - \frac{\nabla\eta_i - \nabla\eta_j}{|\nabla\eta_i - \nabla\eta_j|} \otimes \frac{\nabla\eta_i - \nabla\eta_j}{|\nabla\eta_i - \nabla\eta_j|},$$
$$\mathbf{T}_S(\nabla\phi) = \mathbf{I} - \frac{\nabla\phi}{|\nabla\phi|} \otimes \frac{\nabla\phi}{|\nabla\phi|}. \tag{4.24}$$

Finally, the bulk diffusion magnitude is an Arrhenius function:

$$D_B = D_0 \exp\left(\frac{-E_m}{k_B T}\right), \tag{4.25}$$

where D_0 is the diffusivity prefactor and E_m is the vacancy migration energy.

This model and its derivatives are implemented in the implicit FEM phase field code MARMOT [154]. MARMOT is used to perform all of the following simulations.

4.3.3 Material Values

Most of the values used for this model are available in the literature. These are given in Table 4.1. The parabolic constants, however, must be calculated separately. The constants come from the parabolic free energy curves [150]. Parabolic curves are used because they are more forgiving of rounding error than the ideal solution free energy or the dilute species free energy. We obtained the values by doing a least-squares fit against the ideal solution model for each species according to the equations in [150]. We calculated $k_{s,X}$ in this manner for all three species and a variety of temperatures across the temperature region, then fit them to linear curves of the form $k_{s,X} = m_X T + b_X$. The parameters obtained from the curve fits are shown in Table 4.2. The void phase does not have an ideal energy, so the void versions are assumed to be $k_{v,X} = 10k_{s,X}$. This ensures the void phase stays near equilibrium.

Name	Value	Units	Ref
σ_{GB}	9.86	eV/nm^2	[158]
σ_S	19.7	eV/nm^2	[157]
V_a	0.04092	nm^3	[159]
M_0	1.4759×10^9	nm^4/eVs	[160]
Q	2.77	eV	[160]
D_0	8.33×10^9	nm^2/s	Chapter 3
E_m	3.608	eV	Chapter 3
w_{GB}	10^6	–	Chapter 3
w_S	10^9	–	Chapter 3

Table 4.1. Constant values associated with UO_2 used with the present model

X	$\mathbf{m}_X$ (eV nm^{-3}s^{-1})	$\mathbf{b}_X$ (eV nm^{-3})	**Temperature** (K)
un	0.051	-15.40	1000 – 1263
un	0.211	-217.35	1263 – 2000
cr	-0.104	340.02	1803 – 2000
mn	-0.104	340.02	1776 – 2000

Table 4.2. Linear fit parameters for parabolic energy coefficients of the form $k_{s,X} = m_X T + b_X$. The values are based on a least-squares fit to the ideal solution model. The two dopants have the same fit because their ideal solution free energies are very similar.

The parameters ℓ and T are not given here as they vary based on the specific problem. They are given in the descriptions of the individual simulations.

4.4 Dopant Effects on Pore Closure Rate

According to results from Bourgeois et al. [36] and Arborelius et al. [180], Cr-doped fuel densifies at a slightly higher rate than undoped fuel at sintering temperatures. At the end of heating, Bourgeois et al. found that Cr-doped fuel was about 2% more dense. Arborelius et al. similarly found that after sintering, Cr-doped fuel was about 1% more dense than undoped fuel. It is therefore necessary to determine the effect of dopants on the sintered density according to the grand potential sintering model.

4.4.1 Simulation Setup

Eight uniform spherical particles, 300 nm in diameter, are arranged in a cube formation. The interface initial condition (IC) is set to match a hyperbolic profile, which is a good approximation for the actual profile of phase field interfaces [155]. The interface thickness is set to 40 nm and the simulated temperature to 1900 K. The domain is a cube with side lengths of 680 nm. Mesh adaptivity is used with the individual mesh elements side lengths ranging from 10 to 40 nm.

The pore is the space at the center of the 8 particles. In the IC, the pore is open to the external void surrounding the particles. In order to estimate the volume of the open pore, a 300 nm cubic box is defined with corners at the IC sphere centers. The pore volume is estimated by integrating over the void variable within this box according to

$$V_{pore} = \int_{V_{box}} \phi dV. \tag{4.26}$$

Each simulation is allowed to continue until $V_{pore} = 0$.

4.4.2 Simulation Results

Fig. 4.2 shows an example of the simulation progression with the pore visibility increased by removing two particles. In every case, at or around two seconds of simulation time, the particles have coalesced to the point of closing off the pore from the exterior void. At this point the kinetics of the simulation changes. When the pore is open to the external void, vacancy diffusion is rate-controlled by surface diffusion (Chapter 3). Once the pore is closed there is no surface path to the external surface, and the vacancy diffusion is rate-controlled by GB diffusion. Fig. 4.3 shows the measured pore volume for all three simulations. The transition from S- to GB-controlled kinetics is plainly visible.

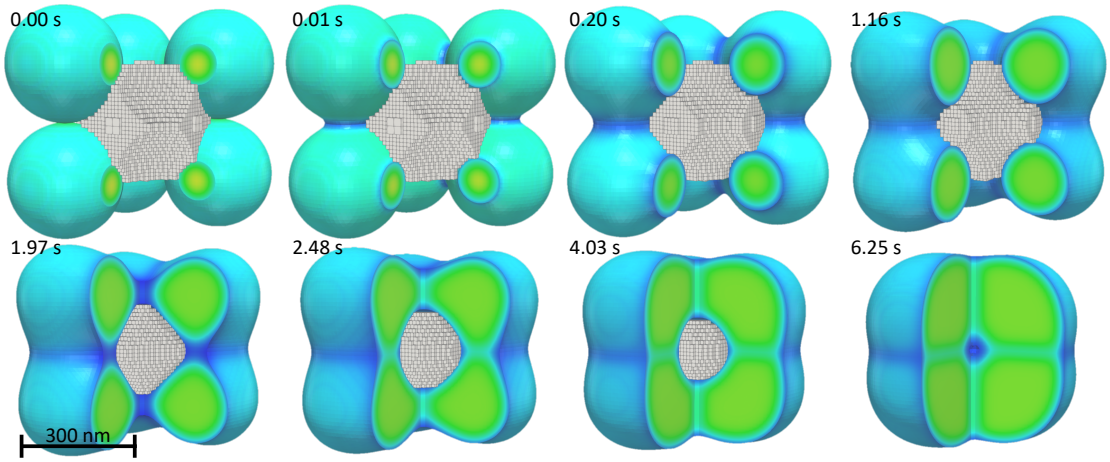

Figure 4.2. Demonstration of 8-particle pore-closure simulations. Two of the particles are not shown so that the pore is more clearly visible. These images are taken from the Cr-doped case at the times shown. The undoped and Mn-doped cases yield similar microstructures, but evolve at different rates. The pore volume is calculated according to Eq. (4.26).

In addition to the simulations, Fig. 4.3 also shows linear fits to the pore volume change based on the two kinetic-control regions. The linear fit parameters are given in Table 4.3.

	Surface-controlled		**GB-controlled**	
X	$\mathbf{m}_X$ ($\mathrm{nm^3 s^{-1}}$)	$\mathbf{b}_X$ ($\mathrm{nm^3}$)	$\mathbf{m}_X$ ($\mathrm{nm^3 s^{-1}}$)	$\mathbf{b}_X$ ($\mathrm{nm^3}$)
un	-3.339×10^6	1.289×10^7	-1.027×10^6	7.614×10^6
cr	-3.870×10^6	1.294×10^7	-1.216×10^6	7.698×10^6
mn	-3.918×10^6	1.291×10^7	-1.377×10^6	7.817×10^6

Table 4.3. Fitting parameters of the form $V_{pore} = m_X t + b_X$ for the 8-particle pore closure simulations. Two sets of parameters are calculated: One for the surface mobility-controlled region and another for the GB mobility-controlled region.

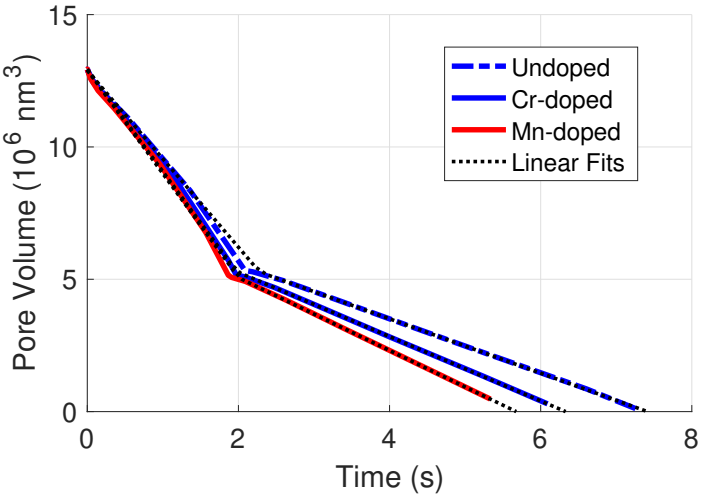

Figure 4.3. Measured pore volume of 8-particle pore closure simulation for undoped, Cr-doped, and Mn-doped simulations. Initially, the rate is controlled by the surface diffusivity. However, after about two seconds the particles coalesce to the point where the pore is closed and the rate transitions to GB diffusivity-controlled. Linear fits were calculated for both regions with the fitting parameters given in Table 4.3.

4.4.3 Discussion

The pore closure rate for the Cr-doped case is 15.9% faster than the undoped case in the surface-controlled region and 18.4% faster in the GB-controlled region. The rates for the Mn-doped case are 17.3% and 34.1%, respectively. These increased rates are a result of the charged-interstitial mechanism increasing the vacancy concentration in the doped cases. To convert to a density measurement, the ratio of solid to total sintered volume is used:

$$\rho^* = \frac{V_{solid}}{V_{solid} + V_{pore}} \tag{4.27}$$

where V_{solid} is the combined volume of the eight particles. This equation converts Fig. 4.3 to density measurements as shown in Fig. 4.4. The spread of relative density is much smaller than the range of pore volumes and appear to agree well with experiments.

The results are encouraging. However, these small simulations are poor comparisons to experimental data. As was discussed in Chapter 3, effects such as surface roughness make accurate density measurements difficult, even for much larger simulations. For example, if the density was measured only inside the same box used to measure V_{pore}, then the relative densities would have a much greater spread. Additionally, these are small particles at constant high temperature that sinter very quickly. If the particles

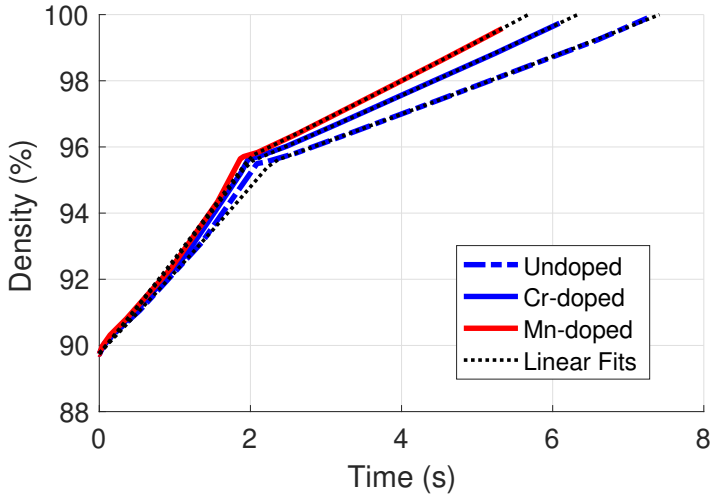

Figure 4.4. Conversion of Fig. 4.3 to a density calculation using Eq. (4.27).

were larger or the temperature lower, then the results could be affected. Thus, before any firm conclusions can be drawn about the densification rate, a larger simulation should be performed. First, though, we measure the grain growth rate.

4.5 Dopant Effects on Grain Growth

While the densification rate is only slightly affected by dopants, the grain growth rate is greatly affected. Bourgeois et al. found that the optimum Cr concentration increased the grain size by up to a factor of 7 during constant-temperature annealing [36]. Arborelius et al. found that the size could increase by up to a factor of 5 during annealing [180]. Even the atomistic simulations from Ref. [191] found that at 1900 K the presence of Cr should increase the grain size by a factor of 2.1 and that Mn should increase it by a factor of 3.9 [191]. Therefore, a set of simple 2D grain growth simulations are used to estimate the grain size during annealing.

4.5.1 Simulation Setup

To estimate grain growth, a fully-dense single phase simulation is set up. Using a single phase allows the model to be significantly simplified to the point of being a standard phase field simulation. Since there is no void phase, vacancies do not need to be tracked explicitly, and the variables ϕ and μ can be removed. This completely negates the need for Eqs. (4.9), (4.13), (4.14), (4.15), (4.18), (4.19), (4.23), (4.24), and (4.25). In addition, Eq. (4.10) is simplified to

$$\Omega = \int_V \left[\epsilon_{GB} f_B(\vec{\eta}) + \kappa_{GB} f_{grad}(\nabla\vec{\eta})\right] dV, \tag{4.28}$$

with

$$f_B(\vec{\eta}) = \sum_{i=1}^{n} \left(\frac{\eta_i^4}{4} - \frac{\eta_i^2}{2}\right) + \frac{3}{2}\sum_{i=1}^{n}\sum_{j>i}^{n} \eta_i^2\eta_j^2 + \frac{1}{4} \tag{4.29}$$

$$f_{grad}(\nabla\vec{\eta}) = \frac{1}{2}\sum_{i=1}^{n} (\nabla\eta_i)^2 . \tag{4.30}$$

The simulations use a square domain with a sidelength of 35 μm, periodic boundary conditions, and 4,000 grains randomly generated using a Voronoi tessellation. All three simulations use the same initial condition. The temperature starts at 1200 K and increases linearly such that after 400 seconds the temperature is 1900 K. The temperature remains at 1900 K for the remainder of the simulation. The short heating period provides time for the formation of the diffusion interface from the initially sharp interfaces that result from the tessellation.

The interface width is set to $\ell = 100$ nm. Mesh adaptivity is again used with square elements ranging in size from 25 nm to 200 nm. Only 10 order parameters are used, with grain coalescence prevented by the GrainTracker algorithm built into MARMOT [149]. GrainTracker also counts the number of grains, both inside the domain and across the periodic boundaries. The average grain area is calculated as $A_{avg} = (35\ \mu\text{m})^2/n_{grains}$. The average grain size is then calculated as $d_X = \sqrt{4A_{avg}/\pi}$.

4.5.2 Simulation Results

The average grain size for the undoped, Cr-doped, and Mn-doped simulations are shown in Fig. 4.5 starting at 400 seconds when the simulations reaches constant temperature. The grain sizes are fitted to curves of the form $d_X = a_X\sqrt{t} + b_X$, where d_X is the grain size of case X. The fitting parameters are given in Table 4.4. This form was chosen because the measured grain area showed highly linear behavior and calculating the grain size requires taking the square root of the grain area. The doped cases obviously grow significantly faster than the undoped case. Images of the microstructures at the initial condition and at 530 s (the maximum time reached by the Mn-doped simulation) are shown in Fig. 4.6. These images also show a stark difference in the grain size between the different cases.

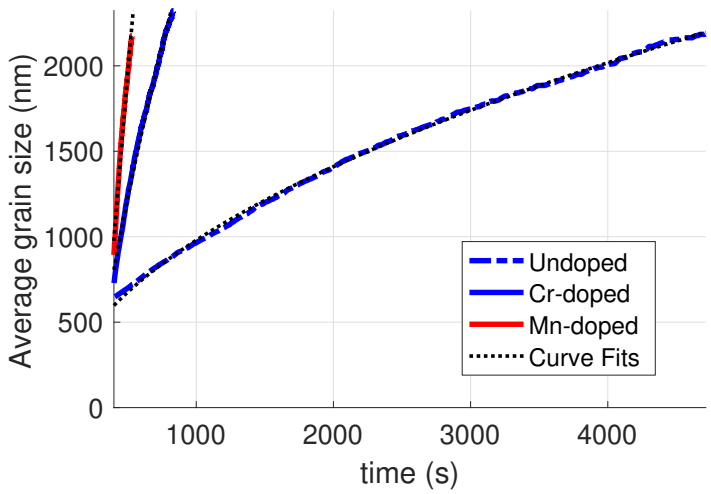

Figure 4.5. Average grain size for undoped, Cr-doped, and Mn-doped grain growth simulations at 1900 K. The Cr-doped and Mn-doped cases both see highly accelerated grain growth. Functional fits are included for each curve in order to compare the relative grain sizes.

X	$\mathbf{a}_X$ (nm s^{-1})	$\mathbf{b}_X$ (nm)
un	32.85	-59.54
cr	176.5	-2,724
mn	414.2	-7,308

Table 4.4. Fitting parameters of the form $d_{grain} = a_X\sqrt{t} + b_X$ for the average grain size in the three grain growth simulation cases.

4.5.3 Discussion

In order to compare the relative grain sizes, we take the limit

$$\lim_{t\to\infty} \frac{d_X}{d_{un}} = \frac{a_X}{a_{un}}, \tag{4.31}$$

where d_X is the grain size associated with dopant X, and a_X is the fitting parameter from Table 4.4. According to this, the Cr-doped case is expected to have a grain size 5.4 times larger than the undoped case. For the Mn-doped case the ratio is 12.6. The charged-interstitial model increases the grain growth rate because the increased vacancy concentration also increases the GB mobility (see Eq. (4.21)). This result for the Cr-doped case is consistent with the results of Bourgeois et al. [36] and Arborelius et al. [180].

It is important to note two factors which are not being accounted for in this simulation. First of all, it is a 2D simulation. Important dimensional effects are not being included, which has been shown to affect the results (Chapter 3). These simulations also do not include the effects of pores, which inhibit grain growth [1, 125](Chapter 2). Therefore, it

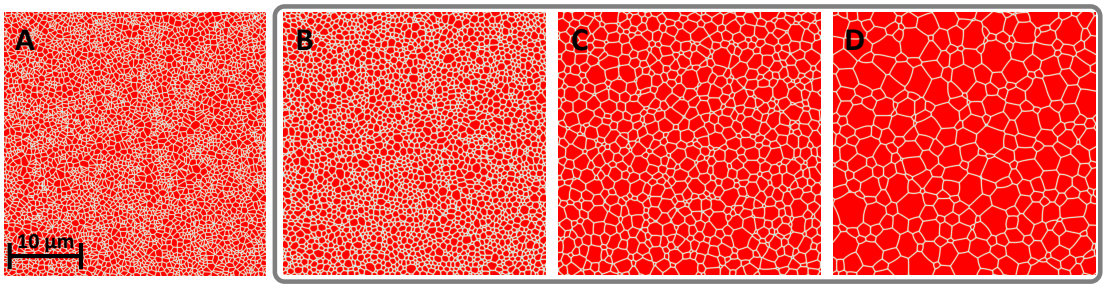

Figure 4.6. Simulated microstructure comparison from the 2D grain growth simulations at 1900 K. A: The initial condition used for all three simulations. The final grain structure after 530 seconds for the undoped case (B), Cr-doped case (C), and Mn-doped case (D).

is better to simulate sintering in 3D with pores present to eliminate this assumption. We do this in the following section.

4.6 Dopant Effects on Sintering

We have now examined the effects of Cr and Mn dopants on pore closure and grain growth. In the case of pore closure, we found that the relative difference between Cr-doped and undoped UO_2 are consistent with experiments and Mn appears to increase the densification rate even further. In the case of grain growth, the acceleration due to the Cr dopants is once again consistent with experiments and Mn accelerates the growth even further. However, both of those simulations are limited. The pore closure simulation used very few particles, maintained constant temperature, and had only a single pore. The grain growth simulation was 2D and did not include pores. To improve upon both of these results, a 3D sintering simulation using a non-constant temperature and a relatively large number of particles and pores is used to investigate the impact of the dopants.

4.6.1 Simulation Setup

The purpose of these simulations is a direct comparison of the relative effects of dopants on sintering. We do this by heating a powder compact from 973 K to 1973 K over 12,000 s (200 min) and measuring the density and grain size. The heating ramp also serves to improve the interface profile like in the grain growth simulations above. However, it should be noted that in experiments, the bulk density is measured during heating, but the average grain size is measured during constant temperature annealing [36, 180]. The interface thickness is set to $\ell = 200$ nm. The initial condition is generated in the same manner as Chapter 3 except that a uniform size distribution is used. 100 particles, each with a diameter of 700 nm, are allowed to fall randomly into a box-shaped space without

being allowed to overlap. The domain is 4.1 μm by 4.1 μm by 4.3 μm in the z-direction. Mesh adaptivity is used with elements ranging in size from 48.8 nm to 195.2 nm.

These sintering conditions are simulated for undoped, Cr-doped, and Mn-doped UO_2. However, since the dopants do not begin to impact the equilibrium vacancy concentration until they reach elevated temperature, as shown in Fig. 4.1, the behavior of the three simulations are identical until they reach these dopant transition temperatures (1803 K for Cr-doped and 1776 K for Mn-doped). Therefore, to reduce computational expense, only the undoped case was run at the lower temperatures. Then, once the dopant transition temperature was reached, the undoped simulation results were used as the initial condition for the two doped cases.

Two measurements are taken: the density, measured using the Monte Carlo integration technique from Chapter 3, and the grain size, measured using the GrainTracker algorithm built into MARMOT [149]. Both of these measurements are somewhat noisy. The Monte Carlo integration technique has noise from its stochastic nature as well as sudden jumps when a particle/grain on the outer edge is consumed by a neighboring grain. The GrainTracker algorithm relies on a threshold value to find and count grains. While a grain is being eliminated, its max value can hover near the threshold, causing the number of grains counted by GrainTracker to fluctuate.

4.6.2 Simulation Results

The microstructure evolutions of the three cases are shown in Fig. 4.7. The first two rows show the evolution of the low temperature region and the undoped case. The third and fourth rows show the evolution of the Cr-doped case and Mn-doped cases, respectively, at times that match the second row. One quarter of the microstructure has been removed in the images so that the interior microstructure can be seen. The density measurements are shown in Fig. 4.8, with the three cases distinguished by color. The average grain size is shown in Fig. 4.9, with similar coloration.

Fig. 4.7 shows how grain growth is accelerated by the dopants. The undoped case at 12,000 seconds looks very similar to the Cr-doped case at 11,000 seconds. However, Fig. 4.9 shows that the Cr-doped case in fact has larger grains by that time. Meanwhile, the Cr-doped case at 12,000 seconds looks very similar to the Mn-doped case at 11,000 seconds.

Both in terms of density and grain size, all three cases reach the maximum possible value before the end of the simulation. This limits the region of the simulation where useful comparisons can be made between the cases and suggests that additional particles should be used in future simulations.

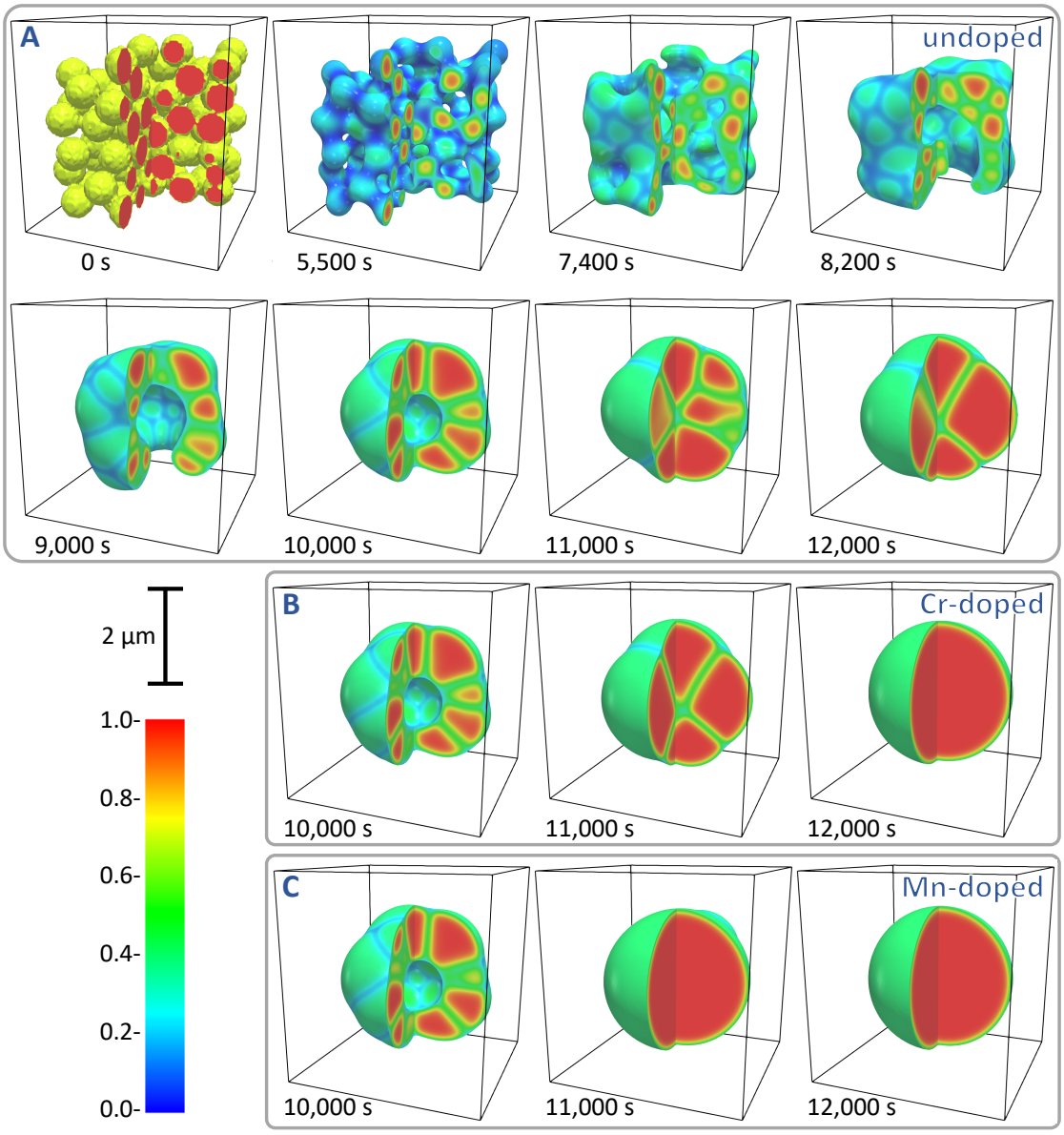

Figure 4.7. Microstructure evolution of the 100-particle sintering simulations. In each image the region where $\phi \leq 0.3$ is shown with one quarter of the domain removed to show the interior. Boxes show the outline of the entire domain. The images are colored based on Eq. (4.20). A: The undoped case. Dopants do not affect behavior at low temperature, so the initial heating is identical for all three cases. B: The Cr-doped case during the last quarter of the simulation. C: The Mn-doped case during the last quarter of the simulation. The Cr- and Mn-doped cases do not diverge from the undoped case until 9,948 s and 9,583.2 s, respectively.

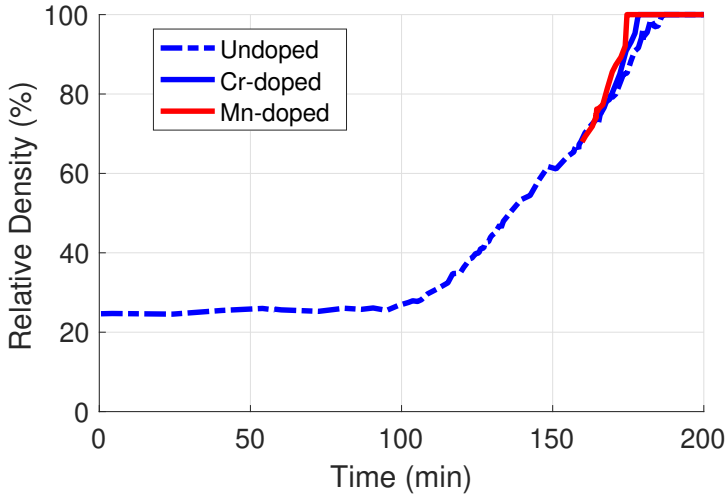

Figure 4.8. Relative density for the 100-particle sintering simulations. The simulations are split into regions based on the dopant according to Eqs. (4.3), (4.4), and (4.5). At the times they reach maximin density, the Cr-doped case and the Mn-doped case are 0.74% and 1.32% more dense than the undoped case, respectively.

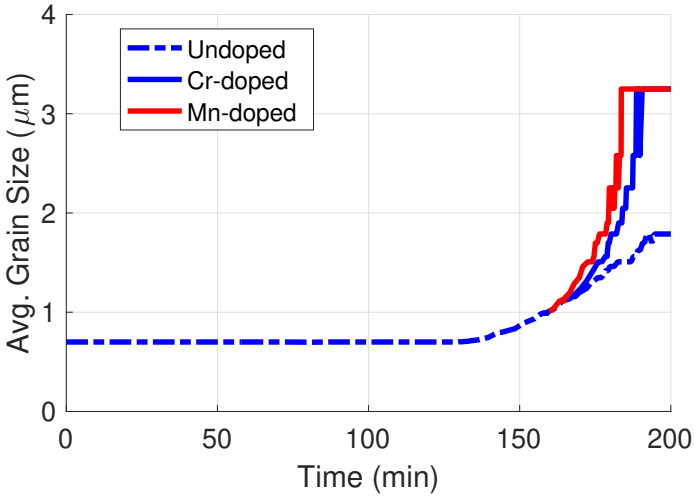

Figure 4.9. Average grain size for the 100-particle sintering simulations. The simulations are split into regions based on the dopant accourding to Eqs. (4.3), (4.4), and (4.5). At the times they reach maximum grain size, the Cr- and Mn-doped average grain sizes are 2.31 and 2.33 times larger than the undoped grains.

4.6.3 Discussion

While most of the microstructure evolution occurs prior to the dopants taking effect, the dopants have a measurable effect in both density and grain size. Quantifying these effects is somewhat difficult because they are limited by reaching both maximum density and

maximum grain size. However, measurable differences do exist in the three cases. At the time they reach maximum density, the Cr- and Mn-doped cases are 0.74% and 1.32% more dense than the undoped case, respectively. This result is similar to the expected results from experiments and consistent with the results from Sec. 4.4. When they reach the maximum grain size, the Cr- and Mn-doped cases are 2.31 and 2.33 times larger than the undoped case. This is somewhat lower than the rates found in experiments and Sec. 4.5, but similar to the values predicted by ideal grain growth models informed by atomistic simulations [191].

There are several important differences between the simulations in Sec. 4.5 and this section that must be explored to determine the reason for the change in relative grain sizes. The previous simulations were 2D with more grains, no pores, and constant temperature. This set of simulations is in 3D, has fewer grains, includes pores, and occurs in a temperature ramp. Let us examine each of these differences. We have shown previously that 2D and 3D geometries can give different results using this model (Chapter 3). However, the effect was to reduce the sintering rate in 2D and was relatively linear. This would not be expected to reduce the relative effect of dopants in 3D.

It would be reasonable to assume that the relatively small number of grains in the 3D simulation reduced the accuracy. Had the grains been able to continue to grow, the average grain size ratio may have continued to increase. To test this hypothesis, we recreate the simulation from Sec. 4.5 with 100 grains on a (5,550 nm)^2 domain. The simulations were allowed to continue until they reduced to a single grain. The resulting fit functions, however, were unchanged from those listed in Table 4.4. We can therefore conclude that the difference is not caused by the number of grains in the simulation.

It is known that pores inhibit grain growth [1,125](Chapter 2). However, the presence of pores does not appear to be a major factor in the grain size discrepancy for the simple reason that the final pore disappears from the microstructure before the majority of grain growth occurs (see Figs. 4.8 and 4.9).

This leaves the different temperature profiles. Temperature is one of the largest driving forces of sintering [1](Chapter 2). To look at the effect of temperature profile, we measured the average grain sizes from Sec. 4.5 prior to reaching the maximum temperature at 400 s. The results are shown in Fig. 4.10. Rather than the square root-curve in Fig. 4.5, this region shows exponential behavior that will diverge as heating continues. The temperature profile appears to be the most likely reason for the different behavior of the relative grain size measurements in this section and Sec. 4.5.

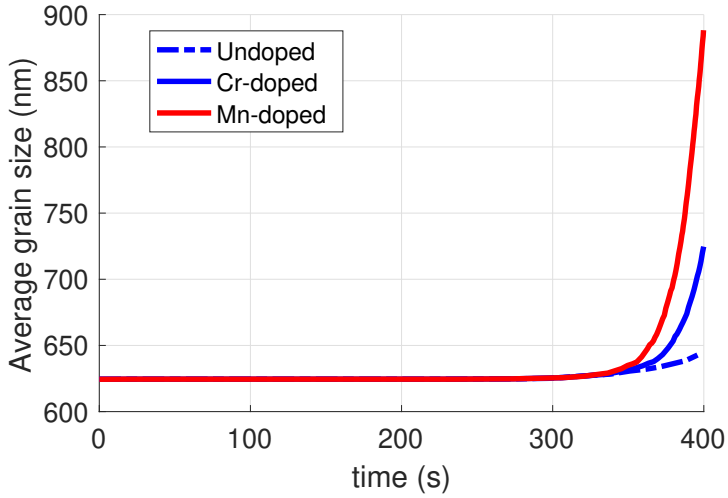

Figure 4.10. Average grain size during the heating ramp prior to Fig. 4.5 for undoped, Cr-doped, and Mn-doped cases. The behavior profile is exponential so that it appears the relative grain sizes will diverge as heating continues.

4.7 Conclusion

In this chapter we have added the impact of dopants into the grand potential sintering model by changing the vacancy equilibrium concentration in the manner predicted by the proposed charged-defect mechanism [191]. We then compared the predictions of model to experimental data on Cr-doped UO_2. The grand potential model predicts relative behavior very similar to that recorded in the literature [36, 180, 191]. Both small- and medium-scale sintering simulations predicted a Cr-doped to undoped density ratio that is consistent with experiments. 2D large-scale grain growth simulations additionally predicted a relative grain size difference which was consistent with experiments. However, a 3D medium-scale sintering simulation found a grain size difference which was smaller than experiments. It appears this discrepancy is caused by the temperature profile used in the simulation, which matched the temperature profile used in experiments to measure the density change, but not the profile used when measuring the average grain size. Experimental measurements of the average grain size were made after constant-temperature annealing, while the simulated grain growth measurements were made during heating. These results support the proposed charged-interstitial mechanism as a valid theory of dopant behavior. Additionally, we tested the predictions of Mn as a dopant and found that it does indeed act as a stronger dopant than Cr. Thus, Mn-doped UO_2 appears to be a new ATF concept for near-term deployment that could yield larger grains and denser pellets than undoped or Cr-doped UO_2 fuel.

The next step is to run sintering experiments on undoped, Cr-doped, and Mn-doped UO_2 to see if our predictions hold true. If the predictions do hold, then that will validate the charged-interstitial mechanism as an accurate model of dopant behavior in UO_2. It will also begin development of a new Mn-doped ATF concept.

Chapter 5
Grand Potential Simulations of Irradiation-Enhanced Densification

5.1 Introduction

Irradiation-enhanced densification (IED) is a phenomenon that occurs in sintered nuclear fuels—typically UO_2. Early in the fuel lifetime the volume of the fuel decreases, which increases the distance between the fuel and the cladding, or plenum gap width. The plenum gap has poor thermal conductivity. So increasing the gap width increases the centerline temperature of the fuel [1](Chapter 2). IED must be understood and quantified in order to maintain fuel temperature and safety standards in existing fuels as well as accident-tolerant and next-generation fuel concepts. In the present work, we apply recent advances in computational sintering models to create a microstructural IED model and verify that the model is working through the use of test cases designed to isolate specific mechanisms or physical effects. These test cases provide additional insight into how increased point defect densities and collision cascade mixing effects contribute to the rate of pore shrinkage in IED.

A porous material in a high temperature environment will sinter and become more dense [6]. UO_2 fuel pellets are manufactured via sintering; and as a result have a non-negligible level of porosity. Upon powering the reactor, the pellets sinter and increase in density. Initially, it was believed that that densification occurred at the same rate in the reactor as it did during sintering [130]. However, it was later found that the fuel volume decreased faster in reactors than they did in experiments with similar temperatures but no fission [9]. Thus, IED is is accelerated by fission within the fuel [1, 10](Chapter 2).

The energy released by fission is carried primarily by the fission fragments as kinetic energy. The fragments collide with atoms in the fuel's crystal lattice, distributing the energy into the lattice and briefly liquefying a small portion of the crystal in events called "collision cascades" [1](Chapter 2). Within a few picoseconds the energy dissipates enough for the atoms to recrystallize [133].

Modern IED theory identifies three driving mechanisms that increase the sintering rate [1](Chapter 2):

- Collision cascade mixing—Within the liquefied portion of the crystal, the atoms diffuse at accelerated rates. The bulk effect of this is accelerated diffusion of the point defects throughout the crystal lattice.
- Increased point defect density—Once the cascade cools and recrystallizes, some U atoms do not reach lattice sites, and instead become interstitial point defects. This leaves a nearby vacancy, thus generating a pair of point defects known as a Frenkel pair. Increased point defect densities increase the self-diffusion rate of U atoms in the material, which increases the sintering rate.
- Pore damage—If a collision cascade occurs on the edge of a pore, atoms from the lattice can be dispersed into the pore, partially filling in the pore while increasing the number of vacancies in the lattice [132]. This causes the overall volume of the pore to decrease and the point defect density in the lattice to increase.

The primary bulk effect of IED is to increase the evacuation rate of small pores [10, 130] (less than 1 μm in diameter [132]). The accepted reason for this size dependence is that large pores act as stronger sinks, which allows them to reabsorb vacancies expelled by pore damage [1](Chapter 2).

The overall difference in the rate of density change between IED and sintering depends on the pore size distribution, the temperature (it is primarily observed at temperatures below 1,300 °C [1, 130]), and the grain size distribution (IED has a larger effect in small-grain structures [10]). However, there are still several important questions that remain unanswered about the IED mechanics. First, do the three driving mechanisms contribute to densification equally, or does one dominate the others? Experimental studies have been unable to address this question because the mechanisms cannot be separated experimentally. Second, both intragranular and grain boundary (GB) pores exist in sintered UO_2. Does the location of the pore affect its IED behavior? Third, how do grain boundaries interact with collision cascades such that small-grain structures densify faster? This question was considered by Bai et al. [133], who found that GBs facilitate vacancy and interstitial recombination. However, this would suggest that grain

boundaries slow down densification by suppressing the defect density, which contradicts the findings of Freshley et al. [10].

Recent studies have proposed using dopants to increase the UO_2 density and average grain size to improve fuel performance [191](Chapter 4). The modified microstructures in doped fuels could impact IED behavior, though the dopants themselves are unlikely to affect the densification at reactor operating temperatures [191](Chapter 4). However, existing empirical models are not equipped to accurately predict the IED behavior of such fuels because no densification data is available from doped fuels [1](Chapter 2). A mechanistic microstructural model could predict the IED behavior in the doped fuels with a greater level of fidelity than empirical models [1](Chapter 2).

In this work we use recent advances in microstructural sintering models (Chapters 3 and 4) to build an IED model and examine some of the effects of collision cascades on the pore evacuation rate as well as effects of the microstructure on the IED rate in UO_2. A recent review paper found no microstructural IED models in current use [1](Chapter 2), so this model fills a gap in computational capabilities related to IED. We have previously used the grand potential sintering model to simulate sintering of UO_2 (Chapter 3) and to validate a proposed mechanism for doped sintering (Chapter 4). In sintering, the density of U-interstitials is so low that they can be ignored. But due to Frenkel pair generation, interstitials should be included in the IED model. To account for this we derive the model with both vacancy and interstitial terms along with terms to account for the generation and annihilation of point defects. An additional term is also added to represent increased self-diffusion from collision cascade mixing. Direct pore damage is not currently included in the model.

5.2 Derivation of Grand Potential Model

This grand potential formulation is based on the quantitative and flexible multi-phase grand potential model derived by Aagesen et al. [151]. It is based on the works of Moelans [147, 155] and Plapp [150]. It is applied to UO_2 sintering in Chapters 3 and 4. Some modifications need to be made to apply the model to IED. As is commonly done in phase field models, we assume that all GB properties are isotropic.

5.2.1 Equations governing the matrix and bubble phases

There are n order parameters, $\vec{\eta} = \{\eta_1, \eta_2, ..., \eta_n\}$, which represent individual grains in the matrix phase. There is one order parameter, ϕ, which represents the bubble phase. The bubble phase includes the void—the space on the exterior of the fuel pellet—and

the pores—empty spaces inside the fuel pellet which are completely isolated from the void and contribute to the fuel porosity. These order parameters are governed by the Allen-Cahn equation [116]:

$$\begin{aligned}\frac{\partial \eta_i}{\partial t} &= -L_m \frac{\delta \Omega}{\delta \eta_i} \\ \frac{\partial \phi}{\partial t} &= -L_b \frac{\delta \Omega}{\delta \phi}\end{aligned} \tag{5.1}$$

where L_m and L_b are the matrix and bubble phase Allen-Cahn mobilities, respectively, and Ω is the grand potential functional:

$$\Omega = \int_V \left[\epsilon f_B + \kappa f_{grad} + h_m \omega_m + (1 - h_m)\omega_b\right] dV, \tag{5.2}$$

where f_B is the bulk free energy, f_{grad} is the gradient free energy, ϵ and κ are energy coefficients, h_m is a switching function that transitions between 1 in the matrix phase and 0 in the bubble phase, and ω_m and ω_b are grand potential densities for the two phases. The bulk free energy has the form:

$$f_B = \left(\frac{\phi^4}{4} - \frac{\phi^2}{2}\right) + \sum_{i=1}^{n}\left(\frac{\eta_i^4}{4} - \frac{\eta_i^2}{2}\right) + \frac{3}{2}\left(\phi^2 \sum_{i=1}^{n} \eta_i^2 + \sum_{i=1}^{n}\sum_{j>i}^{n} \eta_i^2 \eta_j^2\right) + \frac{1}{4}. \tag{5.3}$$

This function ensures that having exactly one order parameter equal to 1 while the others are equal to 0 is energetically preferred. The gradient energy has the form:

$$f_{grad} = \frac{1}{2}\left((\nabla \phi)^2 + \sum_{i=1}^{n} (\nabla \eta_i)^2\right). \tag{5.4}$$

This formulation applies an energy penalty if the order parameter gradients are too high, which ensures a diffuse interface. The grand potential densities depend on the point defects and will be explained in Sec. 5.2.2.

5.2.2 Equations governing the vacancy and interstitial point defect densities

The diffusivity of U atoms is much lower than the diffusivity for O atoms, making U the rate-limiting species (Chapter 3). Therefore, the model only considers the U atoms. There are two conserved U point defect atomic densities for the vacancy and interstitial species, represented by the variables ρ_v and ρ_i, respectively. These are governed by the equation

$$\frac{\partial \rho_\nu}{\partial t} = \dot{\rho}_{\nu,diff} + \dot{\rho}_{gen} - \dot{\rho}_{ann} + \dot{\rho}_{\nu,mix}, \tag{5.5}$$

where $\nu = \{i, v\}$, $\dot{\rho}_{\nu,diff}$ is the change in atomic density from defect self-diffusion, $\dot{\rho}_{gen}$ is the change in atomic density from defect generation, $\dot{\rho}_{ann}$ is the change from defect annihilation, and $\dot{\rho}_{\nu,mix}$ is the change from collision cascade mixing. The time-derivative term can be expanded by the chain rule to

$$\frac{\partial \rho_\nu}{\partial t} = \frac{\partial \rho_\nu}{\partial \mu_\nu}\frac{\partial \mu_\nu}{\partial t} + \frac{\partial \rho_\nu}{\partial \phi}\frac{\partial \phi}{\partial t} + \sum_{i=1}^{n}\frac{\partial \rho_\nu}{\partial \eta_i}\frac{\partial \eta_i}{\partial t}, \tag{5.6}$$

where μ_ν is the chemical potential of species ν. $\dot{\rho}_{\nu,diff}$ is calculated based on the conserved diffusion equation

$$\begin{aligned}
\dot{\rho}_{\nu,diff} &= -\nabla \cdot \vec{j}_\nu, \\
&= \nabla \cdot \mathbf{D}_\nu \nabla \rho_\nu, \\
&= \nabla \cdot \mathbf{D}_\nu \frac{\partial \rho_\nu}{\partial \mu_\nu} \nabla \mu_\nu,
\end{aligned} \tag{5.7}$$

where $\vec{j}_\nu$ and $\mathbf{D}_\nu$ are the flux and the diffusion tensor for species ν, respectively.

The defect generation term depends on the fission rate, $\dot{f}$, according to

$$\dot{\rho}_{gen} = \dot{f}\xi N_c N_d h_m, \tag{5.8}$$

where N_c is the number of collision cascades per fission, N_d is the number of Frenkel pairs generated per cascade, h_m is a switching function that determines the matrix phase, and ξ is a random noise term that accounts for the random positions of collision cascades. Defect annihilation occurs when a vacancy and interstitial recombine. Therefore, the annihilation term represents recombination [199]:

$$\begin{aligned}
\dot{\rho}_{ann} &= a_r \rho_i \rho_v, \\
a_r &= \frac{h_m V_a Z |\mathbf{D}_i|}{a_0^2},
\end{aligned} \tag{5.9}$$

where a_r is the recombination rate, V_a is the defect atomic volume, Z is the recombination number, a_0 is the atomic jump distance, and $|\mathbf{D}_i|$ is the scalar magnitude of $\mathbf{D}_i$.

Collision cascade mixing occurs as the lattice atoms within the collision cascade mix at a highly-accelerated rate [1](Chapter 2). The bulk effect of this can be approximated

by athermal diffusion [142]. This is demonstrated in Fig. 5.1. A 1D Monte Carlo (MC) simulation is used to approximate collision cascade mixing in a system with no other evolution effects. Collision cascades are approximated as regions of a set size where the defect density is instantly homogenized. At each MC step, a point is randomly chosen for a collision cascade. The accumulation of collision cascades drives the evolution of the defect density. This is overlayed with a nondimensionalized diffusion simulation. The two simulations show very similar defect profile evolutions.

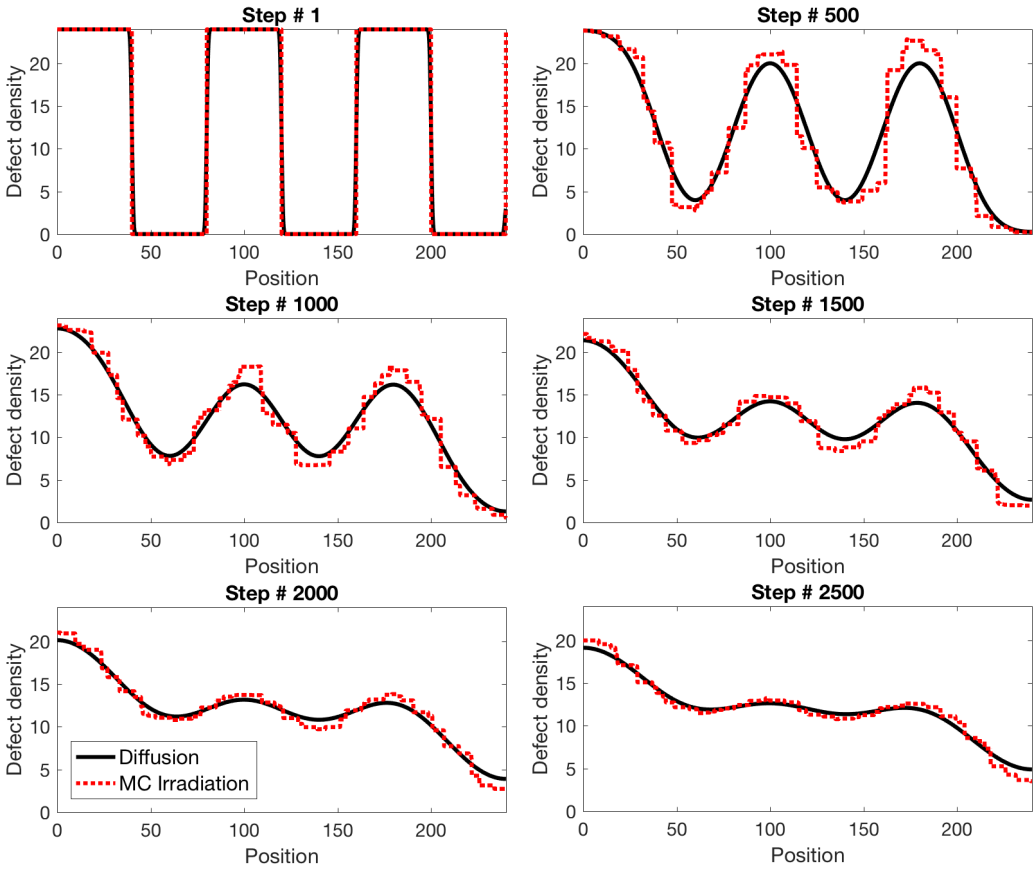

Figure 5.1. 1D nondimensionalized demonstration of an athermal diffusion approximation for collision cascade mixing. The red dashed line uses a Monte Carlo approximation of collision cascade mixing. At each time step, a location for a cascade is randomly chosen and the defect density within the cascade region is set to the average defect density within the region. The black line begins with the same initial condition, but evolves by solving the diffusion equation. Throughout the simulation the two lines match very well.

Using an athermal diffusion approximation, the collision cascade mixing term becomes

$$\dot{\rho}_{\nu,mix} = \nabla \cdot D_{mix} \nabla \rho_{\nu},$$

$$= \nabla \cdot \frac{\partial \rho_\nu}{\partial \mu_\nu} D_{mix} \nabla \mu_\nu, \tag{5.10}$$

where D_{mix} is the athermal diffusion coefficient of collision cascade mixing.

We now introduce the susceptibility of species ν, χ_ν:

$$\chi_\nu = \frac{\partial \rho_\nu}{\partial \mu_\nu} \tag{5.11}$$

Combining Eqs. (5.5)–(5.11) yields the chemical potential evolution equation:

$$\chi_\nu \frac{\partial \mu_\nu}{\partial t} = \nabla \cdot \chi_\nu \left(\mathbf{D}_\nu + D_{mix} \right) \nabla \mu_\nu + h_m \left(\dot{f} \xi N_c N_d - \frac{V_a Z |\mathbf{D}_i|}{a_0^2} \rho_i \rho_v \right) - \frac{\partial \rho_\nu}{\partial \phi} \frac{\partial \phi}{\partial t} - \sum_{i=1}^{n} \frac{\partial \rho_\nu}{\partial \eta_i} \frac{\partial \eta_i}{\partial t}. \tag{5.12}$$

Eq. (5.12) is the governing equation for the chemical potential variables.

The phase-independent chemical potential is a function of the atomic defect density

$$\mu_\nu = \frac{\partial f_{\nu,m}}{\partial \rho_{\nu,m}} = \frac{\partial f_{\nu,b}}{\partial \rho_{\nu,b}}, \tag{5.13}$$

where $f_{\nu,\alpha}$ is the free energy of species ν in phase $\alpha = \{m, b\}$ and $\rho_{\nu,\alpha}$ is the atomic density of species ν in phase α. The free energies for each species and phase are estimated as parabolic curves:

$$f_{\nu,\alpha} = \frac{1}{2} k_{\nu,\alpha} \left(\rho_\nu - \rho^*_{\nu,\alpha} \right)^2, \tag{5.14}$$

where $k_{\nu,\alpha}$ is a parabolic coefficient and $\rho^*_{\nu,\alpha}$ is the equilibrium atomic density of species ν in phase α. The density can now be converted to a function of chemical potential by using Eq. (5.14) to invert Eq. (5.13):

$$\begin{aligned} \rho_{\nu,\alpha} &= \frac{\mu_\nu}{V_a^2 k_{\nu,\alpha}} + \rho^*_{\nu,\alpha}, \\ \rho_\nu &= h_m \rho_{\nu,m} + (1 - h_m) \rho_{\nu,b}. \end{aligned} \tag{5.15}$$

The susceptibility from Eq. (5.11) now becomes:

$$\chi_\nu = \frac{1}{V_a^2} \left(\frac{h_m}{k_{\nu,m}} + \frac{1 - h_m}{k_{\nu,b}} \right). \tag{5.16}$$

Now it is possible to define the grand potential densities from Eq. (5.2) using Eq. (5.14):

$$\begin{aligned}\omega_\alpha &= f_{v,\alpha} - \rho_{v,\alpha}\mu_v + f_{i,\alpha} - \rho_{i,\alpha}\mu_i \\ &= -\frac{1}{2}\frac{\mu_v^2}{V_a^2 k_{v,\alpha}} - \mu_v\rho_{v,\alpha}^* - \frac{1}{2}\frac{\mu_i^2}{V_a^2 k_{i,\alpha}} - \mu_i\rho_{i,\alpha}^*\end{aligned} \tag{5.17}$$

This formulation defines the effects of increased point defect density by including the generation and annihilation terms $\dot{\rho}_{gen}$ and $\dot{\rho}_{ann}$. It also defines collision cascade mixing via the term $\dot{\rho}_{\nu,mix}$. Since it is based on an established sintering model (Chapter 3) and includes two of the IED mechanisms, this model should capture IED behavior. However, this formulation does not capture direct pore damage.

5.2.3 Definitions of Quantitative Terms

We calculate the Allen-Cahn mobilities from Eq. (5.1) according to (Chapter 3):

$$\begin{aligned}L_m &= \frac{4}{3}\frac{M_{GB}}{\ell}, \\ L_b &= 40L_m,\end{aligned} \tag{5.18}$$

where ℓ is the interface width and M_{GB} is the GB mobility. M_{GB} is calculated according to the Arrhenius equation:

$$M_{GB} = M_0 \exp\left(\frac{-Q}{k_B T}\right), \tag{5.19}$$

where M_0 is the mobility prefactor, Q is the GB mobility activation energy, k_B is Boltzmann's constant, and T is the absolute temperature.

The energy coefficients, ϵ and κ, from Eq. (5.2) are functions of the interface energies for surfaces and GBs, σ_S and σ_{GB}, respectively, as well as the interface width:

$$\begin{aligned}\epsilon &= h_S\epsilon_S + (1-h_S)\epsilon_{GB}, \\ \kappa &= h_S\kappa_S + (1-h_S)\kappa_{GB}, \\ \epsilon_\beta &= \frac{6\sigma_\beta}{\ell}, \\ \kappa_\beta &= \frac{3\sigma_\beta\ell}{4},\end{aligned} \tag{5.20}$$

where h_S is a switching function that distinguishes surface regions from GBs, β represents the interface according to $\beta = \{S, GB\}$, and ϵ_β and κ_β are the constant interface values.

The switching functions h_m and h_S both take the same form:

$$H(\phi,\phi_0)=\begin{cases}0, & \phi\leq 0\\ 6\left(\frac{\phi}{\phi_0}\right)^5-15\left(\frac{\phi}{\phi_0}\right)^4+10\left(\frac{\phi}{\phi_0}\right)^3, & 0<\phi<\phi_0\\ 1, & \phi\geq\phi_0\end{cases},$$
$$h_m=1-H(\phi,1),$$
$$h_S=H(\phi,0.3). \tag{5.21}$$

The parameter ϕ_0 is set to a value between 0 and 1. Lower values increase the accuracy of the energy profiles and the computational expense of the simulations. A value of 0.3 keeps the error below 5% (Chapter 3).

The diffusion tensors take the form proposed by Ahmed et al. [148]:

$$\mathbf{D}_\nu=D_{B,\nu}\mathbf{I}+D_{GB,\nu}\sum_{i=1}^{n}\sum_{j\neq i}^{n}\eta_i\eta_j\mathbf{T}_{GB}^{i,j}+D_{S,\nu}\phi^2(1-\phi)^2\mathbf{T}_S,$$
$$\mathbf{T}_{GB}^{i,j}=\mathbf{I}-\frac{\nabla\eta_i-\nabla\eta_j}{|\nabla\eta_i-\nabla\eta_j|}\otimes\frac{\nabla\eta_i-\nabla\eta_j}{|\nabla\eta_i-\nabla\eta_j|},$$
$$\mathbf{T}_S=\mathbf{I}-\frac{\nabla\phi}{|\nabla\phi|}\otimes\frac{\nabla\phi}{|\nabla\phi|}, \tag{5.22}$$

where $D_{B,\nu}$, $D_{GB,\nu}$, and $D_{S,\nu}$ are the bulk, GB, and surface diffusion magnitudes for species ν. $\mathbf{I}$ is the identity tensor, while $\mathbf{T}_{GB}^{i,j}$ and $\mathbf{T}_S$ are normalized directional tensors of the GB and surface interfaces, respectively. The diffusion magnitudes are estimated according to

$$D_{B,\nu}=D_{0,\nu}\exp\left(\frac{-E_\nu^B}{k_BT}\right),$$
$$D_{GB,\nu}=w_{GB}D_{B,\nu},$$
$$D_{S,\nu}=w_SD_{B,\nu}, \tag{5.23}$$

where $D_{0,\nu}$ and E_ν^B are the Arrhenius prefactor and migration energy for species ν in the bulk, and w_{GB} and w_S are multiplier weights for GBs and surfaces, respectively (Chapter 3).

The computational expense of this model is lowered by replacing the tensor $\mathbf{D}_i$ with its magnitude $|\mathbf{D}_i|$, as shown in Eq. (5.9). Since an interstitial will tend to approach a vacancy in the direction of fastest diffusion, the interstitial diffusion directional component can be neglected.

We estimate the athermal diffusion coefficient for collision cascade mixing as

$$D_{mix} = \dot{f}\xi N_c t_c V_c D_c, \tag{5.24}$$

where t_c is the length of time of a collision cascade, V_c is the volume of a collision cascade, and D_c is the diffusion coefficient within a collision cascade.

The treatment of vacancies in the bulk requires some additional explanation. Some models treat GBs and surfaces as point defect sinks where the point defects are annihilated. Our model uses accelerated diffusion along GBs to transport the point defects away from the bulk to the external surface (Chapter 3). This requires a higher defect density on GBs than in the bulk. Therefore, the equilibrium matrix phase point defect density from Eq. (5.14) is defined as

$$\rho^*_{\nu,m} = \rho^B_{\nu,m} + 4(\rho^{GB}_{\nu,m} - \rho^B_{\nu,m})(1-\lambda)^2, \tag{5.25}$$

$$\lambda = \sum_{i=1}^{n} \eta_i^2, \tag{5.26}$$

where $\rho^B_{\nu,m}$ is the atomic equilibrium density for species ν in grain interiors and $\rho^{GB}_{\nu,m}$ is the atomic equilibrium density on grain boundaries.

5.2.4 Assignment of Parameter Values

First we assign the material-specific parameters. These are listed in Table 5.1 along with references where applicable. The matrix phase parabolic coefficients, $k_{\nu,m}$ are chosen by setting the second derivative of the phase energy $\partial^2 f_{\nu,m}/\partial\rho^2_{\nu,m}$ equal to the ideal solution's model [150] second derivative at $\rho_{\nu,m} = \rho^*_{\nu,m}$. This way, small deviations from the equilibrium values result in accurate energy, while ensuring that rounding errors are easily manageable by the computer code. The bubble phase coefficient values are assumed to be equal to the matrix phase parabolic coefficients.

The athermal diffusion coefficient, D_c, is chosen such that in a simulation of the volume of a collision cascade, V_c, the defects could diffuse to near-equilibrium within the time of a collision cascade, t_c.

There are a few other parameters which must be assigned or assumed. First, the temperature is chosen to be 1200 K for all simulations. The interface width is likewise assigned to be 20 nm except for one simulation which will be specified. The fission rate is set to 10^{-8} nm^{-3}s^{-1} and ξ is a uniform random noise function which varies between 0.5 and 1.5.

Name	Value	Units	Ref.
a_0	0.25	nm	[199]
D_c	10^{12}	nm^2s^{-1}	–
$D_{0,i}$	10^{13}	nm^2s^{-1}	[156]
$D_{0,v}$	8.33×10^9	nm^2s^{-1}	Chapter 3
E_i^B	2	eV	[156]
E_v^B	3.608	eV	Chapter 3
$k_{i,b}$	3.6×10^{21}	eV nm^{-3}	–
$k_{i,m}$	3.6×10^{21}	eV nm^{-3}	–
$k_{v,b}$	26.8	eV nm^{-3}	–
$k_{v,m}$	26.8	eV nm^{-3}	–
N_c	2	–	–
N_d	5	–	[133]
Q	2.77	eV	[160]
t_c	10^{-11}	s	[133]
V_a	0.04092	nm^3	[159]
V_c	268	nm^3	[133]
w_{GB}	10^6	–	Chapter 3
w_S	10^9	–	Chapter 3
Z	250	–	[199]
$\rho^*_{i,b}$	0	nm^{-3}	–
$\rho^B_{i,m}$	2.566×10^{-28}	nm^{-3}	[171]
$\rho^{GB}_{i,m}$	2.282×10^{-3}	nm^{-3}	[171] Chapter 4
$\rho^*_{v,b}$	24.438	nm^{-3}	Chapter 4
$\rho^B_{v,m}$	0.02282	nm^{-3}	Chapter 4
$\rho^{GB}_{v,m}$	2.444	nm^{-3}	Chapter 4
σ_{GB}	19.7	eV/nm^2	[157]
σ_S	9.86	eV/nm^2	[158]

Table 5.1. Constant parameters used in the IED model to represent in-reactor UO_2 with units and references.

5.3 Model Verification

We begin with a set of 1D simulations to show that the model is working correctly. We want to examine the steady state behavior of vacancy and interstitial point defects. Adding defect generation should increase the point defect densities, and adding the defect annihilation term should allow them to reach a semi-steady state (true steady state is not likely because of the noise term, ξ). Adding the collision cascade mixing should cause additional diffusion among the point defects and decrease the overall density by increasing the recombination rate.

The simulations use a 1 μm 1D domain with 500 elements. One grain takes up the right half of the domain while a void takes up the left half. The simulations run until the

interface is stable. Except where otherwise specified the simulations use the parameters given in Sec. 5.2.3 except for the interface width, which is increased to 100 nm to give a highly accurate interface profile.

The first simulation is a baseline sintering simulation with a fission rate of 0. The second simulation uses the sintering rate from Sec. 5.2.3. The third simulation increases the fission rate by a factor of 100 to exaggerate the effects of IED. The fourth and fifth simulations use the increased fission rate. The fourth simulation removes the defect generation and annihilation terms to isolate the effects of collision cascade mixing, and the fifth simulation removes the athermal diffusion term to isolate the effects of defect generation.

The results of this study are shown in Fig. 5.2. Order parameter profiles are shown along with the vacancy and interstitial point defect densities. The first simulation is shown in blue in all graphs for comparison to the effects of IED.

Adding defect generation and annihilation increases the defect density; which most easily seen in the behavior of ρ_i. Adding collision cascade mixing not only decreases the maximum point defect density, but also causes the chemical potentials to become more diffuse. The effect of this is actually to slightly narrow the order parameter interfaces as they adjust to match the profile of the switching function h_m (see Eq. (5.15)). Collision cascade mixing has the larger effect on vacancies, but point defect generation has more of an effect on interstitials.

These results show that the model is behaving as expected and that our IED terms are able to affect the microstructure at steady state. Next we need to run simulations testing the kinetic effects of IED on pore evacuation.

5.4 IED Simulations

5.4.1 Relative strengths of defect density and collision cascade mixing mechanisms

This set of simulations is designed to examine the individual effects of point defect generation and collision cascade mixing on the pore evacuation rate. The domain is shown in Fig. 5.3 and consists of a 2D rectangle with a circular pore 100 nm in diameter separated from an external void. The domain is 450 nm by 100 nm with 90×20 elements. Only half of the pore is defined to make use of the plane of symmetry. The external void takes up the last 200 nm of the domain, and the center of the pore is 150 nm away from the surface interface.

Four simulations are used. First is a baseline sintering simulation without radiation

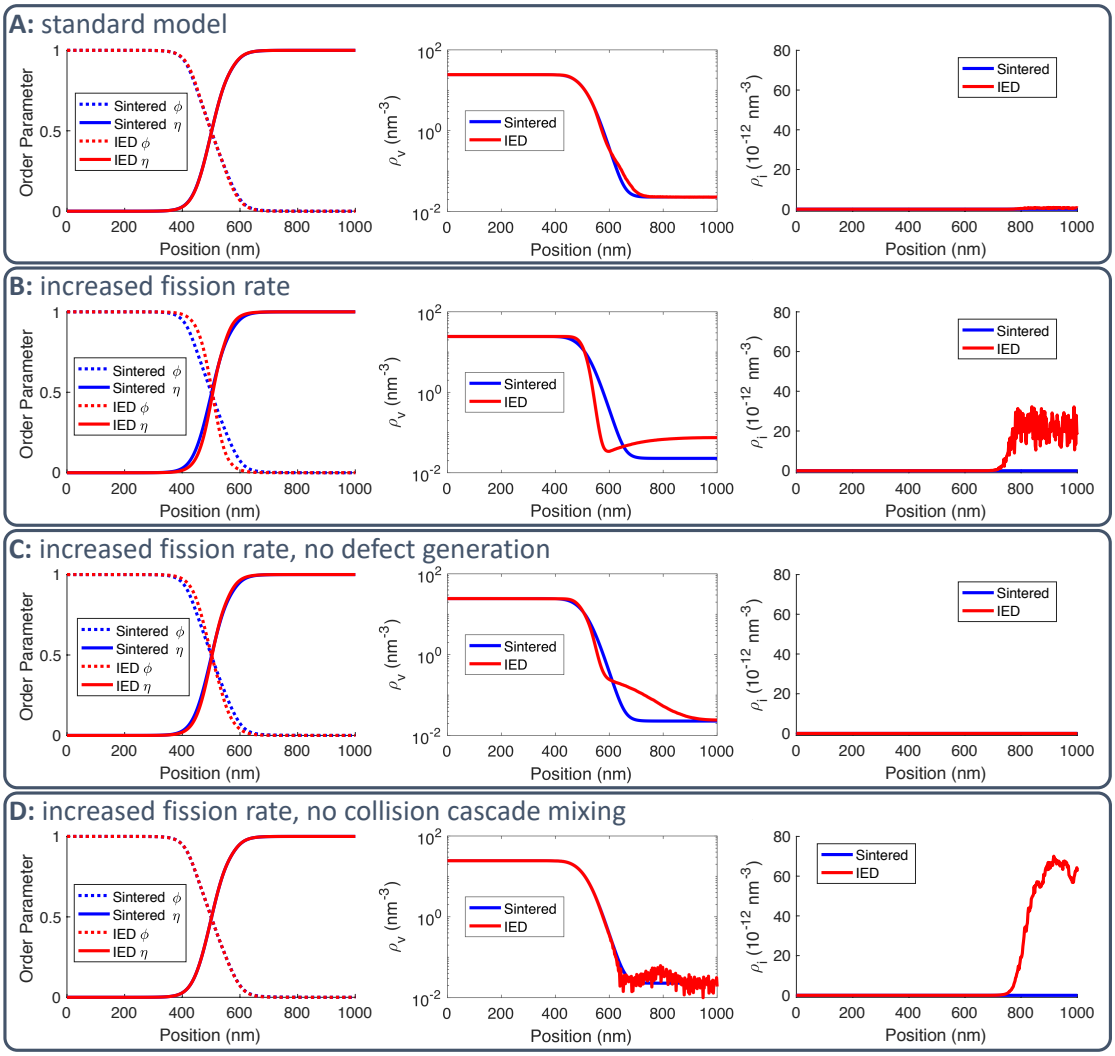

Figure 5.2. Results of 1D IED study. Each figure compares a baseline sintering simulation ($\dot{f} = 0$) with an IED simulation. Each row plots from left to right: The order parameter values, the vacancy defect density on a log-scale, and the interstitial defect density. (A) Simulation using the parameters from Sec. 5.2.3 and an interface width of $\ell = 100$ nm. (B) Simulation which increased the fission rate by a factor of 100. (C) Simulation which increased the fission rate by a factor of 100, but without any point defect generation or annihilation. (D) Simulation which increased the fission rate by a factor of 100, but without any athermal diffusion from collision cascade mixing.

effects. The second simulation includes IED effects, but with the fission rate increased by a factor of 100, similar to Sec. 5.3, to exaggerate the effects of radiation. The last two cases keep the exaggerated fission rate, but remove the effects of point defect generation and collision cascade mixing, respectively. This set of simulations lets us examine the relative strength of increased point defect density and of collision cascade mixing.

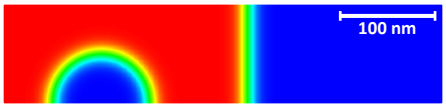

Figure 5.3. Example initial condition used in set of 2D simulations designed to compare the relative strengths of point defect changes and collision cascade mixing.

The results of this set of simulations are shown in Fig. 5.4. The point defect generation and annihilation case almost perfectly overlaps the baseline sintered case. Likewise, the collision cascade mixing case almost perfectly matches the IED case with both mechanisms. This suggests that collision cascade mixing is increasing the self-diffusion rate much more than the increased point defect concentration. Therefore, collision cascade mixing is the dominant effect.

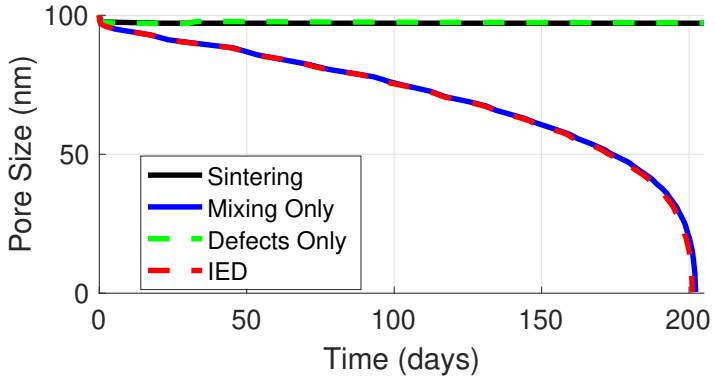

Figure 5.4. Results of 2D simulations separating the effects of point defect generation and collision cascade mixing. Collision cascade mixing accounts for almost all of the effect from IED.

This may help explain the apparent contradiction between Freshley et al. [10] and Bai et al. [133]. Freshley et al. found that small-grained systems are more affected by IED, but Bai et al. found that grain boundaries reduce the accumulation of point defects. If the point defect densities are not a significant driver of IED, then lowering the defect densities will not decrease the pore evacuation rate.

5.4.2 Intragranular Pores

This set of simulations examines the evacuation rate of intragranular pores. One quarter of a spherical pore is surrounded by a 100 nm thick spherical grain. Four pore sizes are used with sizes of 100, 200, 400, and 800 nm. The 3D simulation domain varies to adapt to the size of the pore, with a 40 nm buffer region between the edge of the grain and the edge of the domain. Elements are 5 nm cubes. An example domain is shown in Fig. 5.5.

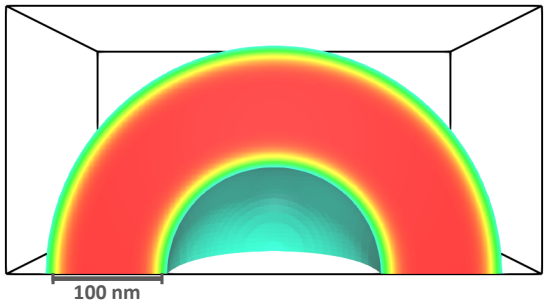

Figure 5.5. Example initial condition used for 3D simulations to examine the effects of intragranular pore size. This is the 200 nm pore case. There are also 100, 400, and 800 nm cases. In each case the grain radius is 100 nm larger than the pore radius.

Each pore size listed above is used in two simulations; one baseline sintering simulation and one with IED effects. The pore size evolution is shown in Fig. 5.6, normalized by taking the difference between the initial pore size and the measured pore size. IED is clearly increasing the pore evacuation rate in all cases.

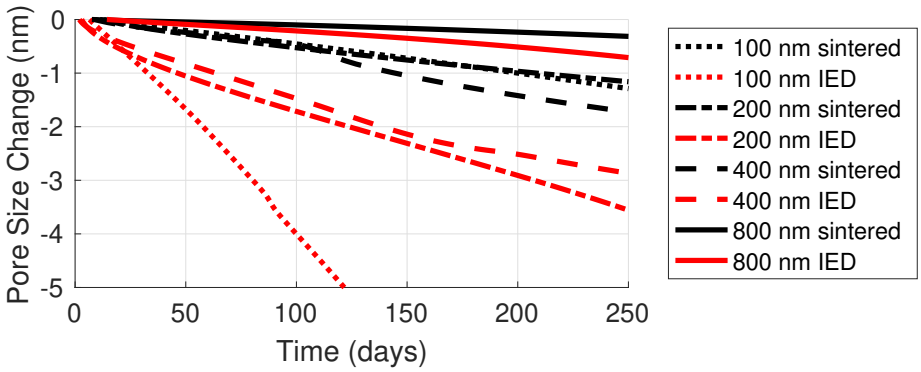

Figure 5.6. Results of evacuation simulations using intragranular pores. The pore size is normalized by taking the difference between the initial pore size and the measured pore size. Smaller pores evacuate faster than large pores.

To quantify the correlation between pore size and the relative effect of IED, we measure the average slope of each line from Fig. 5.6, and then take the ratio of the IED slope with the baseline sintered slope to calculate an IED multiplier. The values of this multiplier are plotted against the original pore size in Fig. 5.7. This IED multiplier is the same whether measuring the diameter change or the volume change of the pore. This figure shows that the effect of IED on the evacuation rate decreases as the pore size increases, possibly as an exponential-decay function. This finding is consistent with experiments and IED theory and further verifies that our IED model is capturing the correct physics. However, most pores are not intragranular [11]. It is worth replicating

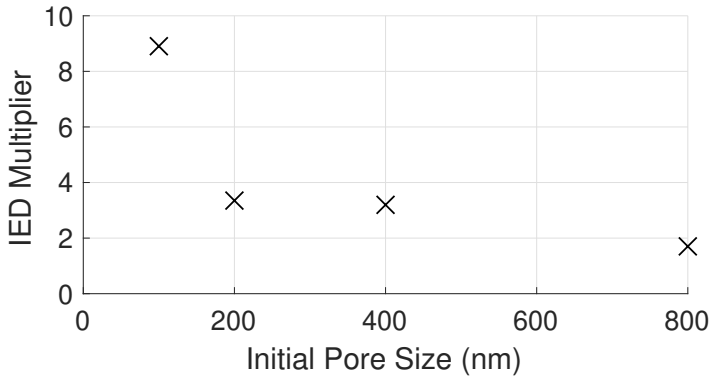

Figure 5.7. Ratio of the evacuation rates for IED and sintered simulations. When subjected to collision cascade damage, the 100 nm pore evacuates nearly 10 times faster. The 800 nm pore evacuates at a rate about two times faster.

this study on GB pores to see if the behavior is the same or if GBs affect the IED kinetics.

5.4.3 Grain Boundary Pores

The setup for this set of simulations is similar to Sec. 5.4.2, except that two grains are used with a GB down the center of the domain. The pore size is measured along the GB plane. A sample initial condition is shown in Fig. 5.8.

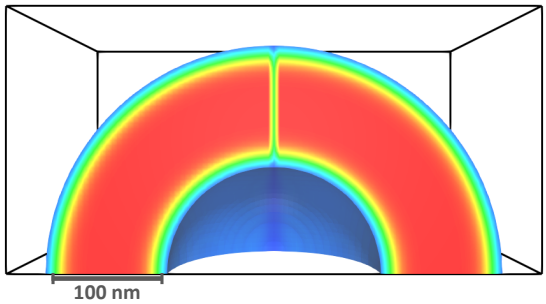

Figure 5.8. Initial condition used for 3D simulations to examine the effects of grain boundary pores size. The pore size was measured along the width of the grain boundary. This is the 200 nm case.

The results of this simulation are shown in Fig. 5.9. During the simulation, the GB would decrease in thickness as the pores became lenticular. In the 400 and 800 nm pore simulations, this went so far as to force the grains to split apart, making the results unusable. Therefore, Fig. 5.9 only includes the 100 and 200 nm pore sizes. Unlike Fig. 5.6, the pore size is not normalized, so the size of the pore is represented by where the lines cross the y-axis.

Unlike the intragranular pores, there is no significant difference between the sintered

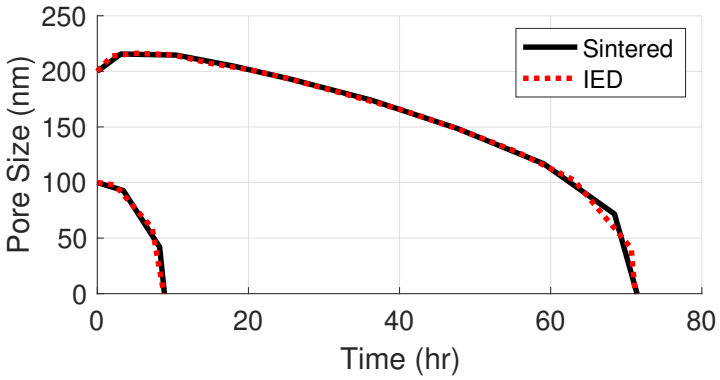

Figure 5.9. Results of evacuation simulations using grain boundary pores. There is no significant difference between sintered and IED simulations.

case and the IED case. Both pores close completely within a matter of hours. This suggests that GB pores are not as affected by IED as intragranular pores. The kinetics of the sintering model show why. Thermal diffusion is 10,000 times faster on GBs than through the bulk; while the largest IED multiplier was 8.9. Thus, on GBs, the kinetic effects of IED are being overwhelmed by the thermal GB kinetics.

There are some important limitations that should be considered with this result. First, the GB system represented here is not accurate to real microstructures. Both bulk and GB diffusion will occur faster in these test cases than in real UO_2 because of the small sizes of the pores and the short distance between the pore and the external void. The length of the GB that can be simulated is limited by the computational cost of the domain. However, a longer GB will be examined in Sec. 5.4.4. Also note that this simulation uses a single temperature. If the temperature lowers further, sintering kinetics may slow to the point that GB pores are affected by IED kinetics. Finally, intragranular pores are more likely to be of the small size associated with IED to begin with [6]. The energy associated with forming a pore is lower on GBs than in the bulk, so GB pores grow larger faster [18]. This GB effect on IED may have never been noticed before because the GB kinetics are primarily affecting pores that are too large to be affected by IED to begin with.

5.4.4 Sink Distance

We now examine the effect of grain size on IED. The average grain size of doped fuel can be many times larger than undoped UO_2 [36, 180], and therefore knowing the impact of grain size is critical to understand densification in doped fuel. We developed a stable microstructure with a GB passing close to a pore before connecting with an external

void. This way, the GB acts as fast diffusion path to the external void. A 100 nm pore is positioned 800 nm away from the void. Perpendicular to the surface is a GB that runs past the pore. Symmetry is used to keep the GB stable so that it does not migrate. This results in two pores and the microstructure shown in Fig. 5.10. The domain is 1,250 nm $\times$ 150 nm $\times$ the distance necessary to facilitate the requisite GB to pore distance. Once again the element are 5 nm cubes. The distance between the GB and the pore is set to one of five options: 0 nm, 50 nm, 100 nm, 200 nm, and 400 nm. The 0 nm case has the pore placed on the GB. The 100 nm case is shown as an example in Fig. 5.10. The behavior for each distance was simulated with and without radiation, making a total of ten simulations.

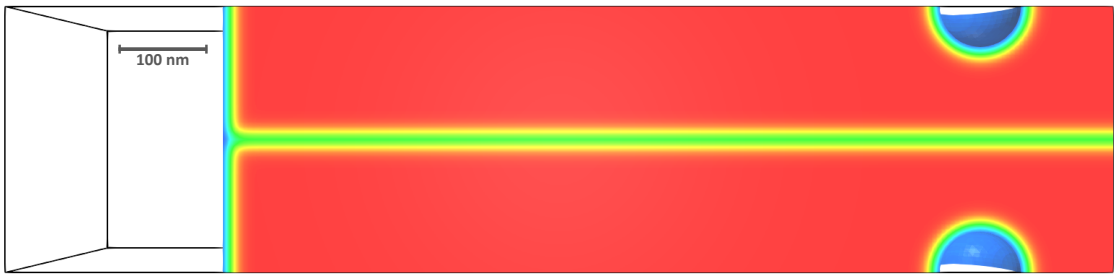

Figure 5.10. Initial condition used to examine the effect of sink distance on the evacuation rate of pores. In this case the distance between the pore and the GB is 100 nm.

The 0 nm GB distance case is used to compare the effects of the GB distance to the sink against the 100 nm pore case from Fig. 5.9. In both simulations, a 100 nm GB pore is allowed to evacuate. In one case the distance from the pore to the sink is 100 nm, in the other case the distance is 800 nm. The comparison is not perfect since one is a curved surface and the other is a flat surface, but the primary factor should still be the distance between the pore and the sink. Both cases are simulated with and without IED effects. The result of these simulations are shown in Fig. 5.11. Increasing the pore to sink distance decreased the pore evacuation rate, but the IED effect is still negligible.

The non-GB pore results are shown in Fig. 5.12. Note the different time scales in Figs. 5.11 and 5.12. The GB pore still evacuates significantly faster than the intragranular pores. All of the IED cases have faster pore evacuation than the sintered cases. However, for both sintering and IED, the 100 nm, 200 nm, and 400 nm cases overlap completely such that the distance to the GB has no effect beyond 50 nm.

There are two possible explanations for this result. One is that the GB distance does not affect the pore evacuation rate except when the pore is very close to the GB. The other explanation is that the external void is a much stronger sink, and its effects are overpowering the effects of the GB despite being much farther away. To test the

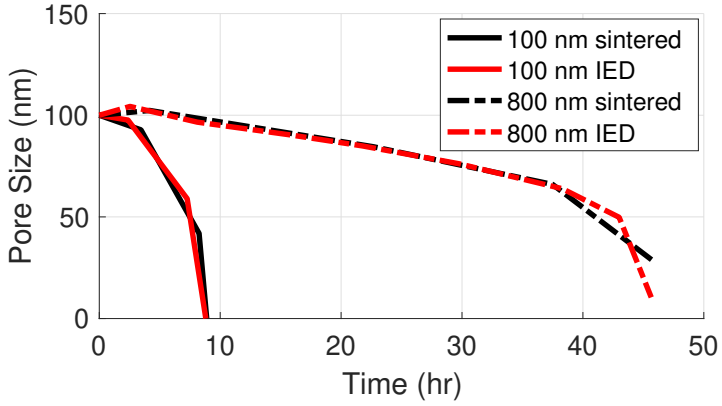

Figure 5.11. Comparison of 100 nm GB pores with different distances between the pore and the sink. One set of simulations has a GB to void distance of 100 nm, while in the other set the distance is 800 nm. The IED effect is again negligible. However, the effect of increasing the GB to void distance significantly slows down the evacuation rate.

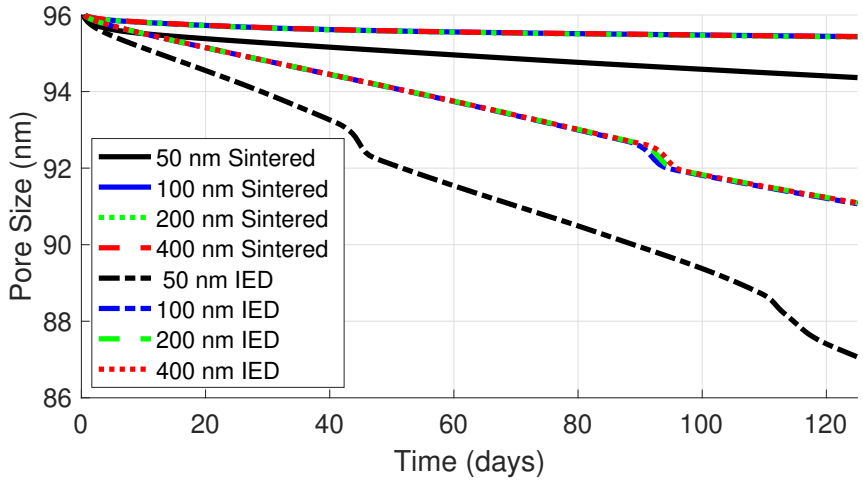

Figure 5.12. Results of varying the distance between intragranular pores and grain boundaries. Adding IED effects and being very close to the grain boundary both increased the evacuation rate. However, beyond 50 nm the distance had no effect.

second possibility, we run additional simulations using the geometry from Sec. 5.4.1, but varying the distance from the pore to the void to match those used above. The results are not shown, but the behavior was very similar to Fig. 5.12, suggesting that the first explanation is the correct one. However, while it is reasonable to suppose that there is a distance t which pores are able to interact with GBs, in a phase field simulation this distance is determined by the interface thickness, not the atomistic diffusion properties. As such, these results should not be used to determine the pore and GB interaction distance, because it is likely they are an effect of the phase field properties rather than

the material properties.

This result appears to contradict the findings of Freshley et al. [10]. However, a correlation between the grain size distribution and the pore size distribution could explain both effects. Kingery and François [41] found such a correlation when they examined the effects of pore sweeping by grain boundaries. As GBs migrate, they pick up intragranular pores and carry them along, causing pores to combine into ever-larger GB pores. If this is the case, then grain size indirectly influences the IED effect by increasing the average pore size and the GB pore fraction.

5.4.5 Neighboring Pore Interactions

Current models assume that pores within the same grain do not interact with one another [11, 142]. However, it is possible that one pore would act as a sink for the other, affecting their evacuation rates. The results of the previous simulation showed that the distance between the pore and a GB sink does not affect the evacuation rate, which increases confidence in this assumption. However, it is still possible that a nearby pore could bridge the gap between a pore and a GB. The final set of IED simulations is used to check if this affects the overall pore evacuation rate.

The simulation setup is demonstrated in Fig. 5.13. Three simulations are used: one with a 100 nm pore positioned 50 nm away from the surface, one with the pore positioned 200 nm away from the surface, and a third with both pores present so that the distance between them is 50 nm. Placing one pore directly in the diffusion path of the other pore and setting the distance between them to 50 nm should maximize the strength of any interaction.

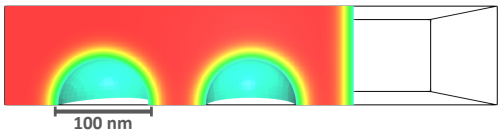

Figure 5.13. Initial condition used to examine pore-pore interactions. This case has both pores present, but the other cases include only one pore or the other.

The simulation results are shown in Fig. 5.14. The pore farther from the surface evacuates faster when the closer pore is also present, but the closer pore evacuates slower. We averaged the results for the individual cases and the combined case, and found that the overall effect is to reduce the average pore evacuation rate by 5.8%. Considering the relatively small effect even among this idealized geometry, the assumption that pores do not interact is likely justifiable.

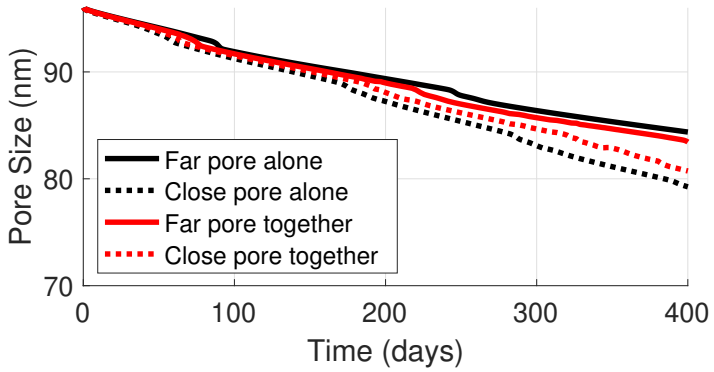

Figure 5.14. Results of two-pore IED interaction simulations. Having both pores causes the farther pore to evacuate faster and the closer pore to evacuate slower.

5.5 Conclusions and Future Work

We have proposed a mechanistic microstructural model to predict irradiation-enhanced densification in nuclear fuels. Once the model is validated, it should be able to provide physically reasonable predictions of non-standard fuel structures (such as large-grained doped-UO_2) without needing to be fit to experimental data. We verified that the model is capturing the effects of IED by examining the interactions of the two mechanisms that were accounted for in the model: increased point defect densities and collision cascade mixing. Both effects are behaving as expected. We were also able to capture accelerated evacuation of small pores, which is a well-established feature of IED.

We used a series of simulations to examine some physical mechanisms of IED. Our results indicate that collision cascade mixing plays a larger role than the generation of point defects in the bulk. We found that GB pores are not affected by IED at the simulated temperature because thermal GB kinetics are already accelerated enough to overpower the effect. Additionally, it appears that grain size does not have a direct effect on IED. Rather, we suggest that larger-grained microstructures may be less affected because they have fewer small intragranular pores than small-grained microstructures. Therefore, large-grained UO_2 pellets manufactured via doped sintering may reduce the effects of IED, but this would be due to a reduction in small porosity not the large grain size. Finally, we found that the effects of pore-pore interactions are small, such that the assumption made in existing models that pores do not interact is probably valid.

None of these results are, by themselves, conclusive. First of all, the model does not capture direct pore damage by collision cascades, so the effect of that mechanism is not being considered. Additionally, too few simulations are used here to give an accurate quantification of any of these effects.

Future work should first focus on further development of the model to capture pore damage. Then the focus should be to give a more complete quantification of the relation between pore size, temperature, fission rate, and the pore evacuation rate via sensitivity analysis. Once this is done, the model can be used in conjunction with experimental data to develop a mechanistic macroscale IED model.

Chapter 6
Conclusions and Future Work

6.1 Summary and Contributions

This work details the development of the grand potential sintering model and its application to three types of UO_2 sintering. It improves upon previous models through a greater reliance on the four thermodynamic and kinetic driving forces of sintering and less reliance on fitting parameters. It's formulation also decouples the interface width from the interface energy, allowing for lower computational costs without affecting the thermodynamics.

In Chapter 3 the model is developed and applied to standard thermal sintering. The model is verified by adjusting the model parameters that relate to the sintering driving forces and by showing that the model predictions change in a realistic manner. By comparing to analytical models it is shown that the grand potential sintering model is giving reasonable behavior compared to sintering theory. The model is also compared to experimental data [8]. It over-predicts the sintering rate, likely caused by uncertainty in the material properties used in the model and the small size of the simulation. These results suggest that the model accurately captures sintering physics, but that more data are needed to accurately represent material properties.

Chapter 4 applies the model to the study of doped-UO_2. The vacancy concentrations are adjusted based on atomistic simulations of undoped, Cr-doped, and Mn-doped UO_2. Then, the relative behavior of these dopants is tested in terms of both the sintering rate and the grain growth rate. In small-scale test simulations, the relative effect of dopants on both the sintering rate and grain growth rate are consistent with experiments [36,180]. However, in a large 100-particle simulation, the relative grain growth rates does not match experiments. Further study shows that this is likely caused by the temperature profile of the simulation, which does not match the isothermal annealing used to measure

grain growth in experiments. These results predict that Mn-doped UO_2 will enhance the microstructural properties of UO_2 even more than Cr-doped UO_2 and may be a viable near-term deployable accident-tolerant fuel.

In Chapter 5, additional terms are added to capture two of the three major drivers of irradiation-enhanced densification (IED). The adjusted model is verified by analyzing the pseudo-steady state behavior of 1D simulations to verify that the vacancy and interstitial defect concentrations behave as expected. It is also verified that the multiplier effect of IED is greater on small pores, as is expected based on experimental data [1](Chapter 2). The model is then used to study IED pore and grain boundary interactions using several small-scale test simulations. Results show that small, intragranular pores are affected by IED, while grain boundary pores see no change in behavior. It is also shown that grain size does not affect IED directly, but likely affects it indirectly by reducing the number of small intragranular pores. Simulations also show that the interactions between neighboring pores are unlikely to affect the overall densification rate. These results should simplify future macroscale IED model development for fuel performance codes by eliminating point defect concentration and grain size from the controlling variables.

6.2 Suggestions for Future Work

The results presented in this work are neither finished nor conclusive. Model validation has not been completed, in part because of poor experimental data. Therefore, additional experiments should be performed to more accurately measure the diffusivity of UO_2. Model validation may then proceed for UO_2 as well as other sintered materials. Experiments are also necessary to validate the conclusion that Mn-doped UO_2 results in larger grains and improves fuel performance over undoped or Cr-doped UO_2.

Additional simulations are necessary to better quantify the relationships between pore size, grain boundaries, temperature, and IED. Once these relationships are quantified, and their findings supported by experiments, they can be used to develop a new mechanistic fuel performance model for IED that is better equipped to predict densification behavior of new fuel or reactor concepts than the existing empirical models.

Appendix A
Initial Condition Generation Code

This is the necessary MATLAB scripts to generate the initial condition described in Sec. 4.6. It was written in MATLAB R2017a. Save the files to the MATLAB environment and run *input_3D.m*.

A.1 input_3D.m

```
%%
% *INPUT SCRIPT FOR INITIAL CONDITION GENERATION*

%   BOILER PLATE
% 3 dimensional
% 100 particles
% constant particle size distribution
% Box free energy function

clear
close all

%%
% *USER INPUTS*

%   PROBLEM SETUP
N = 100;                          % number of particles to simulate
dim = 3;                          % number of dimensions
b_lower = 0 * ones(1, dim);       % lower bounds in (x, y, z) directions
b_upper = [3700, 3700, 14000];    % upper bounds in (x, y, z) directions
v_size = [10, 10, 400, 1000];     % corner positions of figure
```

```
%   SOLVING PARAMETERS
ovrlp = 200 * ones(1, N);        % weighting to penalize particle overlap
d = 60;                          % distance particles travel every step
n_ic = 1000;                     % number of retries to make initial particle
                                 %    position non-overlapping
n_steps = 800;                   % maximum number of time steps to take
n_it = 3;                        % max number of steps to take to lower energy
                                 %    each time step
n_moves = 10;                    % number of tries to move particle before
                                 %    skipping it
min_radius = 100;

%   INPUT FUNCTIONS
% Function inputs
h_max = 50;                      % maximum height of free energy function

% Energy and energy gradient functions
Energy = @(p, n) boxE(n, p, b_upper, b_lower, h_max, ovrlp(n));
grad_Energy = @(p, n) grad_boxE(n, p, b_upper, b_lower, h_max, ovrlp(n));

% Particle size distribution function
part_dist = @(x) 350 * ones(size(x));
%part_dist = @(x) 400 + 1000 * sort(x, 'descend');

% Energy reducer function
E_red = @(p, n, n_it, Dx) pusher_box(p, n, n_it, Dx, b_upper, b_lower, h_max, ovrlp(n));

%   OUTPUT PARAMETERS
file_name = '3D_doped3.txt';     % text file name
movie = true;                    % output a movie file?
movie_file ='3D_doped3.avi';     % movie file name
plot_E = false;                  % plot the energy function (only in 2D)

%%
% *RUN INPUT SCRIPT*

%Plot the energy function
if plot_E == true
    n_pts = 201;
    eee(1).r = 0;
    x_E = linspace(b_lower(1), b_upper(1), n_pts);
    y_E = linspace(b_lower(2), b_upper(2), n_pts);
    E_E = zeros(length(x_E), length(y_E));
    for i = 1:n_pts
```

```
        for j = 1:n_pts
            eee(1).x = [x_E(i), y_E(j)];
            E_E(j,i) = Energy(eee, 1);
        end
    end
end

Driver
```

A.2 Driver.m

```
%%%%%%%%%%%%%%%%%%%%%%%%%%%%%%%%%%%%%%%%%%%%%%%%%%%%%%%%%%%%%%%%%%%%%%%%
% This script builds a series of 3D contacting spherical    %
% particles. It builds on the work of Bruce Berry of the    %
% University of Arkansas. This file must be run from an     %
% input file which gives a list of paramters to control the %
% simulation.                                               %
%                                                           %
% Sphere coordinates (x, y, z) and radii are output to a    %
% .txt file where they can be read in by MOOSE              %
%                                                           %
% Coded by Ian Greenquist                                   %
% Penn State University                                     %
% Department of Mechanical and Nuclear Engineering          %
% Last updated on 02/01/2018                                %
%                                                           %
%%%%%%%%%%%%%%%%%%%%%%%%%%%%%%%%%%%%%%%%%%%%%%%%%%%%%%%%%%%%%%%%%%%%%%%%

%%
% *INSERT DEFAULT VALUES TO INPUT VARIABLES*
if exist('n_moves', 'var') == 0
    n_moves = 4;
end

if exist('n_it', 'var') == 0
    n_it = 3;
end

if exist('min_radius', 'var') == 0
    min_radius = 0;
end

if exist('dim', 'var') == 0
    dim = 2;
```

```
end

if exist('movie', 'var') == 0
    movie = false;
end

if exist('n_ic', 'var') == 0
    n_ic = N;
end

if exist('v_size', 'var') == 0
    v_size = [10, 10, 650, 600];
end

%%
% *INITIALIZE PARTICLES*
n = 1;
it = 0;
r_def = false;

x_rnd = rand(N, 1);
r_list = part_dist(x_rnd);
rmin_frac = sum(r_list<=min_radius) / N;
disp(['Minimum radius fraction = ', num2str(rmin_frac)])

while n <= N
    %   Define particle radius
    if r_def == false               %has the particle radius already been defined?
        p(n).r = r_list(n);         %particle radius distribution
        if p(n).r < min_radius
            p(n).r = min_radius;
        end
        r_def = true;
        p(n).moves = n_moves;       %Defines how mobile the particle is
    end

    cont = true;
    %   Define position
    for i = 1: dim
        p(n).x(i) = (b_upper(i) - b_lower(i) -...
            2 * p(n).r) * rand + b_lower(i) + p(n).r;
    end
    %   check if position overlaps
    for i = 1: n-1
        if it >= n_ic
```

```
            error(['Can not find space for ',...
                num2str(N), ' particles in domain.'])
        end
        r = norm(p(n).x - p(i).x);
        if r < (p(n).r + p(i).r)
            it = it + 1;
            cont = false;
            break
        end
    end
    %   Continue to next particle
    if cont == true
        n = n + 1;                  %move to the next particle
        r_def = false;
    end
end %while n <= N

%%
% *INITIAL ENERGY CALCULATION*

clear r_def cont it r_def n_ic

%   Calculate Initial Energy
for n = 1: N
    p(n).E = Energy(p, n);
end

t = 0;

if plot_E == true
    plotfunction(p, b_lower, b_upper, v_size, x_E, y_E, E_E)
else
    plotfunction(p, b_lower, b_upper, v_size)
end
if movie == true
    frame(1) = getframe;
end
%%
% *ADJUST POSITIONS TO REDUCE ENERGY*

%   Time steps
for t = 1: n_steps
    E_new = 0;
    moves_max = 0;
    %   Move particles
```

```
    for n = 1: N
        if p(n).moves > 0           %only move the particles that are still mobile
            x_last = p(n).x;
            E_last = p(n).E;

            stp = false;            %stop trying to reduce the particle's energy?
            it = 0;                 %number of iterations
            while stp == false
                it = it + 1;
                gradE = grad_Energy(p, n);
                Dx = d * gradE / norm(gradE);
                p(n).x = p(n).x - Dx;%move the particle to minimize energy
                p(n).E = Energy(p, n);
                if p(n).E < E_last  %the energy has been reduced
                    stp = true;     %stop moving it
                    p(n).moves = n_moves;%reset the number of moves
                elseif it >= n_it   %the energy could not be reduced
                    stp = true;     %reset to its original position
                    p(n).E = E_last;
                    p(n).x = x_last;
                    p(n).moves = p(n).moves - 1;%take away a move
                else
                    %moving the particle increased the energy, try to reduce it
                    p = E_red(p, n, n_it, Dx);
                end
            end                     %while stp == false
        end                         %if p(n).moves > 0
        if p(n).moves > moves_max
            moves_max = p(n).moves;
        end
    end
    if plot_E == true
        plotfunction(p, b_lower, b_upper, v_size, x_E, y_E, E_E)
    else
        plotfunction(p, b_lower, b_upper, v_size)
    end
    if movie == true
        frame(t+1) = getframe;
    end
    if moves_max <= 0
        %none of the particles are mobile so end the simulation
        break
    end
end                                 %for t = 1: n_steps
```

```
%%
% *SAVE TO FILE

A = zeros(N, 3);
R = zeros(2, 3);

if dim == 1
    for n = 1:N
        A(n, 1) = p(n).x(1);
    end
elseif dim == 2
    for n = 1:N
        A(n,1) = p(n).x(1);
        A(n,2) = p(n).x(2);
    end
else
    for n = 1:N
        A(n,1) = p(n).x(1);
        A(n,2) = p(n).x(2);
        A(n,3) = p(n).x(3);
    end
end

R(1,:) = min(A);
R(2,:) = max(A);

fileID = fopen(file_name, 'w');
fprintf(fileID, '%8s %12s %12s %8s\n', 'x', 'y', 'z', 'r');
for n = 1:N
    fprintf(fileID, '%12.6f %12.6f %12.6f %8.4f\n',...
        A(n,1), A(n,2), A(n,3), p(n).r);
end

%%
% *MAKE MOVIE

if movie == true
    mov = VideoWriter(movie_file);
    mov.FrameRate = 5;
    open(mov);
    for n = 1:t+1
        writeVideo(mov, frame(n).cdata);
    end
    close(mov);
end
```

A.3 boxE.m

```
function [ E ] = boxE( n, p, b_upper, b_lower, E_max, E_ovr )
%BOXE It's like particle-in-a-box, but with more particles and fewer waves.

%   INPUTS:
% n = The current particle number
% p = All particle information
% b_upper = Upper bounds on domain
% b_lower = Lower bounds on domain
% E_max = Maximum Energy reached in the corners of the domain
% E_ovr = Overlap energy coefficient

%   OUTPUTS:
% E = particle n's energy

%Constants
dim = length(b_upper);
N = length(p);

%Function Energy
FE = p(n).x(dim) / b_upper(dim) * E_max;

%Box Energy
BE = 0;
for i = 1:dim
    if p(n).x(i) - p(n).r < b_lower(i)
        d = 1.0 + b_lower(i) + p(n).r - p(n).x(i);
        BE = BE + E_ovr * d;
    elseif p(n).x(i) + p(n).r > b_upper(i)
        d = 1.0 + p(n).x(i) + p(n).r - b_upper(i);
        BE = BE + E_ovr * d;
    end
end

%Overlap Energy
%   Determine Overlap Energy
OE = 0;
for m = 1:N
    if m ~= n
        r = norm(p(n).x - p(m).x);
        d = p(n).r + p(m).r;
```

```
        if r < d
            OE = OE + E_ovr * (1 + d - r);
        end
    end
end

E = FE + BE + OE;
end
```

A.4 grad_boxE.m

```
function [ gradE ] = grad_boxE( n, p, b_upper, b_lower, E_max, E_ovr )
%GRAD_BOXE Pseudogradient of boxE energy function

dim = length(b_upper);
N = length(p);

gradFE = zeros(size(b_upper));
gradBE = gradFE;
gradOE = gradFE;

gradFE(dim) = E_max / b_upper(dim);

for i = 1:dim
    if p(n).x(i) - p(n).r < b_lower(i)
        gradBE(i) = -E_ovr;
    elseif p(n).x(i) + p(n).r > b_upper(i)
        gradBE(i) = E_ovr;
    end
end

for m = 1:N
    if m ~= n
        r = norm(p(n).x - p(m).x);
        if r < p(n).r + p(m).r
            gradOE = gradOE + (p(m).x - p(n).x) / r;
        end
    end
end

gradE = gradFE + gradBE + gradOE;

end
```

A.5 pusher_box.m

```
%%%%%%%%%%%%%%%%%%%%%%%%%%%%%%%%%%%%%%%%
% This script attempts to allow         %
% particles to push off eachother.      %
%%%%%%%%%%%%%%%%%%%%%%%%%%%%%%%%%%%%%%%%

function p_new = pusher_box(p, n, n_it, Dx, b_upper, b_lower, E_max, w_o)

%disp(['Called function pusher, n = ', num2str(n)])
p_new = p;
N = length(p);
i = 0;
stp = false;
m = 0;

while stp == false
    i = i + 1;
    if i ~= n
        D_r = p(n).r + p(i).r;
        D_x = norm(p(n).x - p(i).x);
        if D_x < D_r
            stp = true;
            m = i;
        end
    end
    if i == N
        stp = true;
    end
end

if m ~= 0
    p_new(m).x = p(m).x - Dx;
    p_new(n).E = boxE(n, p, b_upper, b_lower, E_max, w_o);
    p_new(m).E = boxE(m, p, b_upper, b_lower, E_max, w_o);

    DE = p_new(n).E + p_new(m).E - p(n).E - p(m).E;
    if DE > 0 && n_it > 1
        p_new = pusher_box(p_new, m, n_it - 1, Dx, b_upper,...
            b_lower, E_max, w_o);
        DE = p_new(n).E + p_new(m).E - p(n).E - p(m).E;
    end

    if DE > 0
        p_new = p;
```

```
    end
end

end
```

A.6 plotfunction.m

```
%%
% PlotFunction: This script plots the current distribution of circles or
% spheres from Driver.m. Rewritten on 9/15/17 by Ian Greenquist

%%
function plotfunction(p, b_lower, b_upper, v_size, x_E, y_E, E_matrix)
% User parameters
res = 31; %resolution to use for circles and spheres
pause_time = 0.02; %time to pause between frames in s
set(gcf, 'units', 'points', 'position', v_size)

% Information from array
n_part = length(p); %number of particles
dim = length(p(1).x); %dimensions of system

% The nature of the plot changes depending on the dimension
if dim == 1
    theta = linspace(0, 2*pi, res);
    r_max = 0;
    for i = 1:n_part
        % check that lengths are uniform
        if length(p(i).r) ~= 1
            error(['Particle number ', num2str(i),...
                ' must be a one-dimensional value.'])
        end
        if length(p(i).x) ~= 1
            error(['Particle number ', num2str(),...
                ' is not one-dimensional.'])
        end

        % get maximum radius
        if p(i).r > r_max
            r_max = p(i).r;
        end

        % Convert to polar coordinates
        x = p(i).x + p(i).r * cos(theta);
```

```
        y = p(i).r * sin(theta);

        % Plot
        plot(x, y);
        hold on
    end

    axis([b_lower, b_upper, -1.1*r_max, 1.1*r_max])
elseif dim == 2
    if exist('x_E', 'var')
        contourf(x_E, y_E, E_matrix, 50, 'edgecolor', 'none')
        colorbar
        hold on
    end

    theta = linspace(0, 2*pi, res);
    for i = 1:n_part
        % check that lengths are uniform
        if length(p(i).r) ~= 1
            error(['Particle number ', num2str(i), ...
                ' must be a one-dimensional value.'])
        end
        if length(p(i).x) ~= 2
            error(['Particle number ', num2str(), ...
                ' is not two-dimensional.'])
        end

        % Convert to polar coordinates
        x = p(i).x(1) + p(i).r * cos(theta);
        y = p(i).x(2) + p(i).r * sin(theta);
        if exist('x_E', 'var')
            plot(x, y, 'w', 'linewidth', 2)
        else
            plot(x, y, 'k', 'linewidth', 2)
        end
        hold on
    end
    axis([b_lower(1), b_upper(1), b_lower(2), b_upper(2)])
    axis equal
%    set(gca, 'fontsize', 14)
elseif dim == 3
    for i = 1:n_part
        % check that lengths are uniform
        if length(p(i).r) ~= 1
            error(['Particle number ', num2str(i), ...
```

```
                ' must be a one-dimensional value.'])
        end
        if length(p(i).x) ~= 3
            error(['Particle number ', num2str(),...
                ' is not three-dimensional.'])
        end

        % generate sphere
        [x, y, z] = sphere(res);
        x = p(i).r * x + p(i).x(1);
        y = p(i).r * y + p(i).x(2);
        z = p(i).r * z + p(i).x(3);
        surfl(x, y, z)
        shading flat
        colormap('bone');
        hold on
    end
    axis manual
    axis equal
    axis([b_lower(1), b_upper(1), b_lower(2), b_upper(2),...
        b_lower(3), b_upper(3)])
else
    warning('The system cannot be plotted with the current dimensions.');
end
hold off
pause(pause_time)
end
```

Appendix B
Monte Carlo Density Measurement Code

This is an example of the code used to measure sintered density using Monte Carlo integration.

```
%% Boiler Plate
clear all
close all

%% Inputs
dim = 3;
path = 'path/to/csv/files/';
time_files = {'postprocessor_file_1.csv', 'postprocessor_file_2.csv'};
tcol = 1;
grain_files = {'vectorpostprocessor_base_file_1_',...
    'vectorpostprocessor_base_file_2_'};
lgd_txt = {'name_1', 'name_2'};
file_last = [999; 999]; %last vectorpostprocessor file to search for
varcol = 1; %column number of variable in vectorpostprocessors
Vcol = 2; %column number of volume in vectorpostprocessors
xyzcol = [4, 5, 6]; %column numbers of centroid coordinates in
                    %   vectorpostprocessors
pt_density = 1e-6; %MC point density
lineopts = {'-.b', '-b'}; %line styles for plot

%% Setup
if dim == 2
    f_r = @(V) sqrt(V ./ pi);
elseif dim == 3
    f_r = @(V) (3 * V ./ 4 ./ pi) .^ (1/3);
end
```

```
figure(1)
hold on

%% Calculate Densities
for sim = 1 : length(time_files)
%for sim = 4 : 4
    % Time
    tfile = importdata([path, time_files{sim}]);
    if isstruct(tfile)
        results(sim).t = tfile.data(:, tcol);
    elseif isa(tfile, 'double')
        results(sim).t = tfile(:, tcol);
    end
    nt = length(results(sim).t);

    % Density
    i = 0;
    rho = zeros(nt, 1);
    for fnum = 0 : file_last(sim)
        % Import data
        filename = generatefilename([path, grain_files{sim}], fnum);
        if exist(filename, 'file') == 2
            i = i + 1;
            grainfile = importdata(filename);
            var = grainfile.data(:, varcol);
            V = grainfile.data(:, Vcol);
            x = grainfile.data(:, xyzcol);
            V = V(var >= 0);
            x = x(var >= 0, :);
            r = f_r(V);

            % Number of MC points
            Vtot = 1;
            for j = 1 : dim
                Vtot = Vtot * (max(x(:, j)) - min(x(:, j)));
            end
            n_mc = uint32(Vtot * pt_density);

        % Calculate density
            results(sim).rho(i) = mchulldensity(x, r, n_mc);
            if results(sim).rho(i) > 1.0
                results(sim).rho(i) = 1.0;
            end
        end
    end
```

```
    % Plot results
    if results(sim).rho(end) == 0
        results(sim).t(end) = [];
        results(sim).rho(end) = [];
    end
    imin = find(results(sim).rho <= min(results(sim).rho * 1.05));
    plot(results(sim).t(imin(1):end) / 60,...
        results(sim).rho(imin(1):end) * 100, lineopts{sim}, 'linewidth', 3)
end

m_fit = [2.136e-4, 4.066e-4, 3.251e-4];
b_fit = [-1.371, -3.278, -2.497];
t_fit_end = [1.1212e4, 1.212e4, 1.212e4];

%% Finalize Plot
grid on
xlabel ('Time (min)')
ylabel('Relative Density (%)')
lgd = legend(lgd_txt);
set(gca, 'fontsize', 15)
set(lgd, 'location', 'best')
set(gcf, 'units', 'inches', 'position', [1, 1, 6, 4])
xlim([0, 200])
ylim([0, 100])
```

Bibliography

[1] Ian Greenquist, Michael R. Tonks, and Yongfeng Zhang. Review of sintering and densification in nuclear fuels: Physical mechanisms, experimental results, and computational models. Journal of Nuclear Materials, 507:381–395, August 2018.

[2] H. Stehle, H. Assmann, and F. Wunderlich. Uranium dioxide properties for LWR fuel rods. Nuclear Engineering and Design, 33(2):230–260, September 1975.

[3] H. Assmann and R. Manzel. The matrix swelling rate of UO2. Journal of Nuclear Materials, 68(3):360–364, November 1977.

[4] H. Assmann, W. Doerr, and M. Peehs. Oxide Fuels with Controlled Microstructure. Journal of the American Ceramic Society, 67(9):631–636, September 1984.

[5] D. G Martin. The thermal expansion of solid UO2 and (U, Pu) mixed oxides—a review and recommendations. Journal of Nuclear Materials, 152(2):94–101, May 1988.

[6] Eugene A. Olevsky. Theory of sintering: from discrete to continuum. Materials Science and Engineering: R: Reports, 23(2):41–100, June 1998.

[7] M. C. Paraschiv, A. Paraschiv, and V. V. Grecu. On the nuclear oxide fuel densification, swelling and thermal re-sintering. Journal of Nuclear Materials, 302(2–3):109–124, April 2002.

[8] R. C. Burk, T. W. Zawidzki, and P. S. Apte. Particle Size Distribution and Its Relation to Sintering—A Case Study for UO2 Powders. Journal of the American Ceramic Society, 66(11):815–818, November 1983.

[9] G. J. Dienes and A. C. Damask. Radiation Enhanced Diffusion in Solids. Journal of Applied Physics, 29(12):1713–1721, December 1958.

[10] M. D. Freshley, D. W. Brite, J. L. Daniel, and P. E. Hart. Irradiation-induced densification of UO2 pellet fuel. Journal of Nuclear Materials, 62(2):138–166, November 1976.

[11] V. I. Tarasov and M. S. Veshchunov. Models for fuel porosity evolution in UO2 under various regimes of reactor operation. Nuclear Engineering and Design, 272:65–83, June 2014.

[12] R. L. Williamson, J. D. Hales, S. R. Novascone, M. R. Tonks, D. R. Gaston, C. J. Permann, D. Andrs, and R. C. Martineau. Multidimensional multiphysics simulation of nuclear fuel behavior. Journal of Nuclear Materials, 423(1–3):149–163, April 2012.

[13] J. D. Hales, R. L. Williamson, S. R. Novascone, D. M. Perez, B. W. Spencer, and G. Pastore. Multidimensional multiphysics simulation of TRISO particle fuel. Journal of Nuclear Materials, 443(1–3):531–543, November 2013.

[14] Giovanni Pastore, Lelio Luzzi, Valentino Di Marcello, and Paul Van Uffelen. Physics-based modelling of fission gas swelling and release in UO2 applied to integral fuel rod analysis. Nuclear Engineering and Design, 256:75–86, March 2013.

[15] Michael Braginsky, Veena Tikare, and Eugene Olevsky. Numerical simulation of solid state sintering. International Journal of Solids and Structures, 42(2):621–636, January 2005.

[16] Michael R. Tonks, David Andersson, Simon R. Phillpot, Yongfeng Zhang, Richard Williamson, Christopher R. Stanek, Blas P. Uberuaga, and Steven L. Hayes. Mechanistic materials modeling for nuclear fuel performance. Annals of Nuclear Energy, 105:11–24, July 2017.

[17] H. Assmann and H. Stehle. Thermal and in-reactor densification of UO2: Mechanisms and experimental results. Nuclear Engineering and Design, 48(1):49–67, June 1978.

[18] R. J White. The development of grain-face porosity in irradiated oxide fuel. Journal of Nuclear Materials, 325(1):61–77, February 2004.

[19] Bruce J. Kellett and F. F. Lange. Thermodynamics of Densification: I, Sintering of Simple Particle Arrays, Equilibrium Configurations, Pore Stability, and Shrinkage. Journal of the American Ceramic Society, 72(5):725–734, May 1989.

[20] F. F. Lange and Bruce J. Kellett. Thermodynamics of Densification: II, Grain Growth in Porous Compacts and Relation to Densification. Journal of the American Ceramic Society, 72(5):735–741, May 1989.

[21] Eugene A. Olevsky, Veena Tikare, and Terry Garino. Multi-Scale Study of Sintering: A Review. Journal of the American Ceramic Society, 89(6):1914–1922, June 2006.

[22] Jane R. Blackford. Sintering and microstructure of ice: a review. Journal of Physics D: Applied Physics, 40(21):R355, 2007.

[23] R. L. Coble. Sintering Crystalline Solids. I. Intermediate and Final State Diffusion Models. Journal of Applied Physics, 32(5):787–792, May 1961.

[24] R. L. Coble. Sintering Crystalline Solids. II. Experimental Test of Diffusion Models in Powder Compacts. Journal of Applied Physics, 32(5):793–799, May 1961.

[25] Im Doo Jung, Sangyul Ha, Seong Jin Park, Deborah C. Blaine, Ravi Bollina, and Randall M. German. Two-Phase Master Sintering Curve for 17–4 PH Stainless Steel. Metallurgical and Materials Transactions A, 47(11):5548–5556, November 2016.

[26] Kirill I. Rybakov, Eugene A. Olevsky, and Ekaterina V. Krikun. Microwave Sintering: Fundamentals and Modeling. Journal of the American Ceramic Society, 96(4):1003–1020, April 2013.

[27] Lihao Ge, Ghatu Subhash, Ronald H. Baney, James S. Tulenko, and Edward McKenna. Densification of uranium dioxide fuel pellets prepared by spark plasma sintering (SPS). Journal of Nuclear Materials, 435(1–3):1–9, April 2013.

[28] Zhichao Chen, Ghatu Subhash, and James S. Tulenko. Master sintering curves for UO2 and UO2–SiC composite processed by spark plasma sintering. Journal of Nuclear Materials, 454(1–3):427–433, November 2014.

[29] J. Williams, E. Barnes, R. Scott, and A. Hall. Sintering of uranium oxides of composition UO2 to U3O8 in various atmospheres. Journal of Nuclear Materials, 1(1):28–38, April 1959.

[30] Y. Harada. UO2 sintering in controlled oxygen atmospheres of three-stage process. Journal of Nuclear Materials, 245(2):217–223, June 1997.

[31] Lihao Ge, Ghatu Subhash, Ronald H. Baney, and James S. Tulenko. Influence of processing parameters on thermal conductivity of uranium dioxide pellets prepared by spark plasma sintering. Journal of the European Ceramic Society, 34(7):1791–1801, July 2014.

[32] Susumu Fukushima, Toshihiko Ohmichi, Atsushi Maeda, and Hitoshi Watanabe. The effect of gadolinium content on the thermal conductivity of near-stoichiometric (U,Gd)O2 solid solutions. Journal of Nuclear Materials, 105(2):201–210, February 1982.

[33] S. M. Ho and K. C. Radford. Structural Chemistry of Solid Solutions in the UO2-Gd2O3 System. Nuclear Technology, 73(3):350–360, June 1986.

[34] H. Assmann, W. Dorr, and M. Peehs. Control of UO2 microstructure by oxidative sintering. Journal of Nuclear Materials, 140(1):1–6, August 1986.

[35] Carol A. Handwerker, Patricia A. Morris, and Robert L. Coble. Effects of Chemical Inhomogeneities on Grain Growth and Microstructure in Al2O3. Journal of the American Ceramic Society, 72(1):130–136, January 1989.

[36] L. Bourgeois, Ph. Dehaudt, C. Lemaignan, and A. Hammou. Factors governing microstructure development of Cr2O3-doped UO2 during sintering. Journal of Nuclear Materials, 297(3):313–326, September 2001.

[37] J. M. Pope and K. C. Radford. Stable reactor fuel of controlled density using active UO2 powders. Materials Research Bulletin, 11(5):585–592, May 1976.

[38] Randall M. German. Coarsening in Sintering: Grain Shape Distribution, Grain Size Distribution, and Grain Growth Kinetics in Solid-Pore Systems. Critical Reviews in Solid State and Materials Sciences, 35(4):263–305, November 2010.

[39] Sudipta Biswas, Daniel Schwen, Jogender Singh, and Vikas Tomar. A study of the evolution of microstructure and consolidation kinetics during sintering using a phase field modeling based approach. Extreme Mechanics Letters, 7:78–89, June 2016.

[40] Mikhail S. Veshchunov. Modelling of Grain Growth Kinetics in Porous Ceramic Materials under Normal and Irradiation Conditions. Materials, 2(3):1252–1287, September 2009.

[41] W. D. Kingery and B. Francois. Grain Growth in Porous Compacts. Journal of the American Ceramic Society, 48(10):546–547, October 1965.

[42] Y. Harada. Sintering behaviour of niobia-doped large grain UO2 pellet. Journal of Nuclear Materials, 238(2):237–243, November 1996.

[43] Ryoichi Yuda and Katsumi Une. Effect of sintering atmosphere on the densification of UO2-Gd2O3 compacts. Journal of Nuclear Materials, 178(2):195–203, February 1991.

[44] J. Lechelle, R. Boyer, and M. Trotabas. A mechanistic approach of the sintering of nuclear fuel ceramics. Materials Chemistry and Physics, 67(1):120–132, January 2001.

[45] James D. Hansen, Richard P. Rusin, Mao-Hua Teng, and D. Lynn Johnson. Combined-Stage Sintering Model. Journal of the American Ceramic Society, 75(5):1129–1135, May 1992.

[46] Hunghai Su and D. Lynn Johnson. Master Sintering Curve: A Practical Approach to Sintering. Journal of the American Ceramic Society, 79(12):3211–3217, December 1996.

[47] S. Kiani, J. Pan, and J. A. Yeomans. A New Scheme of Finding the Master Sintering Curve. Journal of the American Ceramic Society, 89(11):3393–3396, November 2006.

[48] K. Maca, V. Pouchly, and A. R. Boccaccini. Sintering densification curve: A practical approach for its construction from dilatometric shrinkage data. Science of Sintering, 40(2):117–122, 2008.

[49] Deborah C. Blaine, John D. Gurosik, Seong Jin Park, Randall M. German, and Donald F. Heaney. Master sintering curve concepts as applied to the sintering of molybdenum. Metallurgical and Materials Transactions A, 37(3):715–720, March 2006.

[50] Kevin G. Ewsuk, Donald T. Ellerby, and Christopher B. DiAntonio. Analysis of Nanocrystalline and Microcrystalline ZnO Sintering Using Master Sintering Curves. Journal of the American Ceramic Society, 89(6):2003–2009, June 2006.

[51] S. J. Park, Randall M. German, J. M. Martin, J. F. Guo, and J. L. Johnson. Densification behavior of tungsten heavy alloy based on master sintering curve concept. Metallurgical and Materials Transactions A, 37(9):2837–2848, September 2006.

[52] Gaurav Aggarwal, Ivi Smid, Seong Jin Park, and Randall M. German. Development of niobium powder injection molding. Part II: Debinding and sintering. International Journal of Refractory Metals and Hard Materials, 25(3):226–236, May 2007.

[53] D. Li, S. Chen, Y. Jing, W. Shao, Y. Zhang, and W. Luan. The master sintering curve for pressure-less sintering of TiO2. Science of Sintering, 39(2):103–110, 2007.

[54] Yoshiaki Kinemuchi and Koji Watari. Dilatometer analysis of sintering behavior of nano-CeO2 particles. Journal of the European Ceramic Society, 28(10):2019–2024, 2008.

[55] A. Mashreghy and M. M. Moshksar. Densification and grain growth of nanocrystalline NiAl powder during pressureless sintering. International Journal of Modern Physics B, 22(18–19):2896–2904, July 2008.

[56] Darin A. Ray, Sarbjit Kaur, Raymond A. Cutler, and Dinesh K. Shetty. Effect of Additives on the Activation Energy for Sintering of Silicon Carbide. Journal of the American Ceramic Society, 91(4):1135–1140, April 2008.

[57] T. R. G. Kutty, K. B. Khan, A. Kumar, and H. S. Kamath. Densification strain rate in sintering of Tho2 and ThO2-0.25% Nb2O5 pellets. Science of Sintering, 41(2):103–115, 2009.

[58] M. V. Nikolic, N. Labus, and M. M. Ristic. Densification rate and phase structure changes during sintering of zinc titanate ceramics. Ceramics International, 35(8):3217–3220, December 2009.

[59] F. Raether and P. Schulze Horn. Investigation of sintering mechanisms of alumina using kinetic field and master sintering diagrams. Journal of the European Ceramic Society, 29(11):2225–2234, August 2009.

[60] W. Q. Shao, S. O. Chen, D. Li, H. S. Cao, Y. C. Zhang, and S. S. Zhang. Prediction and control of microstructure evolution for sub-microscale α-Al2O3 during low-heating-rate sintering based on the master sintering curve theory. Journal of the European Ceramic Society, 29(1):201–204, January 2009.

[61] Manish G. Bothara, Sundar V. Atre, Seong-Jin Park, Randall M. German, T. S. Sudarshan, and R. Radhakrishnan. Sintering Behavior of Nanocrystalline Silicon Carbide Using a Plasma Pressure Compaction System: Master Sintering Curve Analysis. Metallurgical and Materials Transactions A, 41(12):3252–3261, December 2010.

[62] Ricardo Caruso, Nadia Mamana, and Edgardo Benavidez. Densification kinetics of ZrO2-based ceramics using a master sintering curve. Journal of Alloys and Compounds, 495(2):570–573, April 2010.

[63] Takuya Hoshina, Yoichi Kigoshi, Tsutomu Furuta, Hiroaki Takeda, and Takaaki Tsurumi. Shrinkage Behaviors and Sintering Mechanism of BaTiO3 Ceramics in Two-Step Sintering. Japanese Journal of Applied Physics, 50(9S2):09NC07, September 2011.

[64] K. An. Pressure assisted master sintering surface of Co, Cu and Fe powder mixture. Powder Technology, 234:117–122, January 2013.

[65] Joydipta Banerjee, Aditi Ray, Arun Kumar, and Srikumar Banerjee. Studies on sintering kinetics of ThO2–UO2 pellets using master sintering curve approach. Journal of Nuclear Materials, 443(1–3):467–478, November 2013.

[66] Luz Stella Arias-Maya. Free and Constrained Sintering of 3-mol% Yttria Stabilised Zirconia. DYNA, 81(183):158–167, February 2014.

[67] Lili Guan, Shiru Le, Shaofei He, Xiaodong Zhu, Tao Liu, and Kening Sun. Densification Behavior and Space Charge Blocking Effect of Bi2O3 and Gd2O3 Co-doped CeO2 as Electrolyte for Solid Oxide Fuel Cells. Electrochimica Acta, 161:129–136, April 2015.

[68] John L. Johnson. Activated liquid phase sintering of W–Cu and Mo–Cu. International Journal of Refractory Metals and Hard Materials, 53, Part B:80–86, November 2015.

[69] Addison J. Rayner, Ryan M. C. Clemmer, and Stephen F. Corbin. Determination of the Activation Energy and Master Sintering Curve for NiO/YSZ Composite Solid Oxide Fuel Cell Anodes. Journal of the American Ceramic Society, 98(4):1060–1065, April 2015.

[70] Raghunath R. Thridandapani, Diane C. Folz, and David E. Clark. Effect of electric field (2.45 GHz) on sintering behavior of fully stabilized zirconia. Journal of the European Ceramic Society, 35(7):2145–2152, July 2015.

[71] Yong-Shin Lee, Sang-Jun Lee, Sangmok Lee, Eung-Zu Kim, and Duck Jae Yoon. Development of a Master Sintering Curve for Al-Mg Alloy. Advances in Materials Science and Engineering, 2016:e5607386, December 2016.

[72] I-Wei Chen, Gregory N. Hassold, and David J. Srolovitz. Computer Simulation of Final-Stage Sintering: II, Influence of Initial Pore Size. Journal of the American Ceramic Society, 73(10):2865–2872, October 1990.

[73] Gregory N. Hassold, I-Wei Chen, and David J. Srolovitz. Computer Simulation of Final-Stage Sintering: I, Model Kinetics, and Microstructure. Journal of the American Ceramic Society, 73(10):2857–2864, October 1990.

[74] Elizabeth A. Holm, James A. Glazier, David J. Srolovitz, and Gary S. Grest. Effects of lattice anisotropy and temperature on domain growth in the two-dimensional Potts model. Physical Review A, 43(6):2662–2668, March 1991.

[75] Wan Y. Shih, Wei-Heng Shih, and Ilhan A. Aksay. Elimination of an isolated pore: Effect of grain size. Journal of Materials Research, 10(4):1000–1015, April 1995.

[76] Y. Okamoto, N. Hirosaki, and H. Matsubara. A Study of Self-Reinforcement Phenomenon in Silicon Nitride by Monte-Carlo Simulation. MRS Online Proceedings Library Archive, 529, January 1998.

[77] Veena Tikare and James D. Cawley. Application of the Potts Model to Simulation of Ostwald Ripening. Journal of the American Ceramic Society, 81(3):485–491, March 1998.

[78] Veena Tikare and Elizabeth A. Holm. Simulation of Grain Growth and Pore Migration in a Thermal Gradient. Journal of the American Ceramic Society, 81(3):480–484, March 1998.

[79] P. Zeng and V. Tikare. Potts Model Simulation of Grain Size Distributions During Final Stage Sintering. MRS Online Proceedings Library Archive, 529, January 1998.

[80] Hideaki Matsubara. Computer simulations for the design of microstructural developments in ceramics. Computational Materials Science, 14(1âĂŞ4):125–128, February 1999.

[81] C Moron, M Mora, and A Garcia. Computer simulation of grain growth kinetics. Journal of Magnetism and Magnetic Materials, 215âĂŞ216:153–155, June 2000.

[82] Soon-Gi Shin. Experimental and simulation studies on grain growth in TiC and WC-based cermets during liquid phase sintering. Metals and Materials, 6(3):195–201, June 2000.

[83] Elizabeth A. Holm and Corbett C. Battaile. The computer simulation of microstructural evolution. JOM, 53(9):20–23, September 2001.

[84] Veena Tikare, Mark A. Miodownik, and Elizabeth A. Holm. Three-Dimensional Simulation of Grain Growth in the Presence of Mobile Pores. Journal of the American Ceramic Society, 84(6):1379–1385, June 2001.

[85] Sylvie BordÃĺre. Original Monte Carlo Methodology Devoted to the Study of Sintering Processes. Journal of the American Ceramic Society, 85(7):1845–1852, July 2002.

[86] R. A Sutton and G. B Schaffer. An atomistic simulation of solid state sintering using Monte Carlo methods. Materials Science and Engineering: A, 335(1–2):253–259, September 2002.

[87] Veena Tikare, Michael Braginsky, and Eugene A. Olevsky. Numerical Simulation of Solid-State Sintering: I, Sintering of Three Particles. Journal of the American Ceramic Society, 86(1):49–53, January 2003.

[88] Qiang Yu and Sven K. Esche. A Monte Carlo algorithm for single phase normal grain growth with improved accuracy and efficiency. Computational Materials Science, 27(3):259–270, May 2003.

[89] Daoli Zhang, Guang'an Weng, Shuping Gong, and Dongxiang Zhou. Computer simulation of grain growth of intermediateâĂŤand final-stage sintering and Ostwald ripening of BaTiO3-based PTCR ceramics. Materials Science and Engineering: B, 99(1–3):428–432, May 2003.

[90] A Shimosaka, S Ohtani, Y Shirakawa, and J Hidaka. Simulation of the formation of microstructures in sintering. Kagaku Kogaku Ronbunshu, 30(5):697–704, 2004.

[91] E. A. Olevsky, B. Kushnarev, A. Maximenko, V. Tikare, and M. Braginsky. Modelling of anisotropic sintering in crystalline ceramics. Philosophical Magazine, 85(19):2123–2146, July 2005.

[92] Takeshi Yamashita, Tomoki Uehara, and Ryuzo Watanabe. Multi-Layered Potts Model Simulation of Morphological Changes of the Neck during Sintering in Cu-Ni System. Materials Transactions, 46(1):88–93, 2005.

[93] S. Bordere. The impact of fluctuations on the sintering kinetics of two particles demonstrated through Monte Carlo simulation. Scripta Materialia, 55(10):879–882, November 2006.

[94] S. Bordere and D. Bernard. Full resolution of the Monte Carlo time scale demonstrated through the modelling of two-amorphous-particles sintering. Computational Materials Science, 43(4):1074–1080, October 2008.

[95] Bin Fang, Chuan-zhen Huang, Chong-hai Xu, and Sheng Sun. Numerical simulation of microstructural evolution of ceramic tool materials. Computational Materials Science, 44(2):707–715, December 2008.

[96] Hongmei Cheng, Chuanzhen Huang, Hanlian Liu, and Bin Zou. Monte Carlo simulation of microstructure evolution in nano-composite ceramic tool materials. Computational Materials Science, 47(2):326–331, December 2009.

[97] B. Fang, C. Z. Huang, H. L. Liu, C. H. Xu, and S. Sun. Monte Carlo simulation of grain-microstructure evolution in two-phase ceramic tool materials. Journal of Materials Processing Technology, 209(9):4568–4572, May 2009.

[98] Hee-Soo Kim and Jin-Woo Park. Computational Study on the Microstructural Evolution and the Change of Electrical Resistivity of Sintered Materials. Journal of Electronic Materials, 38(3):475–481, March 2009.

[99] Ram Devanathan, Laurent Van Brutzel, Alain Chartier, Christine Gueneau, Ann E. Mattsson, Veena Tikare, Timothy Bartel, Theodore Besmann, Marius Stan, and Paul Van Uffelen. Modeling and simulation of nuclear fuel materials. Energy & Environmental Science, 3(10):1406–1426, September 2010.

[100] Veena Tikare, Michael Braginsky, Didier Bouvard, and Alexander Vagnon. Numerical simulation of microstructural evolution during sintering at the mesoscale in a 3d powder compact. Computational Materials Science, 48(2):317–325, April 2010.

[101] Bin Fang, Chuan Zhen Huang, Chong Hai Xu, and Sheng Sun. Simulation of Fabrication for Single-Phase Al2O3 Ceramic Tool Materials at Different Fabrication Temperature. Advanced Materials Research, 150-151:1358–1363, 2011.

[102] Song Hao, Chuanzhen Huang, Bin Zou, Jun Wang, Hanlian Liu, and Hongtao Zhu. Three dimensional simulation of microstructure evolution for ceramic tool materials. Computational Materials Science, 50(12):3334–3341, December 2011.

[103] Bin Fang, Chuan Zhen Huang, Chong Hai Xu, and Sheng Sun. Simulation of Fabrication for Single-Phase Al2O3 Ceramic Tool Materials at Different Fabrication Pressure. Key Engineering Materials, 499:150–155, 2012.

[104] Bin Fang, Chuan Zhen Huang, Hong Tao Zhu, and Chong Hai Xu. Simulation of Fabrication for Al2O3 Ceramic Tool Materials. Advanced Materials Research, 500:537–543, 2012.

[105] Song Hao, Chuanzhen Huang, Bin Zou, Jun Wang, Hanlian Liu, and Hongtao Zhu. Three-dimensional simulation of microstructure evolution for three-phase nanocomposite ceramic tool materials. Computational Materials Science, 65:254–263, December 2012.

[106] Hong Mei Cheng and Chuan Zhen Huang. Simulation of the Effect of Sintering Pressure on Microstructure Evolution in Nanocomposite Ceramic Tool Materials. Applied Mechanics and Materials, 395-396:262–265, 2013.

[107] Eric R. Homer, Veena Tikare, and Elizabeth A. Holm. Hybrid Potts-phase field model for coupled microstructuralâĂŞcompositional evolution. Computational Materials Science, 69:414–423, March 2013.

[108] R. Bjork, H. L. Frandsen, V. Tikare, E. Olevsky, and N. Pryds. Strain in the mesoscale kinetic Monte Carlo model for sintering. Computational Materials Science, 82:293–297, February 2014.

[109] A. V. Galakhov. Powder Compact Structure. Part 3. Theoretical Analysis of Sintering in Powder Compacts with Inhomogeneous Porosity1. Refractories and Industrial Ceramics, 55(5):448–455, January 2015.

[110] Shaohua Chen, Yaopengxiao Xu, and Yang Jiao. Modeling morphology evolution and densification during solid-state sintering via kinetic Monte Carlo simulation. Modelling and Simulation in Materials Science and Engineering, 24(8):085003, 2016.

[111] D. Raabe. Scaling Monte Carlo kinetics of the Potts model using rate theory. Acta Materialia, 48(7):1617–1628, April 2000.

[112] Long-Qing Chen. Phase-Field Models for Microstructure Evolution. Annual Review of Materials Research, 32(1):113–140, 2002.

[113] Nele Moelans, Bart Blanpain, and Patrick Wollants. An introduction to phase-field modeling of microstructure evolution. Calphad, 32(2):268–294, June 2008.

[114] John W. Cahn and John E. Hilliard. Free Energy of a Nonuniform System. I. Interfacial Free Energy. The Journal of Chemical Physics, 28(2):258–267, February 1958.

[115] John W. Cahn. Free Energy of a Nonuniform System. II. Thermodynamic Basis. The Journal of Chemical Physics, 30(5):1121–1124, May 1959.

[116] Samuel M. Allen and John W. Cahn. A microscopic theory for antiphase boundary motion and its application to antiphase domain coarsening. Acta Metallurgica, 27(6):1085–1095, June 1979.

[117] A Kazaryan, Y Wang, and Bruce R Patton. Generalized phase field approach for computer simulation of sintering: incorporation of rigid-body motion. Scripta Materialia, 41(5):487–492, August 1999.

[118] A. Kazaryan, Y. Wang, S. A. Dregia, and Bruce R. Patton. Generalized phase-field model for computer simulation of grain growth in anisotropic systems. Physical Review B, 61(21):14275–14278, June 2000.

[119] Yu U. Wang. Computer modeling and simulation of solid-state sintering: A phase field approach. Acta Materialia, 54(4):953–961, February 2006.

[120] Karim Ahmed, Janne Pakarinen, Todd Allen, and Anter El-Azab. Phase field simulation of grain growth in porous uranium dioxide. Journal of Nuclear Materials, 446(1âĂŞ3):90–99, March 2014.

[121] Yamato Fukui, Tomoyuki Fujii, Keiichiro Tohgo, and Yoshinobu Shimamura. Multi-physics simulation of oxygen diffusion in PSZâĂŞTi composites during spark plasma sintering process. Computational Materials Science, 95:29–34, December 2014.

[122] Kazunari Shinagawa. Simulation of grain growth and sintering process by combined phase-field/discrete-element method. Acta Materialia, 66:360–369, March 2014.

[123] Rui-jie Zhang, Zhong-wei Chen, Wei Fang, and Xuan-hui Qu. Thermodynamic consistent phase field model for sintering process with multiphase powders. Transactions of Nonferrous Metals Society of China, 24(3):783–789, March 2014.

[124] Karim E. Ahmed. Phase field modeling of grain growth in porous polycrystalline solids. Ph.D., Purdue University, United States – Indiana, 2015.

[125] Michael R. Tonks, Yongfeng Zhang, Aaron Butterfield, and Xian-Ming Bai. Development of a grain boundary pinning model that considers particle size distribution using the phase field method. Modelling and Simulation in Materials Science and Engineering, 23(4):045009, 2015.

[126] S. B. Biner. Pore and grain boundary migration under a temperature gradient: a phase-field model study. Modelling and Simulation in Materials Science and Engineering, 24(3):035019, 2016.

[127] Johannes HÃűtzer, Veronika Rehn, Wolfgang Rheinheimer, Michael J. Hoffmann, and Britta Nestler. Phase-field study of pore-grain boundary interaction. Journal of the Ceramic Society of Japan, 124(4):329–339, 2016.

[128] K. Chockalingam, V. G. Kouznetsova, O. van der Sluis, and M. G. D. Geers. 2d Phase field modeling of sintering of silver nanoparticles. Computer Methods in Applied Mechanics and Engineering, 312:492–508, December 2016.

[129] Karim Ahmed, Michael Tonks, Yongfeng Zhang, Bulent Biner, and Anter El-Azab. Particle-grain boundary interactions: A phase field study. Computational Materials Science, 134:25–37, June 2017.

[130] D. A. Banks. Some observations of density and porosity changes in UO2 fuel irradiated in water-cooled reactors. Journal of Nuclear Materials, 54(1):97–107, November 1974.

[131] H. Stehle and H. Assmann. The dependence of in-reactor UO2 densification on temperature and microstructure. Journal of Nuclear Materials, 52(2):303–308, October 1974.

[132] H. Stehle and H. Assmann. In-reactor UO2 densification. Journal of Nuclear Materials, 61(3):326–329, 1976.

[133] Xian-Ming Bai, Arthur F. Voter, Richard G. Hoagland, Michael Nastasi, and Blas P. Uberuaga. Efficient Annealing of Radiation Damage Near Grain Boundaries via Interstitial Emission. Science, 327(5973):1631–1634, March 2010.

[134] P. R. Roy and D. N. Sah. Irradiation behaviour of nuclear fuels. Pramana, 24(1-2):397–421, January 1985.

[135] S. R. Macewen and I. J. Hastings. A model for in-reactor densification of UO2. Philosophical Magazine, 31(1):135–143, January 1975.

[136] Hj Matzke. Radiation enhanced diffusion in UO2 and (U, Pu)O2. Radiation Effects, 75(1–4):317–325, January 1983.

[137] S. S. Dwaraknath and G. S. Was. Radiation enhanced diffusion of cesium, strontium, and europium in silicon carbide. Journal of Nuclear Materials, 474:76–87, June 2016.

[138] P. E. MacDonald and L. B. (eds) Thompson. Matpro: A Handbook of Materials Properties for Use in the Analysis of Light Water Reactor Fuel Rod Behavior. Technical Report ANCR-1263, SEE CODE- 9502158 Aerojet Nuclear Co., Idaho Falls, Idaho (USA). Idaho National Engineering Lab., February 1976.

[139] G. Maier, H. Assmann, and W. DÃűrr. Resinter testing in relation to in-pile densification. Journal of Nuclear Materials, 153:213–220, April 1988.

[140] J. A. Turnbull. The effect of grain size on the swelling and gas release properties of UO2 during irradiation. Journal of Nuclear Materials, 50(1):62–68, February 1974.

[141] C. C. Dollins. In-pile densification of intergranular porosity in oxide fuels. Journal of Nuclear Materials, 82(2):302–310, July 1979.

[142] Y. Bouguerra and A. Si-Ahmed. A model for predicting evolution of pore size distributions in UO2 fuel. Journal of Nuclear Materials, 178(2):300–305, February 1991.

[143] Armando Carlos Marino, Eduardo J. Savino, and Santiago Harriague. BACO (BArra COmbustible) code version 2.20: a thermo-mechanical description of a nuclear fuel rod. Journal of Nuclear Materials, 229:155–168, April 1996.

[144] J. D. Hales, S. R. Novascone, G. Pastore, D. M. Perez, B. W. Spencer, and R. L. Williamson. Bison Theory Manual the Equations Behind Nuclear Fuel Analysis. Technical Report INL/EXT-13-29930, Idaho National Laboratory (INL), October 2013.

[145] CM Allison, GA Berna, R Chambers, EW Coryell, KL Davis, DL Hagrman, DT Hagrman, NL Hampton, JK Hohorst, RE Mason, et al. Scdap/relap5/mod3. 1 code manual volume iv: Matpro–a library of materials properties for light-water-reactor accident analysis. DT Hagrman, NUREG/CR-6150, EGG-2720, 4:4–234, 1993.

[146] A. D. Le Claire. The analysis of grain boundary diffusion measurements. British Journal of Applied Physics, 14(6):351, 1963.

[147] N. Moelans, B. Blanpain, and P. Wollants. Quantitative analysis of grain boundary properties in a generalized phase field model for grain growth in anisotropic systems. Physical Review B, 78(2):024113, July 2008.

[148] K. Ahmed, C. A. Yablinsky, A. Schulte, T. Allen, and A. El-Azab. Phase field modeling of the effect of porosity on grain growth kinetics in polycrystalline ceramics. Modelling and Simulation in Materials Science and Engineering, 21(6):065005, 2013.

[149] Cody J. Permann, Michael R. Tonks, Bradley Fromm, and Derek R. Gaston. Order parameter re-mapping algorithm for 3d phase field model of grain growth using FEM. Computational Materials Science, 115:18–25, April 2016.

[150] Mathis Plapp. Unified derivation of phase-field models for alloy solidification from a grand-potential functional. Physical Review E, 84(3):031601, September 2011.

[151] Larry K. Aagesen, Yipeng Gao, Daniel Schwen, and Karim Ahmed. Grand-potential-based phase-field model for multiple phases, grains, and chemical components. Physical Review E, 98(2):023309, August 2018.

[152] Seong Gyoon Kim, Won Tae Kim, and Toshio Suzuki. Phase-field model for binary alloys. Physical Review E, 60(6):7186–7197, December 1999.

[153] Abhik Choudhury and Britta Nestler. Grand-potential formulation for multicomponent phase transformations combined with thin-interface asymptotics of the double-obstacle potential. Physical Review E, 85(2):021602, February 2012.

[154] Michael R. Tonks, Derek Gaston, Paul C. Millett, David Andrs, and Paul Talbot. An object-oriented finite element framework for multiphysics phase field simulations. Computational Materials Science, 51(1):20–29, January 2012.

[155] Nele Moelans. A quantitative and thermodynamically consistent phase-field interpolation function for multi-phase systems. Acta Materialia, 59(3):1077–1086, February 2011.

[156] Hansjoachim Matzke. Atomic transport properties in UO2 and mixed oxides (U, Pu)O2. Journal of the Chemical Society, Faraday Transactions 2: Molecular and Chemical Physics, 83(7):1121–1142, 1987.

[157] R. O. A. Hall, M. J. Mortimer, and D. A. Mortimer. Surface energy measurements on UO2—A critical review. Journal of Nuclear Materials, 148(3):237–256, May 1987.

[158] P. V. Nerikar, D. C. Parfitt, L. A. Casillas Trujillo, D. A. Andersson, C. Unal, S. B. Sinnott, R. W. Grimes, B. P. Uberuaga, and C. R. Stanek. Segregation of xenon to dislocations and grain boundaries in uranium dioxide. Physical Review B, 84(17):174105, November 2011.

[159] M. Idiri, T. Le Bihan, S. Heathman, and J. Rebizant. Behavior of actinide dioxides under pressure: UO2 and ThO2. Physical Review B, 70(1):014113, July 2004.

[160] J. B. Ainscough, B. W. Oldfield, and J. O. Ware. Isothermal grain growth kinetics in sintered UO2 pellets. Journal of Nuclear Materials, 49(2):117–128, December 1973.

[161] D. A. Andersson, B. P. Uberuaga, P. V. Nerikar, C. Unal, and C. R. Stanek. U and Xe transport in UO2±x: Density functional theory calculations. Physical Review B, 84(5):054105, August 2011.

[162] A. C. S. Sabioni, W. B. Ferraz, and F. Millot. Effect of grain-boundaries on uranium and oxygen diffusion in polycrystalline UO2. Journal of Nuclear Materials, 278(2):364–369, April 2000.

[163] T. Arima, K. Yoshida, K. Idemitsu, Y. Inagaki, and I. Sato. Molecular dynamics analysis of diffusion of uranium and oxygen ions in uranium dioxide. IOP Conference Series: Materials Science and Engineering, 9(1):012003, 2010.

[164] E. Vincent-Aublant, J-M. Delaye, and L. Van Brutzel. Self-diffusion near symmetrical tilt grain boundaries in UO2 matrix: A molecular dynamics simulation study. Journal of Nuclear Materials, 392(1):114–120, July 2009.

[165] GB Alcock, RJ Hawkins, AWD Hills, and P McNamara. Paper sm-66/36, iaea, symp. Thermodynamics (Vienna, 1966), 1965.

[166] S. Yajima, H. Furuya, and T. Hirai. Lattice and grain-boundary diffusion of uranium in UO2. Journal of Nuclear Materials, 20(2):162–170, August 1966.

[167] M. O. Marlowe and A. I. Kaznoff. Tracer study of the surface diffusivity of UO2. Journal of Nuclear Materials, 25(3):328–333, March 1968.

[168] J. Henney and J. W. S. Jones. Surface-diffusion studies on UO2 and MgO. Journal of Materials Science, 3(2):158–164, March 1968.

[169] P. S. Maiya. Surface diffusion, surface free energy, and grain-boundary free energy of uranium dioxide. Journal of Nuclear Materials, 40(1):57–65, July 1971.

[170] L. Van Brutzel and E. Vincent-Aublant. Grain boundary influence on displacement cascades in UO2: A molecular dynamics study. Journal of Nuclear Materials, 377(3):522–527, July 2008.

[171] Michel Freyss, Thierry Petit, and Jean-Paul Crocombette. Point defects in uranium dioxide: Ab initio pseudopotential approach in the generalized gradient approximation. Journal of Nuclear Materials, 347(1):44–51, December 2005.

[172] R. O. A Hall, M. J Mortimer, and D. A Mortimer. A critical review of the surface energy of UO2. Journal of the Less Common Metals, 121:341–345, July 1986.

[173] P. Nikolopoulos, S. Nazare, and F. Thummler. Surface, grain boundary and interfacial energies in UO2 and UO2-Ni. Journal of Nuclear Materials, 71(1):89–94, December 1977.

[174] Klara Asp and John Agren. Phase-field simulation of sintering and related phenomena—A vacancy diffusion approach. Acta Materialia, 54(5):1241–1248, March 2006.

[175] Malvin H. Kalos and Paula A. Whitlock. Monte Carlo Methods. Wiley VHC, 2 edition, 2008.

[176] Kazunari Shinagawa, Shoko Maki, and Kozo Yokota. Phase-field simulation of platelike grain growth during sintering of alumina. Journal of the European Ceramic Society, 34(12):3027–3036, October 2014.

[177] Gert Ehrlich and F. G. Hudda. Atomic View of Surface SelfâĂŘDiffusion: Tungsten on Tungsten. The Journal of Chemical Physics, 44(3):1039–1049, February 1966.

[178] K. C. Radford and J. M. Pope. UO2 fuel pellet microstructure modification through impurity additions. Journal of Nuclear Materials, 116(2):305–313, June 1983.

[179] A. Leenaers, L. de Tollenaere, Ch. Delafoy, and S. Van den Berghe. On the solubility of chromium sesquioxide in uranium dioxide fuel. Journal of Nuclear Materials, 317(1):62–68, April 2003.

[180] Jakob Arborelius, Karin Backman, Lars Hallstadius, Magnus Limback, Jimmy Nillson, BjÃűrn Rebensdorff, Gang Zhou, Koji Kitano, Reidar Lofstrom, and Gunnar Ronnberg. Advanced Doped UO2 Pellets in LWR Applications. Journal of Nuclear Science and Technology, 43(9):967–976, September 2006.

[181] T. Cardinaels, K. Govers, B. Vos, S. Van den Berghe, M. Verwerft, L. de Tollenaere, G. Maier, and C. Delafoy. Chromia doped UO2 fuel: Investigation of the lattice parameter. Journal of Nuclear Materials, 424(1):252–260, May 2012.

[182] V. Peres, L. Favergeon, M. Andrieu, J. C. Palussiere, J. Balland, C. Delafoy, and M. Pijolat. High temperature chromium volatilization from Cr2O3 powder and Cr2O3-doped UO2 pellets in reducing atmospheres. Journal of Nuclear Materials, 423(1):93–101, April 2012.

[183] Jae Ho Yang, Keon Sik Kim, Ik Hui Nam, Jang Soo Oh, Dong-Joo Kim, Young Woo Rhee, and Jong Hun Kim. Effect of step wise variation of oxygen potential during the isothermal sintering on the grain growth behavior in Cr2O3 doped UO2 pellets. Journal of Nuclear Materials, 429(1):25–33, October 2012.

[184] Ch. Riglet-Martial, Ph. Martin, D. Testemale, C. Sabathier-Devals, G. Carlot, P. Matheron, X. Iltis, U. Pasquet, C. Valot, C. Delafoy, and R. Largenton. Thermodynamics of chromium in UO2 fuel: A solubility model. Journal of Nuclear Materials, 447(1):63–72, April 2014.

[185] M. J. F. Notley and I. J. Hastings. A microstructure-dependent model for fission product gas release and swelling in UO2 fuel. Nuclear Engineering and Design, 56(1):163–175, February 1980.

[186] Masaki Kurata. Research and development methodology for practical use of accident tolerant fuel in light water reactors. Nuclear Engineering and Technology, 48(1):26–32, 2016.

[187] Yifeng Che, Giovanni Pastore, Jason Hales, and Koroush Shirvan. Modeling of cr2o3-doped uo2 as a near-term accident tolerant fuel for lwrs using the bison code. Nuclear Engineering and Design, 337:271–278, 2018.

[188] I. Amato, R. L. Colombo, and A. Pentruccioli Balzari. Grain growth in pure and titania-doped uranium dioxide. Journal of Nuclear Materials, 18(3):252–260, March 1966.

[189] J. B. Ainscough, F. Rigby, and S. C. Osborn. The effect of titania on grain growth and densification of sintered UO2. Journal of Nuclear Materials, 52(2):191–203, October 1974.

[190] P. T. Sawbridge, C. Baker, R. M. Cornell, K. W. Jones, D. Reed, and J. B. Ainscough. The irradiation performance of magnesia-doped UO2 fuel. Journal of Nuclear Materials, 95(1):119–128, November 1980.

[191] M. W. D. Cooper, C. R. Stanek, and D. A. Andersson. The role of dopant charge state on defect chemistry and grain growth of doped UO2. Acta Materialia, 150:403–413, May 2018.

[192] Ki Won Kang, Jae Ho Yang, Jong Hun Kim, Young Woo Rhee, Dong Joo Kim, Keon Sik Kim, and Kun Woo Song. Effects of MnO-Al2o3 on the Grain Growth and High-Temperature Deformation Strain of UO2 Fuel Pellets. Journal of Nuclear Science and Technology, 47(3):304–307, March 2010.

[193] Jang Soo Oh, Dong-Joo Kim, Jae Ho Yang, Keon Sik Kim, Young Woo Rhee, and Yang-Hyun Koo. Recycling Process of U3O8 Powder in MnO-Al2O3 Doped Large Grain UO2 Pellets. Nuclear Engineering and Technology, 46(1):117–124, February 2014.

[194] Gerdjan Busker, Alex Chroneos, Robin W. Grimes, and I.-Wei Chen. Solution Mechanisms for Dopant Oxides in Yttria. Journal of the American Ceramic Society, 82(6):1553–1559, 1999.

[195] M. W. D. Cooper, M. J. D. Rushton, and R. W. Grimes. A many-body potential approach to modelling the thermomechanical properties of actinide oxides. Journal of Physics: Condensed Matter, 26(10):105401, February 2014.

[196] M. W. D. Cooper, S. T. Murphy, and D. A. Andersson. The defect chemistry of UO2±x from atomistic simulations. Journal of Nuclear Materials, 504:251–260, June 2018.

[197] M. N Rahaman. Ceramic processing and sintering. New York : M. Dekker, 1995.

[198] Boris Dorado, Philippe Garcia, Gaelle Carlot, Carine Davoisne, Mathieu Fraczkiewicz, Bertrand Pasquet, Michel Freyss, Carole Valot, Guido Baldinozzi, David Siméone, et al. First-principles calculation and experimental study of oxygen diffusion in uranium dioxide. Physical Review B, 83(3):035126, 2011.

[199] Arthur T. Motta and Donald R. Olander. Light Water Reactor Materials Volume 1: Fundamentals, volume 1. American Nuclear Society, 1 edition, 2017.

Vita

Ian Greenquist

Education

The Pennsylvania State University University Park, PA 2015–2019
Ph.D. Nuclear Engineering, August 2019
Area of Specialization: Computational Nuclear Materials

Brigham Young University Provo, UT 2012–2015
B.S. Chemical Engineering, May 2015
Area of Specialization: Controls and Optimization

Brigham Young University—Idaho Rexburg, ID 2010–2012
A.A.S. Engineering Technology, May 2012
Area of Specialization: Chemical Engineering

Experience

Nuclear Engineering Research Assistant The Pennsylvania State University 2015–2019
Sintering and Densification, Computational Models, Phase Field
Ph.D. Advisor: Prof. Michael Tonks

Nuclear Engineering Intern Idaho National Laboratory 2015
Phase Field, Spinodal Decomposition
Supervisor: Dr. Michael Tonks

Math Tutor Brigham Young University 2012–2015
Normal Differential Equations, Linear Algebra, Multivariable Calculus
Supervisor: Jackie Robertson

Chemical Engineering Intern Idaho National Laboratory 2014
Nuclear Hybrid Energy Systems, Biomass Fuel
Supervisor: Dr. Richard Boardman

Journal Publications for the Dissertation Research

I. Greenqiust, M. Tonks, Y. Zhang, *Analysis of the impact of fuel microstructure onirradiation-enhanced densification using grand potential simulations,* (in preparation).

I. Greenquist, M. Tonks, M. Cooper, D. Andersson, Y. Zhang, *Grand Potential Sintering Simulations of Doped UO2 Accident-Tolerant Fuel Concepts,* (ready to submit).

I. Greenquist, M. Tonks, L. Aagesen, Y. Zhang, *Development of a Microstructural Grand Potential-Based Sintering Model,* npj Computational Materials (under review).

I. Greenquist, M. Tonks, Y. Zhang, *Review of sintering and densification in nuclear fuels: Physical mechanisms, experimental results, and computational models,* Journal of Nuclear Materials, 2018.